The Application of Infrared Spectral Radiances and Fluxes for Arctic Climate Monitoring and Cloud Phase Determination from Space

by

Colten A. Peterson

A dissertation submitted in partial fulfillment
of the requirements for the degree of
Doctor of Philosophy
(Atmospheric, Oceanic, and Space Sciences)
in The University of Michigan
2022

Doctoral Committee:

Professor Xianglei Huang, Chair
Professor Valeriy Ivanov
Assistant Professor Cheng Li
Professor Christopher Ruf

Colten A. Peterson

coltenp@umich.edu

ORCID iD: 0000-0003-4904-9959

Dedication

To the friends that became family and my house jaguars, Cairo and Calypso.

Acknowledgements

Arriving at this point in my career could not have been possible without the support and guidance of many people. Throughout graduate school, my advisor Professor Xianglei Huang has provided me with unwavering support and guidance. He provided me with so much flexibility in developing my research projects, which allowed me to follow my passions and actively prepare for my future career. At the beginning of graduate school, I told Prof. Huang that I would like to pursue a career within the NASA Earth Science Division; he did everything in his power to help me actualize that goal. With his support and advocacy, I was able to present at NASA meetings and participate in summer NASA internships. These experiences opened many doors for me and were instrumental to my development as a researcher. Graduate school has been a very challenging experience, but Prof. Huang helped me develop the skills and strength to overcome those challenges. I could not have asked for a better advisor.

I would also like to acknowledge the numerous other individuals that have helped me on my graduate school journey. Firstly, I would like to thank the current and former members of my research group: Dr. Xiuhong Chen, Dr. Yi-Hsuan Chen, Chongxing Fan, and Yan Xie. I would also like to acknowledge the support and research mentorship from Dr. Qing Yue, who was my mentor at NASA JPL. I am also very grateful to Prof. Tristan L'Ecuyer for welcoming me to participate in the PREFIRE mission and supporting me in my career pursuits. There are many others that I cannot list, but I am truly grateful for everyone who has helped me along the way.

Table of Contents

List of Figures

Abstract

The Arctic climate is strongly influenced by infrared (IR) radiation emitted and absorbed by greenhouse gases, clouds, and the surface. As the Arctic continues to rapidly change, it is crucial to further understand how changes in such geophysical variables influence changes in IR flux at the Arctic surface and the top-of-atmosphere. Cloud phase (i.e., ice, liquid, and mixed) can affect the clouds' overall contributions to the IR fluxes. However, the spatial and temporal occurrences of Arctic cloud phase are not well characterized.

Satellite observations of spectrally resolved IR fluxes can be used to connect changes in the atmosphere and surface to broadband IR flux changes, however, such studies have not been performed in the Arctic. Spectral IR radiances can be used for satellite-based cloud phase retrievals, but conventional methods using the mid-IR window region (~800-1250 cm^{-1}) have limitations in polar regions, especially for mixed phase clouds. It may be possible to improve Arctic mid-IR cloud phase retrievals with far-IR (<~600 cm^{-1}) measurements. However, few studies have investigated far-IR cloud phase retrievals from space.

Overall, this dissertation studies the potential and limitations of spectral mid-IR and far-IR radiances and fluxes for monitoring Arctic IR radiation and identifying cloud phase from space. It contains four studies. The first study examines the trends of zonal mean spectral outgoing longwave radiation (OLR) and greenhouse efficiencies (GHE) in the Arctic from 2003 to 2016 using spectral flux derived from collocated Atmospheric IR Sounder (AIRS) and the Clouds and the Earth's Radiant Energy System observations in conjunction with AIRS retrievals. Positive and negative trends in Arctic OLR and GHE are observed across the far-IR and mid-IR spectral

regions, depending on the season, and the largest positive OLR and GHE trends occur in spring. Sensitivity studies reveal that surface temperature increases contribute most to the OLR and GHE trends, but the effects of atmospheric humidity and temperature are discernable.

In the second study, AIRS cloud phase retrievals, which were never evaluated over the Arctic, are evaluated against four years of combined CloudSat and the Cloud-Aerosol Lidar and Infrared Pathfinder Satellite Observation measurements over the Arctic Ocean. AIRS classification skill for single-layer ice- and liquid-phase clouds ranges from 85%–95% and 22%–32%, respectively. Most unknown and liquid AIRS phase classifications correspond to mixed-phase clouds.

The third study explores the synergy between the far- and mid-IR for polar ice cloud detection. A far-IR brightness temperature difference (BTD) test is developed and applied to simulated IR radiances and the results are compared to those from a mid-IR BTD test. Scattering leads to the far-IR being most sensitive to small ice particles, and the increase of cloud optical depth contributing to stronger far-IR BTD signals. Synergy between the mid-IR and far-IR is most useful for identifying cloud ice particles with an effective diameter around 40 µm.

The final study examines the sensitivity of simulated 11 µm brightness temperature (BT_{11}) to cloud ice changes within Arctic liquid-topped mixed phase clouds (LTMs). It was determined that BT_{11} can be sensitive to cloud ice for a range of commonly observed Arctic LTMs. By utilizing channels in the mid- and far-IR, it may be possible to use BTD tests together with a machine learning approach to detect Arctic LTMs from space.

Chapter 1 Introduction

1.1 The Changing Arctic

The Arctic is the northernmost area of the planet and lies north of the Arctic circle (66.56°N). Most of the Arctic region is covered by a nearly landlocked ocean surrounded by the northern parts of Russia, Canada, Greenland, Scandinavia, and the U.S. state of Alaska. The ocean itself consists of open water with areas of floating sea ice typically covered by a thick blanket of snow. The sea ice grows and melts seasonally, with a maximum extent typically in March and a minimum in September. The Arctic only receives significant amounts of sunlight for a few months during the northern hemisphere summer; in other parts of the year the Arctic is extremely cold and dark. Even during the sunlit summer months, the highly reflective sea ice reduces that amount of sunlight absorbed by the Arctic Ocean. This leads to the Arctic region absorbing much less solar radiation during the year compared to the tropics, where it is in excess. This establishes a negative temperature gradient from the tropics and Arctic, leading to poleward transport of heat from the tropics to Arctic (and the southern hemisphere polar region) via the atmosphere and ocean. The Arctic region, and the entire planet for that matter, emits electromagnetic radiation in the thermal infrared (IR; wavelengths greater than ~3 µm) part of the spectrum into outer space continuously and this acts as a cooling mechanism. Since the Arctic receives so little sunlight, the region emits more radiation to space annually than it receives. Overall, this leads to the Arctic venting the excess heat deposited by sunlight in the tropics into space. Thus, the Arctic (and its southern hemisphere counterpart) act as Earth's thermostats and changes in these regions can impact global climate.

Since the mid-20th century, Arctic surface-air temperatures (i.e., temperature at 2-m above the surface; SAT) have increased secularly, most noticeably during winter, at approximately twice the rate as the global average temperature (Figure 1.1a), a phenomenon known as Arctic Amplification (Serreze & Francis, 2006). Furthermore, during the era of satellite observations, there has been a steady decline in the September Arctic sea ice extent and thickness (e.g., Cavalieri & Parkinson, 2012; Lindsay and Schweiger, 2015). Figure 1.1b shows a 12.7 percent per decade reduction in September sea ice extent from 1979-2021 based on satellite passive microwave measurements. Many studies suggest that this Arctic sea ice decline may impact northern mid-latitude weather
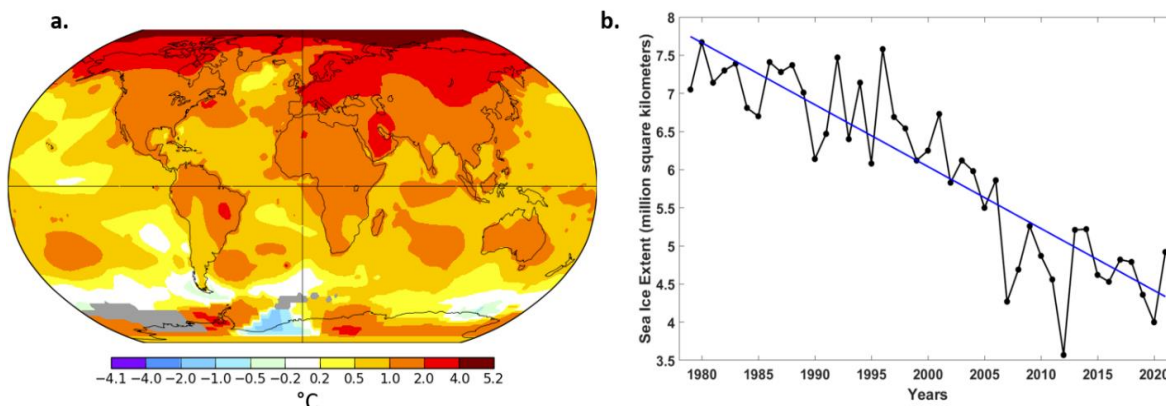
Figure 1.1. (a) Annually averaged temperature change over the period of 1960 to 2021. Data was obtained from NASA GISS (data.giss.nasa.gov). (b) Average Arctic September sea ice extent for the period 1978-2021 from the National Snow and Ice Data Center (nsicd.org). The blue line represents the linear least squares regression trend.

(Vihma, 2014). Furthermore, rising temperatures on the Greenland ice sheet have led to pronounced surface melt and runoff during this period as well. It is estimated that this melt has contributed to 10.6 mm of global sea level rise from 1992 to 2017 (Slater et al., 2020).

It is evident that the Arctic is transitioning into a regime characterized by higher surface temperatures and larger expanses of ice-free ocean than observed in previous decades. A leading theory is that the ice albedo feedback, i.e., a positive feedback in which ice melt fosters more solar radiation absorption into the Arctic ocean, which melts more ice and so on, is the main contributing

factor. It is also certain that numerous radiative and non-radiative processes and feedbacks play a role in the changes being observed in the Arctic. However, the relative contribution of such processes and feedbacks to the Arctic warming and sea ice decline is still a debated issue. Furthermore, the radiative and non-radiative contributions of clouds to current and future Arctic climate changes are not fully understood.

Climate model simulations tend to underestimate the trends in Arctic temperature increases and sea ice loss (e.g., Stroeve et al., 2012; Koenigk et al., 2013; Shu et al., 2020). Given that model simulations are the only mechanism in which to predict the response of the Arctic and the entire planet to anthropogenic greenhouse forcing, it is crucial to improve our understanding of the changing Arctic system.

1.2 Importance of Radiation in Arctic Climate

At the top-of-atmosphere (TOA; altitude of ~100 km above the Earth's surface) the sum of incoming and reflected solar, also referred to as shortwave (SW) radiative energy flux, and the outgoing IR radiative energy flux, also referred to as outgoing longwave radiation (OLR), determines the net TOA radiative flux (R_{TOA}) for the planet: it is zero when radiative equilibrium exists. For the Arctic, R_{TOA} is generally negative (i.e., more TOA upwelling radiation than downwelling radiation), except for a few months in the summer when the incoming SW TOA flux is largest (Serreze et al., 2007). At the surface, or at any given vertical level in the atmosphere, the sum of upwelling and downwelling SW and IR radiative fluxes determines the radiative heating (or cooling) rate, which plays a large role in determining temperatures at the surface and throughout the atmosphere. Figure 1.2 illustrates the various radiative processes discussed below.
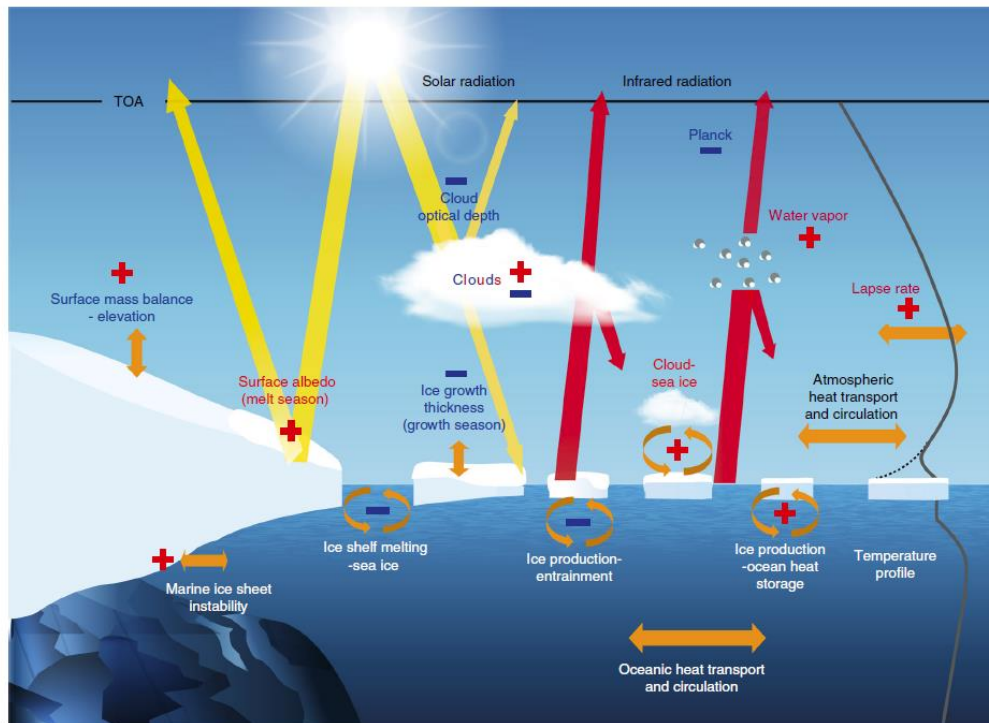
Figure 1.2. A schematic of some important radiative and non-radiative processes and feedbacks in the polar regions. Yellow and red indicate solar radiation and infrared radiative exchanges, respectively. The positive and negative signs represent the sign of the feedback. Gray lines represented simplified vertical temperature profiles. Adapted from Figure 1 in Goosse et al. (2018).

Incoming SW flux is most significant from April to September, with a peak in June. During these months, the SW radiation over the Arctic can be absorbed by the surface or reflected into space by sea ice, snow, clouds and other atmospheric gases and aerosols (Figure 1.2). While incoming SW radiation in the Arctic is only significant during the summer, IR radiative processes operate year-round. Both the atmosphere and surface emit IR radiation based on the Stephen Boltzmann law, where the emitted IR flux is proportional to the emitter's absolute temperature to the fourth power. The emissivity of either the atmosphere or surface at a given frequency, i.e., the difference between actual emission and blackbody emission (i.e., following Planck's Law) normalized by the blackbody emission at that frequency, can be generally equated to the

absorptivity, which is the fraction of incident radiation that is absorbed by the atmosphere or surface at that frequency.

While the Arctic surface can be generally considered as a blackbody (ignoring spectral variations in surface emissivity), the atmosphere's emissivity and absorptivity are mostly based on the spectroscopic features of atmospheric gases and the amounts of condensed cloud liquid or ice water. Water vapor is the main gaseous absorber and emitter of IR radiation in the Arctic atmosphere due to water molecule's many rotational and vibrational energy transitions that can be excited by IR photons of many different frequencies. Between about 800 and 1250 cm^{-1} (or 8 and 12.5 µm) the water vapor absorption is much smaller; this is referred to as a water vapor "window". This leads to most of the surface emission at these frequencies to be able to escape to space.

Clouds greatly enhance the emissivity of the Arctic atmosphere and can be completely opaque to IR radiation at cloud water paths (cloud water concentration that is vertically integrated) greater than ~100 g/m^2. The opacity of the cloud also depends on the size of liquid droplets or ice crystals within the cloud, where smaller cloud particles tend to lead to more opaque clouds for the same cloud water path. As will be discussed later, Arctic clouds and their opacity play a key role in warming the surface from their downwelling IR emissions.

For a given vertical atmospheric column, absorption and emission of IR radiation by the atmosphere leads to the origin of most of the photons that eventually escape to space to be at a colder temperature than the surface, which results in the OLR being less than the surface emission (Figure 1.2). This so-called greenhouse effect "traps" thermal energy in the system that would have otherwise escaped to space. The greenhouse effect can be quantified using the greenhouse efficiency (GHE) metric, which is the difference between the OLR and upwelling surface IR fluxes

normalized by those surface fluxes. For example, a GHE of one at a given frequency would mean that the OLR is zero at that frequency.

Numerous studies have shown that both SW and IR radiation are crucial components of the recent changes in Arctic temperature and sea ice extent. For the SW, a leading theory is that, as sea ice continues to retreat annually during the summer and autumn, an increased absorption of sunlight into the Arctic Ocean can delay the sea ice freeze-onset period, reduce ice thickness, and lead to more heat content in the ocean (e.g. Perovich et al., 2007). Since heat generally flows from the Arctic Ocean into the atmosphere during the winter months, the increased heat content in the ocean deposited in the sunlit seasons can lead to increased SATs in the winter (Screen & Simmonds 2010b; Serreze et al., 2009; Serreze & Barry 2011). This helps explain the fact that Arctic amplification is greatest during the winter months.

The IR is associated with radiative feedback processes that may contribute to Arctic amplification, namely the water vapor and lapse rate feedbacks (e.g. Goosse et al., 2018; Stueker et al., 2018; Figure 1.2). The water vapor feedback is based on the Clausius-Clapeyron relation, where the atmospheric humidity is exponentially related to the temperature of liquid water at the surface. Evaporation of water can lead to an increase in the water vapor GHE, which in turn can warm the surface and lead to more evaporation, and so on. The lapse rate is defined as the rate of change of temperature with height in the atmosphere. The lapse rate feedback in the Arctic is unique in that is positive, where at lower latitudes it is negative. Stable stratification of the Arctic atmosphere can result in a "bottom heavy" tropospheric warming profile as the Arctic surface warms, leading to a smaller increase in OLR compared to a uniform tropospheric warming, which can result in further surface warming (Goosse et al., 2018; Pithan & Mauritsen, 2014).

It has been shown through multiple studies that the Arctic atmosphere is becoming warmer and wetter (e.g., Boisvert et al., 2015a,b; Screen & Simmonds, 2010a; Serreze et al., 2012). The
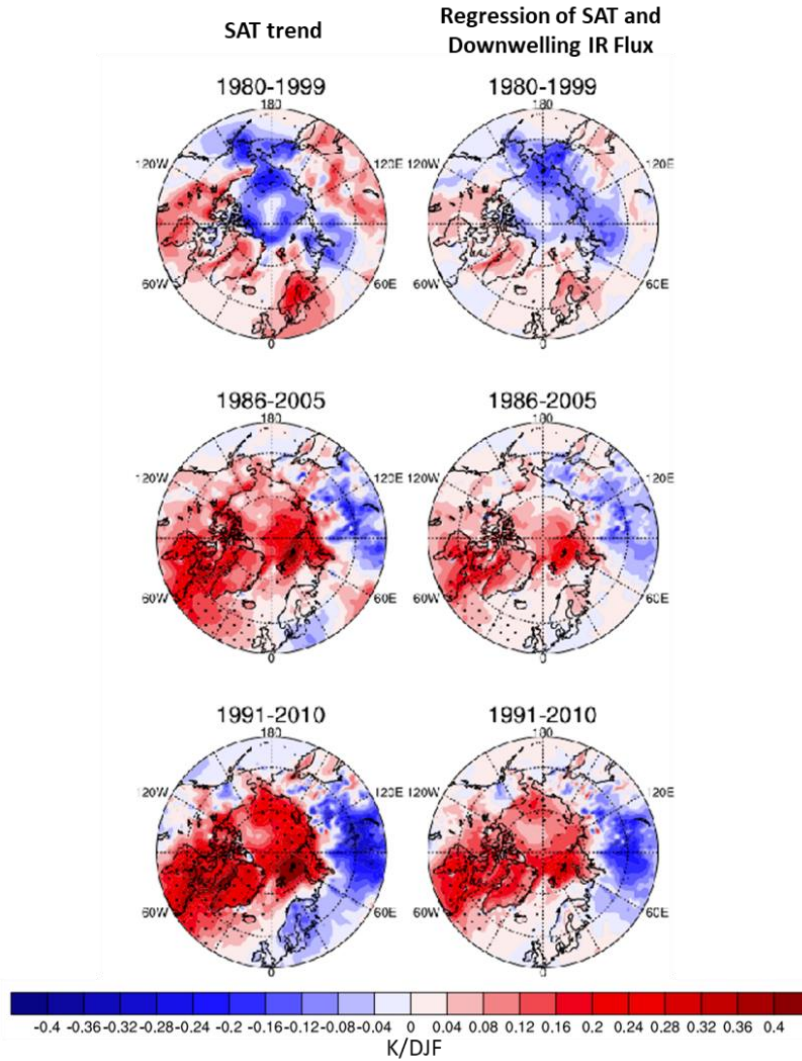
Figure 1.3. (left column) The interdecadal trend of surface-air-temperature (SAT) obtained by linear regression of winter (DJF) averaged SAT at each grid point (right column) trend derived from regression of SAT onto the downwelling IR flux $(d(SAT)/d(IR^{\downarrow})$; where the downwelling IR flux is $IR^{\downarrow}$) and multiplied by the interdecadal trend in the downwelling IR flux at each grid point. Units are in kelvin per winter season. The stippling indicates values that are significant at the $p < 0.05$ level for the Student's t test. Adapted from Figure 2 in Gong et al. (2017).

increased downwelling IR emissions from increasing humidity and temperature can increase the

greenhouse effect, and this can lead to early sea ice melt onset and increased surface warming in

the winter and spring, when Arctic amplification is most prominent (Kapsch et al., 2013; Cao et

al., 2017). Both Gong et al. (2017) and Lee et al. (2017) determined that, in recent decades, the

spatial pattern of winter SAT trends is strongly related to the spatial pattern of downwelling IR flux trends. Figure 1.3 shows, for three different 20-year periods, that the linear regression of the SAT onto downwelling IR fluxes results in a very similar spatial pattern compared to the SAT trends. This highlights the importance of IR radiative processes in understanding current and future Arctic climate changes

1.3 Cloud-Radiation Interactions and the Role of Cloud Phase in the Arctic

The Arctic has extensive cloud coverage throughout the year that can be greater than 80% and 50% in the summer and winter, respectively (Kay et al., 2016). As discussed previously, clouds can change both the amount of SW and IR radiative flux that is incident on the surface compared to clear sky conditions. This is known as cloud radiative forcing. This cloud radiative forcing can be quantified as the difference between all-sky and clear-sky radiative fluxes (IR or SW) and can be assessed for the TOA or surface.

A major summertime radiative role of clouds in the Arctic is the reflection of sunlight and modulation of the amount of solar energy absorbed by the ocean (Kay & L'Ecuyer, 2013) and hence a negative cloud radiative forcing at the surface. However, the emission and absorption of IR radiation by clouds is active year-round, and for most of the year this causes an overall surface warming effect of clouds due to the downwelling IR emission (Interieri et al., 2002), which would be a positive cloud radiative forcing at the surface. The cloud's thermodynamic phase, or whether it is composed of liquid droplets, ice crystals, or both, can determine the IR surface warming effect of clouds in the Arctic. This is because, for the same amount of cloud water, liquid-containing clouds tend to be opaquer in the IR compared to ice-only clouds, which leads to liquid clouds dominating the surface warming effects in the Arctic (Shupe and Intrieri, 2004; Cesana et al., 2012). Furthermore, liquid droplets tend to be smaller than ice particles, which leads to liquid

clouds being more reflective at visible wavelengths, and thus cloud phase can also influence the summer-time radiative effects of clouds (Shupe & Intrieri, 2004). Supercooled liquid cloud droplets can exist at temperatures as low as -40°C (Shupe, 2011) and thus mixed phase clouds are
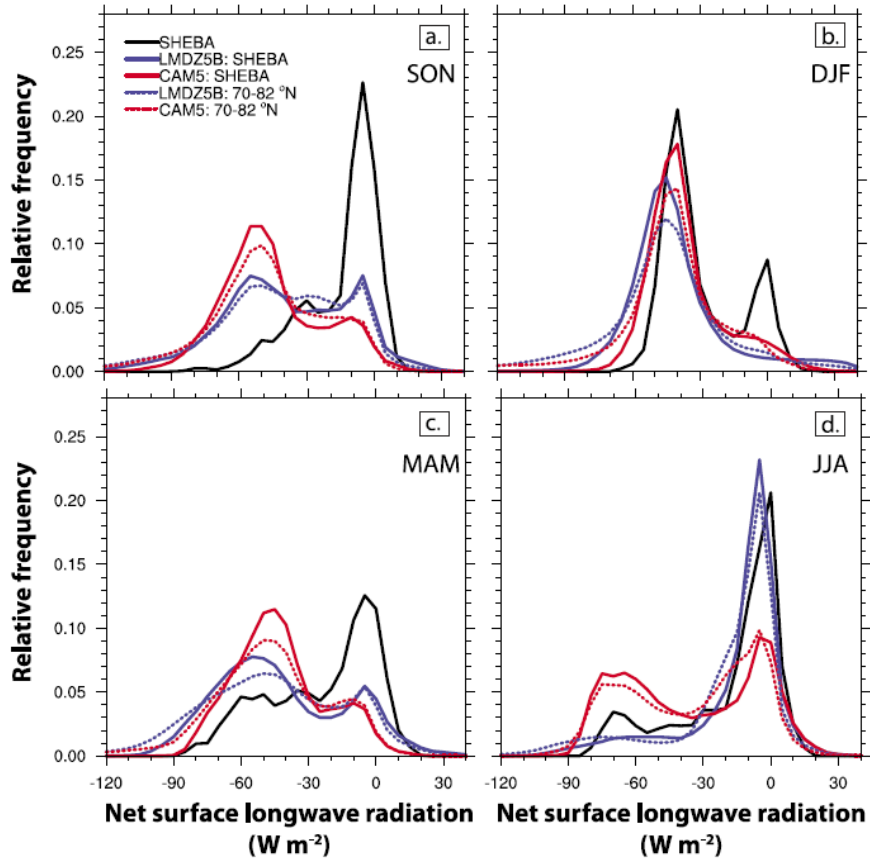
Figure 1.4. Probability density functions of hourly Arctic Ocean net (down minus up) surface longwave radiation by season in two climate models (LMDZ5B) [Hourdin et al., 2012], CAM5 [Neale et al., 2010], and SHEBA observations [Persson et al., 2002]: (a) Fall (SON), (b) Winter (DJF), (c) Spring (MAM), and (d) Summer (JJA). Climate model SHEBA points based on averages over 70–80 N and 190–240 E, while SHEBA observations are taken along a single ship track. LMDZ5B model data are 3-hour averages, while SHEBA observations and CAM5 model data are 1-hour averages. Adapted from Cesana et al. (2012).

common in the Arctic. These clouds are produced and maintained by numerous complex microphysical processes and radiative and non-radiative feedbacks that interconvert liquid and ice particles (Morrison et al., 2012). The typical structure of Arctic mixed phase clouds is a thin liquid layer above a precipitating ice cloud layer (de Boer et al., 2011). As will be discussed later, mixed phase clouds present a challenge for cloud remote sensing. A lack of understanding of processes

involving the interconversion of cloud liquid and ice in the Arctic atmosphere leads to misrepresentation of clouds in climate models and their associated IR radiative effects (e.g., Cesana et al., 2012; Pithan et al., 2014). For example, Figure 1.4 shows the probability distribution of net LW (or IR) radiation (positive downward) at the Arctic surface from in-situ observations (black solid line) for each season. Liquid-containing clouds tend to be associated with a net LW flux of about 0 W/m^2, while ice clouds tend to correspond to more negative values (Morrison et al., 2012). These are commonly referred to radiatively opaque and clear states, respectively (e.g., Morrison et al., 2012; Stramler et al., 2011). Figure 1.4 also shows climate model simulations that aimed to reproduce these radiative states (colored solid and dotted lines). During all seasons except for summer (JJA), the models do not capture the probability distribution of net LW flux, which is related to the model's representation of supercooled cloud liquid in the Arctic (e.g., Cesana et al., 2012). Overall, it is crucial to further the understanding of Arctic cloud processes, especially relating to cloud phase, to improve projections of warming and sea ice loss in the Arctic.

1.4 Satellite Remote Sensing of Arctic Clouds: Methods and Challenges

To further understand Arctic cloud properties, their radiative effects at the top-of-atmosphere (TOA) and surface, and how these change over time, observations are needed across the vast Arctic region. Ground observations are important but are sparse in the Arctic due to the remoteness and harshness of the environment: satellite observations are essential.

Modern spaceborne measurements of cloud properties, such as cloud phase, generally rely on at least one of the following: (1) lidar (i.e., laser) backscatter and depolarization (2) radar backscatter (3) spectrally resolved SW radiances that are reflected from the clouds and (4) spectrally resolved IR radiances that are either emitted by the cloud or are attenuated by the cloud.

Active satellite instruments such as Cloud–Aerosol Lidar and Infrared Pathfinder Satellite Observations (CALIPSO) and CloudSat use lidar and radar, respectively, and can be combined for cloud property measurements (e.g., Sassen et al., 2008). The major benefit of active measurements is that they can provide vertical profiles of cloud properties and more confident cloud phase determination compared to IR and SW imagers. However, these measurements are taken along a narrow ground track (e.g., ~0.1 km track width for CALIPSO), which means that many Arctic cloud scenes are not observed during a given overpass. There are also complicating factors, such as multiple scattering of lidar by cloud liquid droplets which can lead to an inaccurate cloud phase determination (Hu et al., 2009). Overall, active sensor cloud products are benchmarks for comparison with passive imager cloud products, especially cloud phase.

Spectrally resolved measurements of reflected solar radiance, such as those from the Moderate Resolution Imaging Spectroradiometer (MODIS), can provide information on cloud properties based on the differences in cloud liquid and ice absorption and scattering at different SW wavelengths. For example, the ratio of reflectance at 2.1 and 0.87 µm is used by the MODIS Collection 6 Cloud Optical Properties Algorithm (Platnick et al., 2014), as this ratio can provide information on cloud phase, cloud opacity, and cloud particle size. A major benefit of SW imagers is that the horizontal spatial footprint can be larger than the active sensors (e.g., 1 km MODIS pixels). Imagers like MODIS also utilize cross track scanning, which ultimately provides large swaths of pixels for a given satellite overpass. However, there are major drawbacks in the Arctic for SW cloud remote sensing. Firstly, during the sunlit months in the Arctic, the presence of underlying sea ice and snow can complicate cloud detection and property retrievals (Platnick et al., 2001). Secondly, there is a lack of sunlight that is usable by spaceborne SW imagers in the Arctic throughout much of the year. Even during the summer, the solar zenith angle (angle between

the sun and the zenith) only becomes as low as ~66°. Such large zenith angles can also complicate

SW retrievals of cloud properties (Grosvenor & Wood, 2014).

Spaceborne measurements of spectral IR radiances are particularly useful in the Arctic

because they can be used all year-round. Additionally, imagers such as the Atmospheric Infrared

Sounder (AIRS) aboard the NASA Aqua spacecraft have larger horizontal spatial footprints than

the active sensors (e.g., ~13.5 km radius footprint for AIRS). Spectral IR radiances can be used

for cloud detection and cloud retrievals, such as cloud phase. Detection of clouds from spaceborne
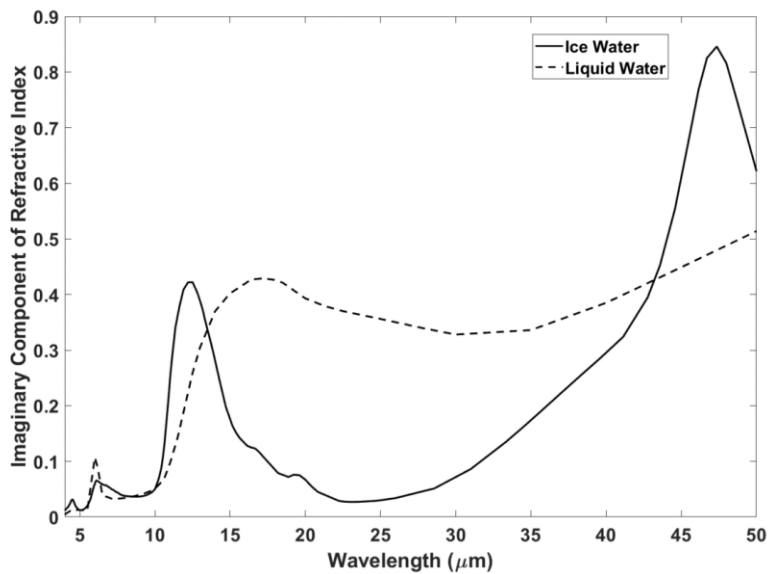
Figure 1.5. Imaginary component of refractive index for liquid and ice water from 4 to 50 µm.

IR measurements is based on the difference in the radiative temperatures between clouds and the

surface. However, this cloud detection can be difficult in the Arctic because it is not uncommon,

especially during the winter and spring, for the clouds to exist within a temperature inversion and

be at the same temperature or warmer than the surface. This can lead to the cloud being

indistinguishable from nearby clear sky scenes. Cloud phase within an IR imager footprint can be

determined using spectral IR radiances, and it is a convention to utilize brightness temperature

differences (BTDs) between two spectral channels within the mid-infrared window (mid-IR; 8-

12

12.5 µm; 800-1250 cm^{-1}). This is possible because the spectral variations of liquid and ice water absorption across the mid-IR are sufficiently different (Figure 1.5). One of the main challenges for Arctic cloud phase determination using the mid-IR, besides the cloud detection limitations, is the ubiquitous presence of mixed phase clouds in the Arctic (Baum et al., 2000; Cho et al., 2009). This can lead to ambiguous cloud phase determination using the mid-IR. Furthermore, due to the larger IR imager footprints compared to active sensors, it is possible that clear sky, liquid clouds, ice clouds, and mixed phase clouds can exist within the same footprint.

1.5 The Far-IR Observation Gap

The far-infrared (far-IR; >15 µm) makes up over 60% of Arctic OLR and thus is an important part of the radiative energy processes in the Arctic. There are many water vapor absorption lines across the far-IR spectral region, and thus both downwelling IR fluxes and OLR are sensitive to water vapor's far-IR spectroscopic properties (Turner & Mlawyer, 2010).

There has been a lack of spectrally resolved far-IR radiance measurements from space during the modern satellite era, which is largely due to technology limitations. However, two upcoming missions will measure the far-IR spectral radiances: the Far-infrared-Outgoing-Radiation Understanding and Monitoring (FORUM; Palchetti et al., 2020) and the Polar Radiant Energy in the Far Infrared Experiment (PREFIRE; L'Ecuyer et al., 2021) missions.

The spectral region from 400 to 600 cm^{-1}, which is referred to as the "dirty" window region (Yang et al., 2003), contains numerous semi-transparent water vapor micro-windows. The cold and dry Arctic atmosphere means that some far-IR dirty window channels can be sensitive to lower tropospheric water vapor and clouds. Furthermore, the far-IR can be sensitive to cloud properties such as cloud phase (Turner et al., 2003; Maestri et al., 2019b; Di Natale et al., 2020) and ice cloud particle size (Yang et al., 2003; Libois & Blanchet, 2017; Saito et al., 2020). All the above facts

suggest that the spaceborne far-IR radiance measurements can be a useful tool for the remote sensing of Arctic atmospheric and cloud properties in the Arctic.

1.6 Connections and Relevance of Main Chapters

The following chapters present work that aims to address challenges and knowledge gaps relevant to the discussion above. Spectral fluxes are underutilized and represent a tool for connecting changes in atmospheric and surface properties to changes in broadband radiative fluxes at the top-of-atmosphere. Given that the Arctic is rapidly changing, and IR radiative processes are crucial to Arctic climate, such spectral fluxes can provide deeper insight into changes in Arctic climate compared to broadband fluxes. The phase of clouds represents an important contributor to the IR radiative processes in the Arctic, but the spatial and temporal distribution of cloud phase in the Arctic is not well characterized. Since IR imagers are useful for cloud phase determination from space, it is important to further understand the limitations of conventional mid-IR cloud phase algorithms over the Arctic and the potential for far-IR spectral radiance measurements, which will be made for the first time this decade, to improve mid-IR Arctic cloud phase determination. Lastly, mixed phase clouds are ubiquitous and not well characterized in the Arctic, and detecting such clouds from space is an ongoing challenge for mid-IR imagers. Thus, it is important to investigate the potential for mixed phase cloud detection in the Arctic by examining mid-IR limitations and the benefits of combined mid-IR and far-IR observations for such detections.

Chapter 2 investigates 14-year trends in spectrally resolved OLR and GHE over the Arctic region. Typically, such studies utilize broadband radiative fluxes: the integration of spectral fluxes across the IR spectrum. While the broadband fluxes are useful, the spectral fluxes can be used to further assess how changes in the Arctic atmosphere and surface contribute to the broadband fluxes. This is because different spectral channels can be sensitive to changes in atmospheric

temperature and composition at different vertical levels. Furthermore, spectrally resolved IR fluxes are important for observation-model comparisons. If only broadband fluxes are used in such comparisons, there can be compensating biases in the spectral fluxes that cause the broadband fluxes to agree for the wrong reasons (e.g., Huang et al., 2006; Huang et al., 2014). Overall, spectral fluxes are underutilized, especially in the analysis of Arctic IR processes, which suggests that there is a lack of knowledge on how changes in the Arctic atmosphere and surface contribute to the broadband OLR and GHE. Chapter 2 addresses this lack of knowledge by comparing observed spectral OLR and GHE trends to those simulated with a radiative transfer model that uses satellite retrieved geophysical variables as inputs. Furthermore, the observed spectral OLR and GHE trends are extended using principal component analysis to include trends in the far-IR. Such spectral far-IR OLR and GHE trends in the Arctic have not been explored and they can ultimately shed light onto how changes in tropospheric water vapor and temperature at different atmospheric levels in the Arctic can impact OLR and GHE in the far-IR.

Chapter 2 mainly focuses on clear sky scenes due to the difficulty in simulating OLR and GHE in cloudy scenes. As discussed previously, there are complexities and challenges with satellite retrievals of cloud properties in the Arctic, especially for cloud phase determinations. Improving Arctic cloud phase retrievals can (1) improve knowledge of the cloud meteorological and hydrological processes and how they change with Arctic climate and (2) the radiative impacts of the clouds at the Arctic TOA and surface. It was previously discussed that cloud remote sensing using spectral radiances in the mid-IR window region has advantages in the Arctic, namely that it can be used throughout the year. The AIRS instrument aboard the NASA Aqua spacecraft, capable of measuring mid-IR radiances at high spectral resolution, has collected such radiances over the Arctic for two decades. This suggests that AIRS could be a useful tool for cloud phase studies of

the Arctic. However, the AIRS cloud phase product was never evaluated and compared with active sensors over the Arctic, which is a necessary step to validate the AIRS product in the region.

Chapter 3 addresses this challenge by collocating four years of joint CALIPSO-CloudSat cloud observations over the Arctic with coincident AIRS footprints to compare cloud phase classifications from both products. Additionally, the study compares the climatology of Arctic cloud phase between AIRS and the active sensors to understand if AIRS can capture the cloud phase seasonality, zonal distribution, and connections with meteorological and thermodynamic variables.

The results of Chapter 3 can further illuminate the advantages and disadvantages of the mid-IR spectral radiances for Arctic cloud phase determination. As was discussed previously, the far-IR may be useful for retrievals of cloud properties in the Arctic due to the cold and dry atmosphere and the sensitivity of the far-IR to cloud properties. Like the mid-IR, the spectral variations of liquid and ice absorption have differences across the far-IR dirty window region. This suggests that a far-IR BTD method could be applicable for satellite-based Arctic cloud phase determination. Furthermore, the spectral variations of ice and liquid scattering properties are larger than in the mid-IR, which suggests that far-IR scattering can be taken advantage of in a far-IR BTD framework. Recent studies have, using a machine learning approach, indicated that the far-IR and mid-IR can be used jointly for cloud phase determination (e.g., Maestri et al., 2019b). Chapter 4 aims to develop a simple and physically based far-IR BTD polar ice cloud detection test that can supplement or even improve the conventional mid-IR BTD approach.

The detection of mixed phase clouds in the Arctic continues to be a challenge for spaceborne IR imagers. This dissertation and previous studies show that the mid-IR and far-IR are most useful for ice cloud detection. While detection both cloud phases simultaneously with the IR

is a subject of future work, Chapter 5 of this dissertation examines the potential for the use of IR spectral radiances to detect the presence of ice in one of the most common mixed phase clouds in the Arctic. This chapter also discusses the potential of combining mid- and far-IR spectral radiances for mixed phase cloud detection in the Arctic.

References

Baum, B. A., Soulen, P. F., Strabala, K. I., King M. D., Ackerman, S. A., et al. (2000). Remote sensing of cloud properties using MODIS Airborne Simulator imagery during SUCCESS. 2. Cloud thermodynamic phase. *Journal of Geophysical Research*, 105, 11 781–11 792. https://doi.org/10.1029/ 1999JD901090

Boisvert, L. N., & Stroeve, J. C. (2015). The Arctic is becoming warmer and wetter as revealed by the Atmospheric Infrared Sounder. *Geophysical Research Letters*, 42(11), 4439-4446. https://doi.org/10.1002/2015gl063775

Boisvert, L. N., Wu, D. L., & Shie, C. L. (2015). Increasing evaporation amounts seen in the Arctic between 2003 and 2013 from AIRS data. *Journal of Geophysical Research: Atmospheres*, 120(14), 6865-6881, https://doi.org/10.1002/2015jd023258

Cao, Y. F., Liang, S. L., Chen, X. N., He, T., Wang, D. D., & Cheng, X. (2017). Enhanced wintertime greenhouse effect reinforcing Arctic amplification and initial sea-ice melting. *Scientific Reports*, 7, 9. https://doi.org/10.1038/s41598-017-08545-2

Cavalieri, D. J., & Parkinson, C. L. (2012). Arctic sea ice variability and trends, 1979-2010. *Cryosphere*, 6(4), 881-889. https://doi.org/10.5194/tc-6-881-2012

Cesana, G., Kay, J. E., Chepfer, H., English, J. M., & de Boer, G. (2012). Ubiquitous low-level liquid-containing Arctic clouds: New observations and climate model constraints from CALIPSOGOCCP. *Geophysical Research Letters*, 39, L20804. https://doi.org/10.1029/ 2012GL053385

Cho, H. M., Nasiri, S. L., & Yang, P. (2009). Application of CALIOP measurements to the evaluation of cloud phase derived from MODIS infrared channels. *Journal of Applied Meteorology and Climatology*, 48, 2169– 2180. https://doi.org/10.1175/2009JAMC2238.1

de Boer, G., Morrison, H., Shupe, M. D., & Hildner, R. (2011). Evidence of liquid dependent ice nucleation in high-latitude stratiform clouds from surface remote sensors. *Geophysical Research Letters,* 38, L01803. doi:10.1029/2010GL046016

Di Natale, G., Bianchini, G., Del Guasta, M., Ridolfi, M., Maestri, T., et al. (2020). Characterization of the Far Infrared Properties and Radiative Forcing of Antarctic Ice and Water

Clouds Exploiting the Spectrometer-LiDAR Synergy. *Remote Sensing*, 12, 3574. https://doi.org/10.3390/rs12213574

Gong, T. T., Feldstein, S., & Lee, S. (2017). The role of downward infrared radiation in the recent Arctic winter warming trend. *Journal of Climate*, 30(13), 4937-4949. https://doi.org/10.1175/jcli-d-16-0180.1

Goosse, H., Kay, J.E., Armour, K.C., Bodas-Salcedo, A., Chepfer, H., *et al.* (2018). Quantifying climate feedbacks in polar regions. *Nature Communications,* 9, 1919. https://doi.org/10.1038/s41467-018-04173-0

Grosvenor, D. P. & Wood, R. (2014). The effect of solar zenith angle on MODIS cloud optical and microphysical retrievals within marine liquid water clouds. *Atmospheric Chemistry and Physics*, 14, 7291–7321. https://doi.org/10.5194/acp-14-7291-2014

Hu, Y., Winker, D., Vaughan, M., Lin, B., Omar, A., Trepte, C., et al. (2009). CALIPSO/CALIOP Cloud Phase Discrimination Algorithm. *Journal of Atmospheric and Oceanic Technology*, 26(11), 2293-2309. https://doi.org/10.1175/2009JTECHA1280.1

Huang, X. L., Chen, X. H., Soden, B. J., & Liu, X. (2014). The spectral dimension of longwave feedback in the CMIP3 and CMIP5 experiments. *Geophysical Research Letters*, 41, 7830–7837. https://doi.org/10.1002/2014gl061938

Huang, X. L., Ramaswamy, V., & Schwarzkopf, M. D. (2006). Quantification of the source of errors in AM2 simulated tropical clear-sky outgoing longwave radiation. *Journal of Geophysical Research*, 111, D14107. https://doi.org/10.1029/2005jd006576

Intrieri, J. M., Fairall, C. W., Shupe, M. D., Persson, P. O. G., Andreas, E. L., et al. (2002). An annual cycle of Arctic surface cloud forcing at SHEBA. *Journal of Geophysical Research*, 107, 8039. https://doi.org/10.1029/2000JC000439

Kapsch, M. L., Graversen, R. G., & Tjernstrom, M. (2013). Springtime atmospheric energy transport and the control of Arctic summer sea-ice extent. *Nature Climate Change*, 3(8), 744-748. https://doi.org/10.1038/nclimate1884

Kay, J. E., & L'Ecuyer T. (2013). Observational constraints on Arctic Ocean clouds and radiative fluxes during the early 21st century. *Journal of Geophysical Research: Atmospheres*, 118, 7219–7236. https:// doi.org/10.1002/JGRD.50489

Kay, J. E., Bourdages, L., Miller, N. B., Morrison, A., Yettella, V., et al. (2016). Evaluating and improving cloud phase in the Community Atmosphere Model version 5 using spaceborne lidar observations. *Journal of Geophysical Research: Atmospheres*, 121, 4162–4176.doi:10.1002/2015JD024699.

Koenigk, T., Brodeau, L., Graversen, R.G., Karlsson, J., Svensson, G., Tjernstrom, M., et al. (2013). Arctic climate change in 21st century CMIP5 simulations with EC-Earth. *Climate Dynamics*, 40, 2719–2743. https://doi.org/10.1007/s00382-012-1505-y

L'Ecuyer, T. S., Drouin, B. J., Anheuser, J., Grames, M., Henderson, et al. (2021). The Polar Radiant Energy in the Far InfraRed Experiment: A New Perspective on Polar Longwave Energy Exchanges. *Bulletin of the American Meteorological Society*, 1-46. https://doi.org/10.1175/BAMS-D-20-0155.1

Lee, S., Gong, T. T., Feldstein, S. B., Screen, J. A., & Simmonds, I. (2017). Revisiting the cause of the 1989-2009 Arctic surface warming using the surface energy budget: Downward infrared radiation dominates the surface fluxes. *Geophysical Research Letters*, 44(20), 10654-10661. https://doi.org/10.1002/2017gl075375

Libois, Q., & Blanchet, J. P. (2017). Added value of far-infrared radiometry for remote sensing of ice clouds. *Journal of Geophysical Research: Atmospheres*, 122(12), 6541-6564. https://doi:10.1002/2016jd026423

Lindsay, R., & Schweiger, A. (2015). Arctic sea ice thickness loss determined using subsurface, aircraft, and satellite observations, *The Cryosphere*, 9, 269–283, https://doi.org/10.5194/tc-9-269-2015

Maestri, T., Cossich, W., & Sbrolli, I. (2019). Cloud identification and classification from high spectral resolution data in the far infrared and 840 mid-infrared. *Atmospheric Measurement Techniques*, 12, 3521–3540, https://doi.org/10.5194/amt-12-3521-2019

Morrison, H., de Boer, G., Feingold, G., Harrington, J., Shupe, M. D., *et al.* (2012). Resilience of persistent Arctic mixed-phase clouds. *Nature Geoscience,* 5, 11–17 (2012). https://doi.org/10.1038/ngeo1332

Palchetti, L., Brindley, H., Bantges, R., Buehler, S. A., Camy-Peyret, C., et al. (2020). FORUM: Unique Far-Infrared Satellite Observations to Better Understand How Earth Radiates Energy to Space. *Bulletin of the American Meteorological Society*, 101(12), E2030-E2046. https://doi.org/10.1175/BAMS-D-19-0322.1

Perovich D., Light, B., Eicken, H., Jones, K.F., Runciman, K., et al., (2007). Increasing solar heating of the Arctic Ocean and adjacent seas, 1979–2005: Attribution and role in the ice-albedo feedback. *Geophysical Research Letters*, 34:L19505. 10.1029/2007GL031480.

Pithan, F. & Mauritsen, T. (2014). Arctic amplification dominated by temperature feedbacks in contemporary climate models. *Nature Geoscience*, 7, 181–184. https://doi.org/10.1038/ngeo2071

Pithan, F., Medeiros, B. & Mauritsen, T. (2014). Mixed-phase clouds cause climate model biases in Arctic wintertime temperature inversions. *Climate Dynamics,* 43, 289–303. https://doi.org/10.1007/s00382-013-1964-9

Platnick, S., King, M. D., Meyer, K. G., Wind, G., Amarasinghe, N., et al. (2014). MODIS Cloud Optical Properties: User Guide for the Collection 6 Level-2 MOD06/MYD06 Product and Associated Level-3 Datasets. http://modis-atmos.gsfc.nasa.gov/ _docs/C6MOD06OPUserGuide.pdf

Platnick, S., Li, J. Y., King, M. D., Gerber, H., and Hobbs, P. V. (2001). A solar reflectance method for retrieving the optical thickness and droplet size of liquid water clouds over snow and ice surfaces. *Journal of Geophysical Research*, 106(D14), 15185– 15199. doi:10.1029/2000JD900441

Saito, M., Yang, P., Huang, X., Brindley, H. E., Mlynczak, M. G., et al. (2020). Spaceborne middle- and far-infrared observations improving nighttime ice cloud property retrievals. *Geophysical Research Letters*, 47, e2020GL087491. https://doi.org/10.1029/2020GL087491

Sassen, K., Wang, Z., & Liu, D. (2008). Global distribution of cirrus clouds from CloudSat/Cloud-Aerosol Lidar and Infrared Pathfinder Satellite Observations (CALIPSO) measurements. *Journal of Geophysical Research*, 113, D00A12. https://doi.org/10.1029/2008JD009972

Screen, J. A., & Simmonds, I. (2010a). The central role of diminishing sea ice in recent Arctic temperature amplification. *Nature*, 464(7293), 1334-1337. https://doi.org/10.1038/nature09051

Screen, J. A., & Simmonds, I. (2010b). Increasing fall-winter energy loss from the Arctic Ocean and its role in Arctic temperature amplification. *Geophysical Research Letters*, 37, 5. https://doi.org/10.1029/2010gl044136

Serreze, M. C., & Barry, R. G. (2011). Processes and impacts of Arctic amplification: A research synthesis. *Global and Planetary Change*, 77(1-2), 85-96. https://doi.org/10.1016/j.gloplacha.2011.03.004

Serreze, M. C., & Francis, J. A. (2006). The Arctic amplification debate. *Climatic Change*, 76(3-4), 241-264. https://doi.org/10.1007/s10584-005-9017-y

Serreze, M. C., Barrett, A. P., & Stroeve, J. (2012). Recent changes in tropospheric water vapor over the Arctic as assessed from radiosondes and atmospheric reanalyses. *Journal of Geophysical Research: Atmospheres*, 117, 21. https://doi.org/10.1029/2011jd017421

Serreze, M. C., Barrett, A. P., Slater, A. G., Steele, M., Zhang, J., et al. (2007). The large-scale energy budget of the Arctic. *Journal of Geophysical Research*: *Atmospheres*, 112(D11). https://doi.org/10.1029/2006JD008230

Serreze, M. C., Barrett, A. P., Stroeve, J. C., Kindig, D. N., & Holland, M. M. (2009). The emergence of surface-based Arctic amplification. *Cryosphere*, 3(1), 11-19. https://doi.org/10.5194/tc-3-11-2009

Serreze, M.C. (2015.). Arctic climate. *Encyclopedia of Atmospheric Sciences, 2nd edition (J North, ed.)*, Academic Press, 107-115,. http://dx.doi.org/10.1016/B978-0-12-382225-3.00072-4

Shu, Q., Wang, Q., Song, Z., Qiao, F., Zhao, J., et al. (2020). Assessment of sea ice extent in CMIP6 with comparison to observations and CMIP5. *Geophysical Research Letters*, 47, e2020GL087965. https://doi.org/10.1029/2020GL087965

Shupe, M. D. (2011). Clouds at Arctic atmospheric observatories. Part II: Thermodynamic phase characteristics. *Journal of Applied Meteorology and Climatology*, 50, 645–661. https://doi.org/10.1175/2010JAMC2468.1

Shupe, M. D., & Intrieri, J. M. (2004). Cloud radiative forcing of the Arctic surface: The influence of cloud properties, surface albedo, and solar zenith angle. *Journal of Climate*, 17, 616–628. https://doi.org/ 10.1175/1520-0442(2004)017,0616:CRFOTA.2.0.CO;2

Stramler, K., Del Genio, A. D., & Rossow, W. B. (2011). Synoptically Driven Arctic Winter States. *Journal of Climate*, *24*(6), 1747-1762. https://doi.org/10.1175/2010JCLI3817.1

Stroeve, J. C., Kattsov, V., Barrett, A., Serreze, M., Pavlova, et al. (2012). Trends in Arctic sea ice extent from CMIP5, CMIP3 and observations. *Geophysical. Research. Letters.*, 39, L16502, doi:10.1029/2012GL052676

Stuecker, M. F., Bitz, C. M., Armour, K. C., Proistosescu, C., Kang, S. M., et al. (2018). Polar amplification dominated by local forcing and feedbacks. *Nature Climate Change* 8, 1076–1081. https://doi.org/10.1038/s41558-018-0339-y

Turner, D. D., & Mlawer, E. J. (2010). Radiative heating in underexplored bands campaigns (RHUBC). *Bulletin of the American Meteorological Society*, 91(7), 911–924. https://doi.org/10.1175/2010BAMS2904.1

Turner, D. D., Ackerman, S. A., Baum, B. A., Revercomb, H. E., & Yang, P. (2003). Cloud phase determination using ground-based AERI observations at SHEBA. *Journal of Applied Meteorology*, 42(6), 701-715. https://doi.org/10.1175/1520-0450(2003)042<0701:CPDUGA>2.0.CO;2

Vihma, T. (2014). Effects of Arctic Sea Ice Decline on Weather and Climate: A Review. *Surveys in Geophysics,* 35, 1175–1214. https://doi.org/10.1007/s10712-014-9284-0

Yang, P., Mlynczak, M.G., Wei, H., Kratz, D.P., Baum, B.A., et al. (2003). Spectral signature of ice clouds in the far-infrared region: Single-scattering calculations and radiative sensitivity study. *Journal of Geophysical Physics,* 108, 4569. https://doi:10.1029/2002JD003291

Chapter 2 The Spectral Dimension of Arctic Outgoing Longwave Radiation and Greenhouse Efficiency Trends from 2003-2016

2.1 Introduction

Over the last several decades, the Arctic has experienced considerable surface warming, the greatest of which has occurred between autumn and spring (Boisvert & Stroeve, 2015). Additionally, Arctic sea ice extent has declined steadily in the era of global satellite observations (Parkinson & Cavalieri, 2008; Cavalieri & Parkinson, 2012), with September experiencing record lows in 2007 and 2012 (Stroeve et al., 2012). It is evident that the Arctic climate is shifting into a regime featured with higher surface temperatures and larger expanses of ice-free ocean than observed in previous decades.

In addition to sea ice reduction and surface temperature increase, multiple lines of evidence suggest that the Arctic atmosphere has experienced increases in temperature and humidity in recent decades. Screen and Simmonds (2010a) reported increases in atmospheric temperature throughout all seasons. Serreze et al. (2012), using radiosonde and reanalysis data, found a near Arctic wide increase in precipitable water over the period of 1979-2010. Some studies (e.g. Gong et al., 2017) indicated that changes in atmospheric circulation have increased moisture flux and warm air advection into the Arctic. Recently, it has been suggested that local evaporation, due to a reduction

in sea ice, has also substantially contributed to positive trends in Arctic atmospheric humidity (e.g. Boisvert & Stroeve, 2015; Boisvert et al., 2015a; Screen & Simmonds, 2010a).

The increase in Arctic near-surface temperatures has been conventionally linked to increased ocean absorption of solar radiation in the summer that leads to a delay of the freeze up period and subsequent release of ocean sensible heat during the cold season (e.g. Screen & Simmonds, 2010b). In recent years, it also has been proposed that the enhancement of downwelling longwave (LW) radiative flux due to an increasing water vapor greenhouse effect and atmospheric temperature could contribute to Arctic surface warming. Kapsch et al. (2013) reported that the increase of downwelling LW flux in spring due to increased water vapor could play a direct role in initiating early sea-ice melt. Cao et al. (2017) also found that increasing Arctic water vapor contributed to winter and spring warming. Lee et al. (2017) and Gong et al. (2017) both reported that the pattern of surface-air warming could largely be explained by increases in downwelling LW flux associated with increases in atmospheric water vapor and air temperatures.

Water vapor is the most important greenhouse gas in the atmosphere. The cold Arctic atmosphere generally contains less water vapor than the atmosphere in lower latitudes, and therefore the LW radiative properties of the polar atmosphere can be different. A notable example is the far-IR dirty window around 500 cm^{-1} (Yang et al., 2003), which opens in high latitudes and allows part of the surface emission to reach the top of atmosphere (TOA). This spectral region is completely opaque at lower latitudes (except high-elevation regions such as the Andes Mountains). As the Arctic atmosphere becomes warmer and wetter, the greenhouse effect of the Arctic atmosphere may change accordingly. One metric to quantify the greenhouse effect of an atmosphere-surface column at a frequency ν is spectral greenhouse efficiency, GHE(ν), which is defined as

$$GHE(v) = \frac{F_s^\uparrow(v) - OLR(v)}{F_s^\uparrow(v)} \qquad\qquad\qquad \text{(eq. 2.1)}$$

where OLR(v) is the spectrally resolved outgoing LW flux at the TOA, and $F_s^\uparrow(v)$ is the spectrally resolved LW flux emitted by the surface. The LW broadband version of GHE(v) is the greenhouse efficiency defined in Raval and Ramanathan (1989). Greenhouse efficiency depicts the fraction of surface thermal emission trapped within the atmosphere. The GHE metric involves both the upper and lower boundaries of the atmospheric radiative transfer and thus can describe the atmospheric greenhouse effect in a more informative way than the TOA or surface flux alone.

Increases in atmospheric temperature, humidity, or surface temperature impact both OLR and GHE. Broadband fluxes integrated over the entire LW spectrum are typically used in such an investigation. The spectral fluxes, on the other hand, are underutilized. As far as the TOA spectral flux is concerned, different spectral channels have different weighting functions, which means they have different sensitivities to emission from different parts of the atmosphere. Different spectral channels can also be sensitive to different greenhouse gas species. From this perspective, studying the changes of spectral fluxes has its own merits: it connects the understanding of broadband flux changes with the changes of actual meteorological variables that are responsible for such broadband OLR changes. If only broadband flux is studied, a potential issue is that compensating biases from different spectral bands can lead to a seemingly good agreement between models (or between model and observation) but for the wrong reasons. Such compensations were seen in the evaluation of simulated broadband clear-sky flux by a climate model (e.g. Huang et al., 2006) as well as for longwave radiative feedbacks (e.g. Huang et al., 2014b). The studies of spectral flux, however, can largely avoid issues of compensating biases and make the attribution of radiative flux changes more effective. Therefore, studying the changes in

spectrally resolved Arctic OLR and GHE can lead to more insight into associated changes in surface and atmospheric variables, which hopefully can help indirectly evaluate the relevant impacts on polar surface warming.

This study seeks to use satellite observations and forward radiative transfer calculations to understand the zonal-mean changes of clear-sky spectral OLR and GHE in the Arctic over the past decade as well as their connection to the changes in atmospheric temperature, humidity, and surface temperature. Section 2 describes the data used in this study and the methodology. Section 3 presents the main results which is followed by further discussions and conclusions in Section 4.

2.2 Data and Methods

2.2.1 AIRS Observation and Measurement

The Atmospheric Infrared Sounder (AIRS) is an infrared grating spectrometer aboard the NASA AQUA satellite that was launched in May 2002. The sun-synchronous orbit of the AQUA satellite has an equatorial crossing time at 1:30 and 13:30 local time. AIRS is a cross-track scanning instrument with a swath range of -49° to 49° in viewing zenith angle and a field of view (FOV) of 1.1°, which corresponds to a 13.5-km nadir footprint. AIRS records spectra at 2378 channels within three bands (3.74-4.61 µm; 6.20-8.22 µm; 8.8-15.4 µm) spanning the thermal IR and near IR and has a spectral resolving power of $\lambda/d\lambda = 1200$ (Aumann et al., 2003; Chahine et al., 2006). Its radiometric accuracy is <0.3 K for a 250 K brightness temperature target (Pagano et al., 2003) and its spectral accuracy is <0.01 dv, where dv is the full-width at half-maximum of the channel (Gaiser et al., 2003). Since the beginning of its operation, AIRS has exhibited excellent stability over the years. Aumann et al. (2006) estimated the stability to be better than 16 mK yr^{-1} and the estimate was updated to be ~4 mK yr^{-1} by Aumann and Pagano (2008).

2.2.2 The Spectral Longwave Flux Derived from Collocated AIRS and CERES

Observations

This study uses spectrally resolved fluxes derived from collocated AIRS and CERES observations (for brevity, hereafter referred as observed spectral flux). The algorithm to derive the observed spectral flux has been described in detail in Huang et al. (2008; 2010; 2014a) and Chen et al. (2013b). In brief, the AIRS radiances within two thermal-IR bands (6.20-8.22 µm and 8.8-15.4 µm) are used in the derivation. The scene type info is taken from the collocated CERES SSF (Single Satellite Footprint) data product and a spectral anisotropic distribution model (ADM) was developed for each scene type defined in the CERES SSF. Spectral flux at each AIRS channel can be estimated by applying the spectral ADM to the AIRS spectrum collocated with a CERES FOV. Then a multiple linear regression scheme based on the principal component decomposition is used to estimate the spectral flux over the spectral regions not covered by the AIRS observations. As a result, spectral fluxes over each 10 cm^{-1} interval for the entire LW spectrum can be derived from the collocated AIRS and CERES observations. Note that only the CERES SSF ancillary information about the scene type of each collocated AIRS and CERES footprint is used in the derivation of the spectral fluxes. The collocated CERES radiometric measurements and CERES broadband OLR have not been used in the derivation of spectral fluxes at all. Satisfactory comparisons with the CERES OLR at the footprint level and at the monthly gridded average over multiple years were demonstrated in Huang et al. (2008; 2010; 2014a) and Chen et al. (2013b). Such footprint-level spectral fluxes were further averaged onto 2º latitude by 2.5º longitude grids to form monthly averages for both all-sky and clear-sky observations. The monthly mean of clear-sky spectral flux is an average of the spectral flux from all collocated AIRS and CERES FOVs

deemed as clear sky by the CERES SSF algorithm, i.e. the coincident MODIS pixel-level cloud coverage within the FOV being less than 0.1% (Geier et al., 2001; Loeb et al., 2005).

2.2.3 AIRS Version 6 Retrievals

The monthly-mean surface skin temperature (T_s), atmospheric temperature (T_{atm}) and specific humidity (q_{H2O}) profiles from the AIRS Version 6 Level-3 (L3) monthly (AIRS+AMSU-A) data products (Olsen. 2017) are used to generate synthetic spectral fluxes and to investigate changes in Arctic atmosphere and surface conditions from November 2002 - October 2016. The AIRS sounding suite can derive up to 324,000 vertical profiles of T_{atm} and q_{H2O} per day. Error estimates are performed for each retrieval at each vertical level in which quality control (QC) flags are assigned. Retrievals are reported on the native ~45km AMSU-A footprint resolution (3×3 AIRS FOVs) and only included in the L3 monthly mean data and binned into 1°×1° grid cells if data are flagged as good (QC = 1) or best (QC = 0) quality. Atmospheric temperature profiles are provided at 24 levels from 1000 hPa to 1 hPa and the moisture profiles at 12 vertical levels from 1000 hPa to 100 hPa. Susskind et al. (2014) provides a detailed explanation of V6 retrieval procedure and error estimate methodology. The AIRS system was designed to retrieve T_{atm} with 1 K of root mean square uncertainty in 1-km layers in the troposphere and q_{H2O} with 15% absolute uncertainty per 2-km layer. The AIRS T_{atm} and q_{H2O} profiles have been validated against various in situ observations and satellite measurements, which shows AIRS has met these prelaunch specifications (Fetzer et al., 2006; Yue et al., 2013).

2.2.4 PCRTM Simulation

The Principal Component Based Radiative Transfer Model (PCRTM) was developed by Liu et al. (2006). It is used here as the forward model to simulate clear-sky spectra. The PCRTM

does fewer monochromatic radiative transfer calculations than a line-by-line radiative transfer model, while results for other frequencies are predicted based on the correlations between radiances over different frequencies. It has been validated against the line-by-line radiative transfer model (LBLRTM) with a root-mean-square error of less than 0.4 K (Liu et al., 2006). Based on the PCRTM, Chen et al. (2013a) developed a simulator that can calculate spectral radiance or flux using global-scale meteorological fields from climate model simulations, reanalyses and satellite retrievals in a computationally affordable way. The details of the simulator can be found in Chen et al. (2013a), and it has been used in other published studies (e.g., Huang et al., 2014b; Bantges et al., 2016; Pan et al., 2017; Chen et al., 2018). The same simulator package is used in this study.

Daytime and nighttime monthly-mean profiles of T_{atm}, q_{H2O}, ozone and T_s from AIRS L3 data are fed into the PCRTM simulator to compute monthly-mean clear-sky spectral radiances at the diffusive angle (i.e. $\cos\theta=1/1.66$, where θ is view zenith angle) with a spectral resolution of 1 cm^{-1}. The same approach of using monthly-mean profiles in the spectral simulation has been adopted by previous trend studies of spectral radiances as well (e.g. Huang and Ramaswamy 2009; Feldman et al., 2011; Feldman et al., 2015). All calculations use latitude and season dependent profiles of CH_4, CO, and N_2O from McClatchey et al. (1972). For each month, the CO_2 vertical profiles are scaled by the observed CO_2 mixing ratio of the same month as compiled by NOAA Earth System Research Laboratory. All calculations use the surface spectral emissivity dataset from the Advanced Spaceborne Thermal Emission Reflection Radiometer (ASTER) Spectral Library version 2.0 (Baldridge et al., 2009). The surface type on each grid is determined based on the 1-km resolution land surface coverage dataset from the U.S. Geological Survey (Loveland et al., 2000). The spectral fluxes are then derived by multiplying the simulated monthly-mean spectral radiances by a factor of π, commonly referred as the diffusivity approximation (Elsasser,

1942). To be comparable with the spectral interval in the observed spectral flux described in subsection 2.2, the synthetic spectral fluxes are also summed to the 10 cm^{-1} spectral interval.

In addition, we also conducted three separate sets of spectral OLR calculations for sensitivity studies. These simulations are performed to further understand how q_{H2O}, T_{atm}, and T_s respectively affect the trends in spectral OLR and GHE. Each sensitivity simulation is identical to the full simulation except that only one of the three listed geophysical variables is allowed to vary from year to year, while the values of the other two variables are fixed.

2.2.5 Selection of Months

As mentioned in subsection 2.2, the CERES clear-sky FOV is identified using a cloud-fraction threshold (MODIS cloud coverage within a CERES FOV < 0.1%). It is well known that Arctic cloud cover can be extensive and persist throughout the entire year, with total cloud fraction attaining its maximum in the fall and minimum in the late winter and early spring (e.g. Kato et al., 2006, Liu et al., 2012). In order to obtain meaningful zonal-mean trends for clear-sky observations, a sufficient fraction of clear-sky scenes should be available for a given month and each latitudinal zone examined in the study. It should be noted that the fraction of clear-sky footprints seen by CERES (with respect to the total number of CERES footprints) is not entirely equivalent to the clear-sky fraction seen by CERES because a cloudy CERES footprint can be partly clear-sky as well. Only observations from collocated clear-sky footprints are counted here.

Figure 2.1 shows the percentage of area without a single collocated clear-sky AIRS and CERES observation in a given month from November 2002 to October 2016 for every 2° latitudinal band in the Arctic. From October to February, i.e., late fall to winter, the percentage of area without clear-sky observations ranges from 15% to 100% and increases rapidly north of ~75°N. North of 85°N, the clear-sky occurrence is drastically reduced for all calendar months. Therefore, in this study, we do not analyze data from October to February. Instead, we analyze the trends for three representative months from 2003 to 2016, i.e., March and September (the beginning and ending months of melting season, respectively) and July (the peak of the summer
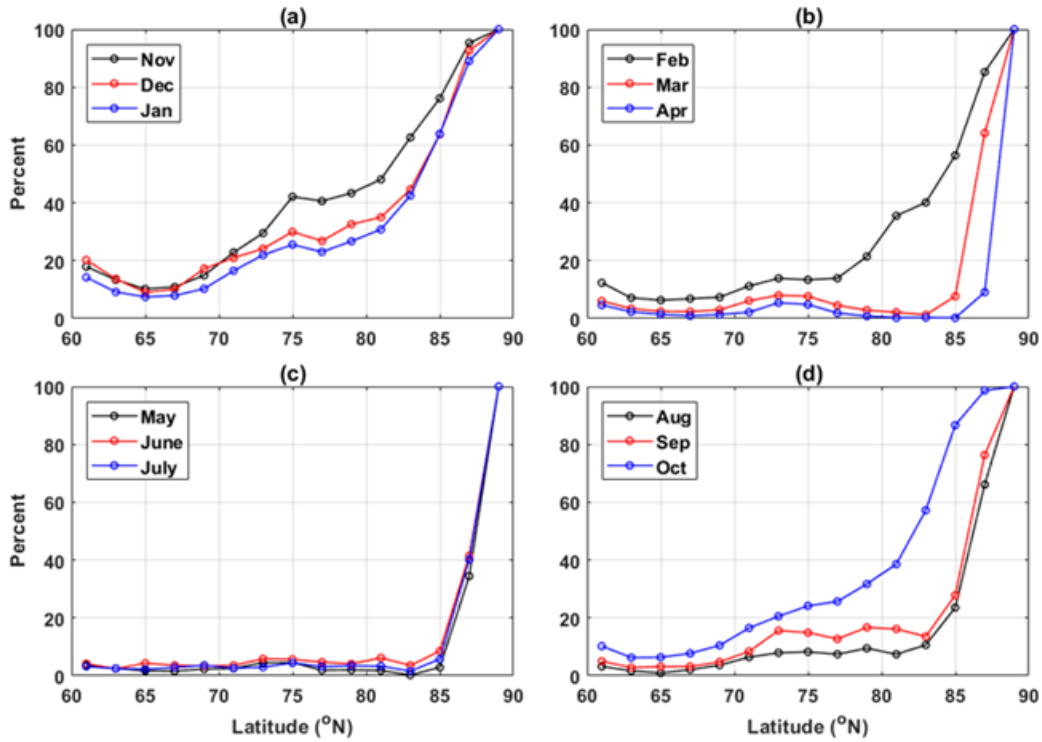
Figure 2.1. Percent of area within each 2° latitudinal zone that has no single clear-sky FOV from the collocated AIRS and CERES observations. The results are shown for each calendar month.

season), and limit our studies to 60-85°N. Key features of Arctic seasonality (e.g. TOA radiation, surface energy processes, and sea ice states) are well represented by the three months (Serreze, 2007). The percentage of area without clear-sky observations, for March and July, is less than 10%

for all the latitudes up to 85°N. For September, it is less than 10% up to 71°N, less than 20% up to 83°N, and less than 30% at 85°N (Figure 2.1d).

2.2.6 Spectral GHE Calculation and Linear Trend Analyses

To compute the clear-sky spectral GHE, the spectral radiative fluxes emitted by the surface, $F_s^{\uparrow}(v)$, are first derived using AIRS L3 T_s and the same spectral surface emissivity dataset described in subsection 2.4. Then, the spectral GHE is computed according to Eq. (1) using such $F_s^{\uparrow}(v)$ and the TOA spectral OLR from either the observations (i.e. collocated AIRS and CERES) or the PCRTM simulations based on the AIRS L3 retrievals. The use of AIRS L3 T_s here ensures consistency between simulated spectral GHE and OLR calculations. All trends in this study were computed using the standard linear regression technique and the results were deemed statistically significant at a significance level of 5%.

2.3 Results

2.3.1 Comparisons with Broadband OLR Anomalies and Trends

Figure 2.2 shows all-sky and clear-sky broadband OLR anomalies (top and middle row of Figure 2.2) and zonal-mean clear-sky trends (bottom row of Figure 2.2) derived from the summation of spectral fluxes used in this study, as well as their counterparts directly from the CERES SSF Edition4 products. As mentioned previously, the spectral fluxes were derived from AIRS radiances using only the collocated scene type information from the CERES SSF products and no radiometric measurements from CERES were used in this derivation at all. Therefore, this comparison can be deemed as an independent consistency check between the spectral flux used in this study and the standard CERES broadband products. For both all-sky and clear-sky results, and for all three months examined here, there is a robust agreement between the OLR anomaly time

series for the two data. Additionally, the zonal-mean trends of broadband clear-sky OLR are consistent with each other for all three months. The agreement between the anomalies and zonal-mean trends from both data sets gives us further confidence to examine the spectral details of broadband OLR trends. In the following parts of this section we will first delineate the trends in the relevant AIRS L3 retrievals and then describe the trends in the observed and simulated spectral OLR and spectral GHE. The final part of this section will discuss the sensitivity studies.
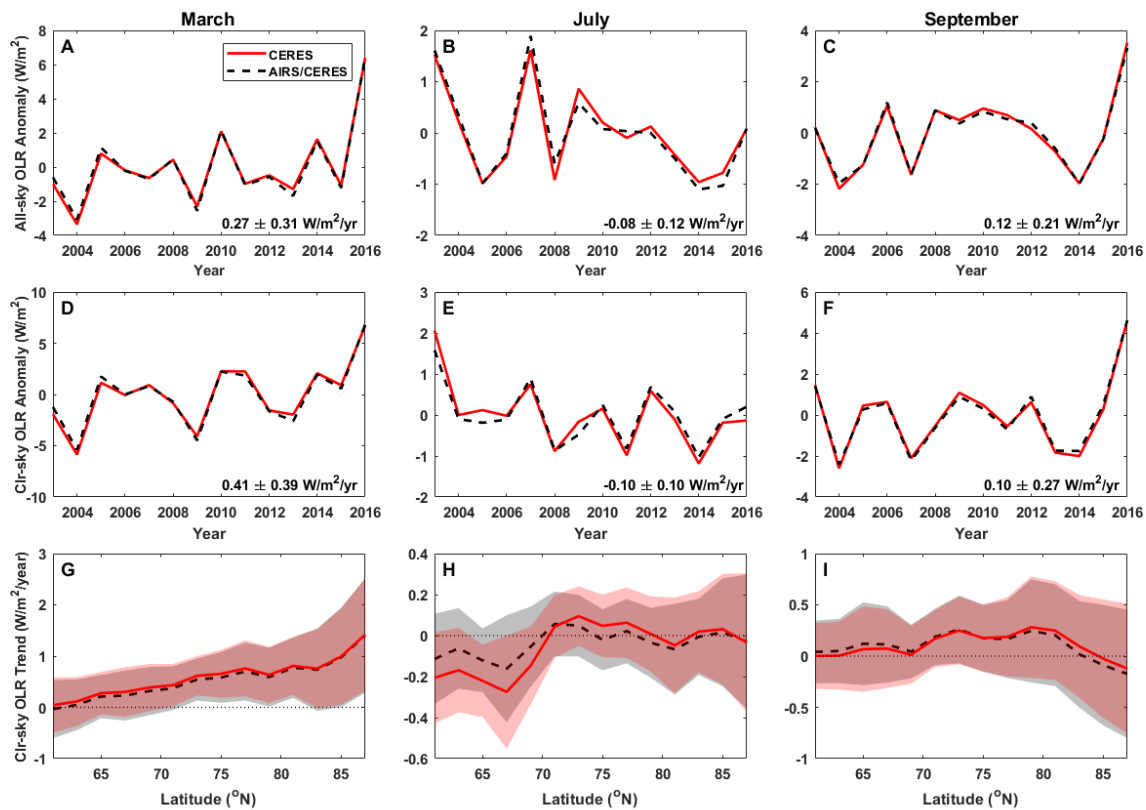
Figure 2.2. (a) Broadband all-sky OLR anomalies averaged over 60°N - 85°N for March. The CERES Edition 4 result is shown as a red solid line and the result based on the spectral fluxes used in this study as a black dashed line. The CERES OLR linear trend is shown with a 95% confidence interval. (b) Same as (a) except for July. (c) Same as (b) except for September. (d)-(f) Same as (a)-(c), respectively, but for clear-sky OLR anomalies. (g) Zonal-mean trends of March broadband clear-sky OLR in the Arctic. The red and black shading represents 95% confidence intervals for the CERES SSF result (red solid line) and the spectral flux product used in this study (black dashed line), respectively. (h) same as (g) except for July. (i) same as (g) except for September.

2.3.2 Atmospheric Temperature, Humidity, and Surface Temperature Trends

Figure 2.3 shows zonal-mean trends of AIRS L3 T_{atm}, q_{H2O}, and T_s for March, July, and September, respectively. For comparison, T_s trends from the European Centre of Medium-Range Weather Forecasts Era-Interim reanalysis (Dee et al., 2011) are also shown in Figure 2.3. The trends of vertical profiles are plotted up to 500 hPa as no statistically significant trends are found for temperature and humidity above this level.
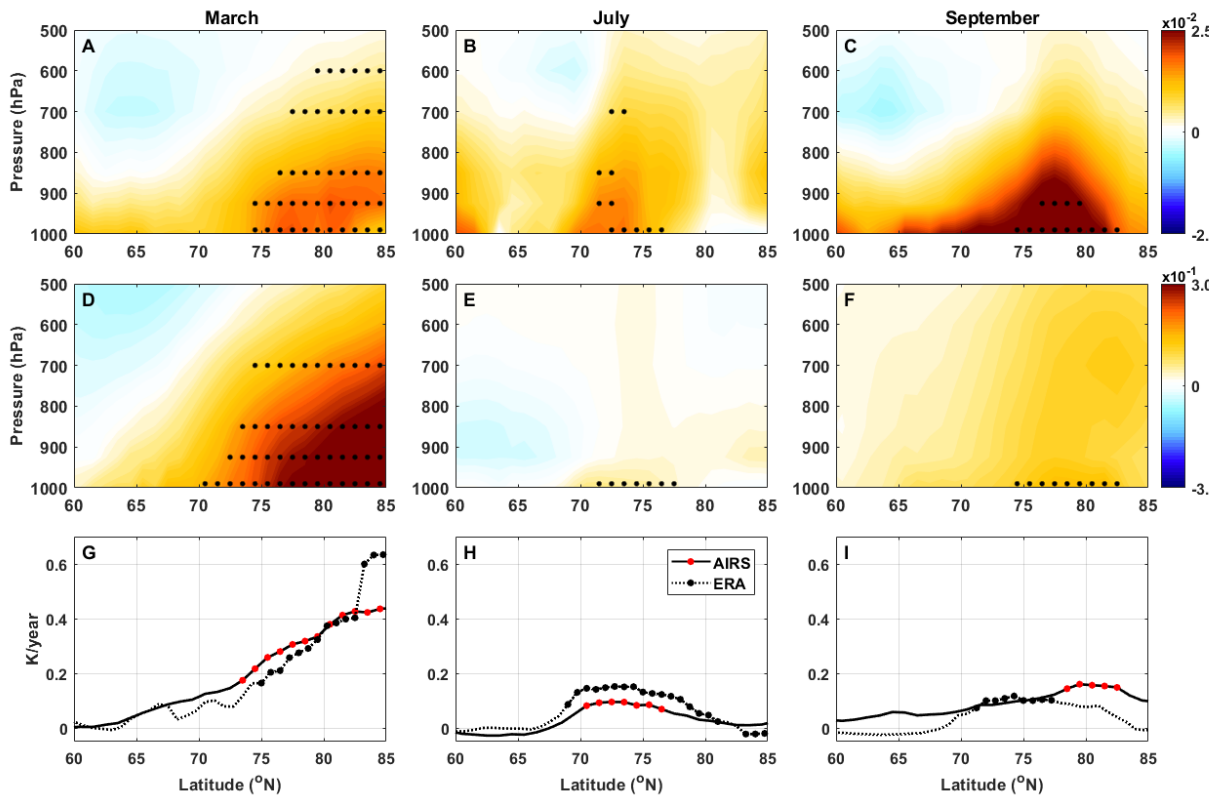
Figure 2.3. (a)-(c) Zonal-mean trends of q_{H2O} from AIRS L3 retrievals for March, July, and September, respectively. The markers indicate statistically significant results (α=0.05). (d)-(f) Same as (a)-(c) except for trends of T_{atm}. (g)-(i) Same as (a)-(c) except for trends of Ts. Solid lines are based on AIRS L3 retrievals and dashed lines on ECMWF ERA-Interim reanalysis. Solid circles indicate significant trends in (g)-(i).

Atmospheric temperature in March exhibits statistically significant trends northward of $70°N$ and can be as large as 0.35 K/year (Figure 2.3d). The largest trends are seen in the planetary boundary layer and extend to 600 hPa. The positive trends of q_{H2O} are ~0.0175 g/kg/year and extend to 500 hPa (Figure 2.3a). AIRS T_s trends for March are much larger than those for July and

September: monotonically increasing from ~0 K/year at 60°N to 0.4 K/year at 85°N. Surface temperature trends from ERA-Interim and AIRS L3 largely agree except for the area north of 83°N (Figure 2.3g). Averaged over the entire Arctic Ocean (70°N - 90°N), the AIRS L3 T_s trend in March is 0.28 K/year, much larger than the trends in July (0.06 K/year) and September (0.11 K/year).

Both July and September show statistically significant T_{atm} increases in the planetary boundary layer from 70 to 80°N (Figure 2.3e and 2.3f), but the magnitude is much smaller than the trends in March. For July, statistically significant q_{H2O} trends are only seen between 70-75°N and extend from surface upwards to 600 hPa, with magnitudes comparable to those in March (Figure 2.3b). In contrast, the lower tropospheric q_{H2O} trends in September are the largest among all three months and peak at more than 0.03 g/kg/year (Figure 2.3c). AIRS T_s trends in July are statistically significant from 70°N to 76°N and range from 0.075 to 0.1 K/year. AIRS T_s trends in September are statistically significant from 78-83°N and the magnitudes are ~0.15 K/year across those latitudes. The ERA-Interim T_s trends in July and September show more disagreement from the AIRS trends than in March, but the magnitudes of the AIRS and ERA-interim T_s trends are largely comparable to each other (Figure 2.3h and 2.3i).

For each respective month examined above, all statistically significant trends of T_{atm}, q_{H2O}, and T_s occur roughly around the same latitudinal zones. Both ERA-Interim and AIRS L3 T_s trends indicate that the surface warming in March is larger than in September and July. Such March warming is consistent with previous findings that, during the last several decades, Arctic surface warming has been greatest during the cold season (e.g. Serreze et al., 2009). A variety of mechanisms have been proposed to explain this seasonally dependent Arctic surface warming. One mechanism is related to sea ice-albedo feedback (e.g. Serreze et al., 2009; Simmonds & Simmonds, 2010a, 2010b; Serreze & Francis, 2006; Serreze & Barry, 2011; Stroeve et al., 2012).

For the period studied here, the statistically significant March T_s and T_{atm} trends occur northward of $70°N$ where sea ice coverage is nearly 100% for March in all the years. Therefore, it is unlikely that this mechanism alone can explain the warming in March. Other proposed mechanisms include (1) the change of temperature profiles in the Arctic lower troposphere (e.g., Bintanja et al., 2011 and Pithan et al., 2014) and (2) increased downward LW radiative flux due to dynamic interactions with extra-Arctic circulations (Gong et al., 2017; Lee et al., 2017).

Screen and Simmonds (2010a) reported a relatively small increase in summer atmospheric temperature compared to other seasons during the period of 1989-2008, a feature seen in Figure 2.3e as well. The disagreement between July and September surface temperature trends between the ERA-Interim and AIRS L3 are not entirely clear. Boisvert et al. (2015b) reported that, when compared to a variety of in-situ data, the ERA-Interim surface temperature tends to have twice as large root-mean-square errors as the counterpart from the AIRS L3.

Numerous studies (e.g., Screen & Simmonds, 2010a) have found that increases in Arctic atmospheric water vapor are related to sea-ice reductions, which expose more open water to the atmosphere and facilitates more evaporation. Using AIRS L3 data over the period of 2003-2013, both Boisvert and Stroeve (2015) and Boisvert et al. (2015a) reported positive trends in evaporation rates that peak in the fall season, which is consistent with the fact that the largest atmospheric humidity trends in our analysis are seen in September instead of March or July.

2.3.3 Spectral OLR Trends

Figure 2.4 shows zonal-mean trends of observed all-sky spectral OLR, observed clear-sky spectral OLR, synthetic clear-sky spectral OLR using the AIRS L3 retrievals as input, and the zonal-mean broadband OLR trends as derived from observations or simulations, respectively. As shown in Fig. 2.4d, 2.4h and 2.4l, except for high Arctic in March, the clear-sky broadband OLR

trends are statistically not distinguishable from zero trend at 5% significance level for virtually all latitudes and for the three months. The spectral OLR trends, however, do show significant trends over certain spectral regions for all three months. This further corroborates the merit of examining spectrally resolved fluxes in addition to the broadband fluxes for such a trend analysis.

Both observed and simulated clear-sky spectral OLR trends in March show statistically significant positive trends as large as 1.5×10^{-2} W per m^2 per 10 cm^{-1} per year north of $75°N$ in the mid-IR window (800-1200 cm^{-1}) and far-IR dirty window (400-600 cm^{-1}). A slight difference between observed and simulated trends can be seen in the far-IR and north of $82°N$, where the
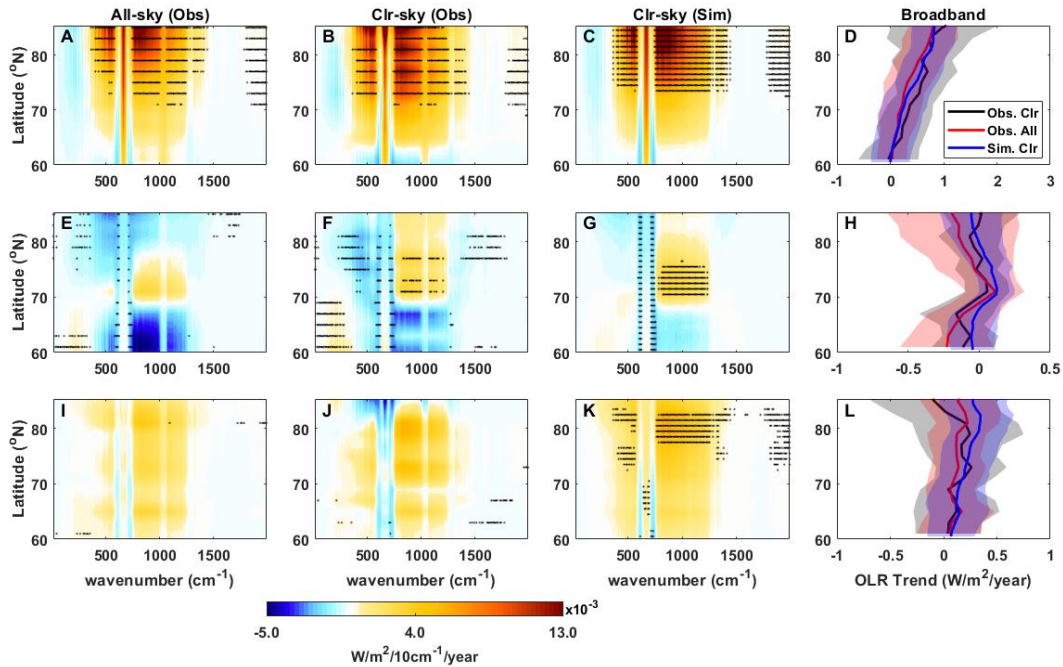
Figure 2.4. (a) Observed zonal-mean trends of March all-sky spectral OLR as a function of latitude in the Arctic region. Stippling indicates statistically significant trends ($\alpha=0.05$). Trends are derived using data from 2003 to 2016. (b) Same as (a) except for observed clear-sky spectral OLR trends. (c) Same as (a) except for simulated clear-sky spectral OLR trends using AIRS L3 retrievals as input to the PCRTM. (d) Zonal-mean trends of observed all-sky (red), observed clear-sky (black), and simulated clear-sky broadband OLR trends (blue). The corresponding color shading indicates 95% confidence intervals for the trends. (e-h) Same as (a-d) except for July. (i-l) Same as (a-d) except for September.

simulated clear-sky spectral OLR trends are still statistically significant, but the observed ones are not. The all-sky spectral OLR trends in general are consistent with the clear-sky spectral OLR trends, but the magnitudes are slightly smaller than their clear-sky counterparts.

The simulated and observed clear-sky spectral OLR trends in July (middle row in Figure 2.4) show agreement in the mid-IR window region for 70-77°N, with statistically significant trends of $\sim 2 \times 10^{-3}$ W per m^2 per 10 cm^{-1} per year. Observed spectral OLR trends also show statistically significant negative trends in the water vapor far-IR band and the water vapor $v2$ band (1300-1900 cm^{-1}) between 75°N and 82°N, as well as positive trends in the far-IR between 60°N and 70°N (Figure 2.4f). These features can also be seen in the simulated spectral OLR trends (Figure 2.4g), but none of them are statistically significant. The observed all-sky spectral OLR trends in July in general show a pattern similar to the clear-sky counterparts (Figure 2.4e), but few trends are statistically significant.

There are little statistically significant trends from the observed all-sky and clear-sky spectral OLR in September (Figure 2.4i and 2.4j). The simulated clear-sky spectral OLR trends in the mid-IR window are statistically significant between 77°N and 83°N (Figure 2.4k). The observed trends over the same region are comparable but not significant. Note such positive trends in the mid-IR window region correlate well with the maximum positive trends of September T_s, $T_{atm,}$ and q_{H2O} in the same latitude zone (Figure 2.3).

2.3.4 Spectral GHE trends

Figure 2.5 shows zonal-mean spectral GHE trends for the same three months. In general, the simulated clear-sky spectral GHE trends agree well with the observed ones. The all-sky spectral GHE trends bear substantial similarity to the clear-sky counterparts, with some differences in terms of statistical significance. For March (top row in Figure 2.5), statistically significant positive GHE trends are seen north of 80°N for both the far-IR bands and the water vapor v2 band in the mid-IR, suggesting an increase of trapped surface emission by the atmosphere over such bands. Moreover, the positive trends here are the largest among all of the GHE trends examined here: at least four

times more than any positive GHE trends seen in July and September. This is consistent with the rapid Arctic warming in late winter and early spring.

For July (middle row in Figure 2.5), statistically significant positive clear-sky GHE trends that range from 1.5×10^{-3} to 3×10^{-3} $year^{-1}$ can be seen from 70 to $80°N$ in both observation and
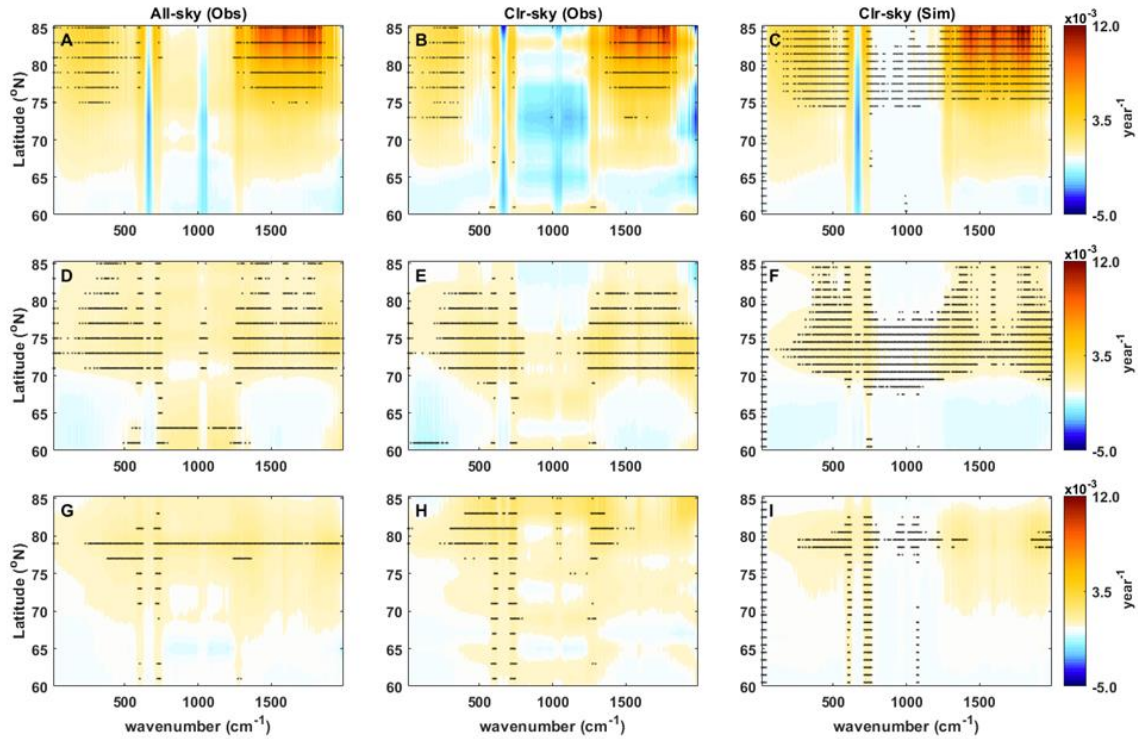
Figure 2.5. (a) Observed zonal-mean trends of March all-sky spectral GHE in the Arctic region. Stippling indicates statistically significant trends ($\alpha=0.05$). Trends are derived using data from 2003 to 2016. (b) Same as (a) except for observed clear-sky spectral GHE trends. (c) Same as (a) except for simulated clear-sky spectral GHE trends. (d-f) Same as (a-c) except for July. (g-i) Same as (a-c) except for September.

simulation results across the water vapor v_2 band and far-IR. For September (bottom row in Figure 2.5), the observed clear-sky GHE trends exhibit few significant trends except for the positive trends above $\sim80°N$ in the far-IR dirty window region and part of the water vapor v_2 band, and across all latitudes for the positive trends in the wings of the CO_2 v_2 band (also commonly known as the CO_2 15 μm band). The simulated trend pattern (Fig. 2.5i) is largely consistent with the observed counterpart.

38

Figures 2.4 and 2.5 consistently show agreement between the spectral trends directly derived from the collocated AIRS and CERES observations and those derived from the synthetic spectra using the AIRS L3 retrievals. This gives us further confidence to carry out sensitivity studies to explore which factors contribute the most to the trends in the OLR and GHE. Meanwhile, it is also clear from Figures 2.4 and 2.5 that the spectral GHE trends have distinctively different patterns from the spectral OLR trends. Given what directly matters to the surface climate is the radiation trapped by the atmosphere, such pattern differences also highlight the merit of analyzing both the TOA flux and the GHE for a better understanding of the changes in the Arctic.

2.3.5 Sensitivity Studies for the Spectral OLR and GHE Trends

As described in Section 2.2, the sensitivity studies were carried out by respectively changing q_{H2O}, T_{atm}, and T_s in the simulations and then computing the zonal-mean trends respectively, the results of which are shown in Figures 2.6-2.8. To focus on the changes of temperature and humidity, the CO_2 concentration is fixed for all the months in the sensitivity simulations and, therefore, the changes in the CO_2 v_2 band will not be discussed here.

For all three months, the trends due to changes of T_s largely dominate the overall trends. Figure 2.3 shows that the March T_s trends north of 75°N are the largest ones among all three months. Accordingly, the spectral OLR and GHE trends north of 75°N due to changes of T_s in March (Figure 2.6c and 2.6f) are also much larger than the trends caused by T_s alone in July and September. For the trends from changing q_{H2O} or T_{atm} alone, as one would expect, the sign of the spectral GHE trends is opposite that of the spectral OLR trends as the denominator in Equation (1) is fixed in such cases. In addition to these common features, there are also several noteworthy features:

(1). For March, between 80°N - 85°N, changing q_{H2O} alone leads to a small but statistically significant positive trend ~1.5×10^{-3} W per m^2 per 10 cm^{-1} per year in the far-IR dirty window. Such positive trends caused by q_{H2O} are only seen for March results. For the other two months, trends caused by q_{H2O} alone are always negative. At high latitudes, the far-IR dirty window is sensitive
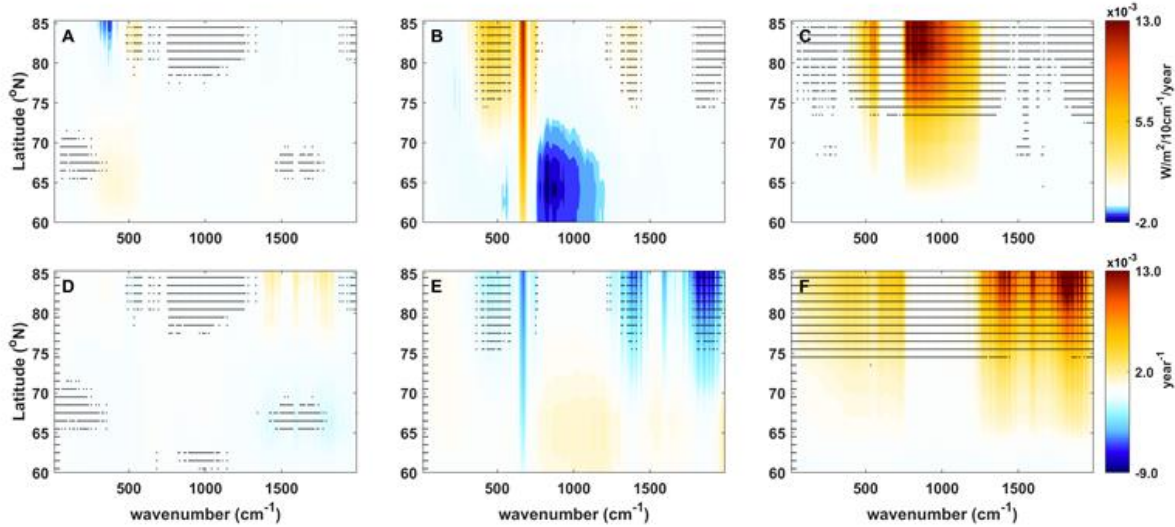
Figure 2.6. (a) The simulated spectral OLR trends in March when only q_{H2O} changes with time. Stippling indicates statistically significant trends (α=0.05). (b) Same as (a) but for changing T_{atm} only. (c) Same as (a) but for changing T_s only. (d)-(f) Same as (a)-(c) but for the simulated spectral GHE trends.

to emission from the lower troposphere as well as surface. Figure 2.3 shows positive q_{H2O} trends over 80°N - 85°N throughout the entire Arctic lower troposphere in March. Normally an increase of q_{H2O} in the troposphere leads to a reduction in OLR. However, if there is a temperature inversion layer in the troposphere, then an increase of q_{H2O} can lead to an increase of spectral OLR for the channels most sensitive to the emissions from the inversion layer. It is well known that the Arctic tends to have lower tropospheric inversions in non-summer months due to the lack of surface heating by the Sun, and the inversion layer can reach as high as 600 hPa. These facts explain why the positive spectral OLR trends due to q_{H2O} change occurring in a tropospheric inversion layer are seen in March but not in July and September.

40

(2). The statistically significant trends caused by T_{atm} alone are only seen in the far-IR dirty window (for March) and in the mid-IR window region (for March and September), two spectral regions that are affected by the lower tropospheric temperature change. For spectral regions sensitive to the temperature in the upper and middle troposphere, no significant trends are obtained. This is consistent with the fact that no statistically significant trends in AIRS L3 temperature exist above 600 hPa (Figure 2.3).

(3). The changes of T_s can lead to statistically significant OLR trends not only in the mid-IR window region but across the water vapor far-IR and v_2 bands, especially for north of 75°N and non-summer months. This highlights the contrast between polar regions and low latitudes. The polar region has much less column water vapor than lower latitudes, especially in the non-summer months; as a result, the atmosphere is not entirely opaque in the water vapor bands and changes of surface emission can impact the changes of spectral OLR over these bands, as previous shown in Chen et al. (2014).

(4). As far as the T_s change is concerned, the sign of the spectral OLR trend is not necessarily opposite to that of the spectral GHE trend. This is different from the cases of T_{atm} or q_{H2O} changing only. This can be understood by differentiating Equation (1.1), which leads to

$$\frac{dGHE(v)}{dt} = \frac{OLR(v)}{F_s^\uparrow(v)} \left[\frac{dF_s^\uparrow(v)/dt}{F_s^\uparrow(v)} - \frac{dOLR(v)/dt}{OLR(v)} \right]$$
(eq. 2.2)

Therefore, the magnitude and sign of $\frac{dGHE(v)}{dt}$ depends on the difference between $\frac{dF_s^\uparrow(v)}{dt}$ and $\frac{dOLR(v)}{dt}$. Note that OLR(v) consists of two components: surface emission transmitted through the atmosphere and the cumulative contribution from the atmosphere, the latter of which remains the same for all spectral regions when only T_s changes. The atmospheric transmittance also does not change in this case. Thus, two possibilities can be expected:

(a) for spectral regions where atmosphere attenuation of surface emission is small (i.e. window band), $\frac{dOLR(v)}{dt}$ is smaller than but comparable to $\frac{dF_s^{\uparrow}(v)}{dt}$. Thus, $\frac{dGHE(v)}{dt}$ will be close to zero even if $\frac{dOLR(v)}{dt}$ is noticeably positive or negative, as the window band shown in panels (c) and (f) of Fig. 2.6-2.8.

(b) for spectral regions where atmosphere attenuation is large (i.e. both water vapor bands in the far-IR and mid-IR where atmospheric opacity is much larger than one), strong attenuation by the atmosphere implies that changes of surface emission have little impact on OLR(v). Therefore, $\frac{dOLR(v)}{dt}$ is nearly zero but $\frac{dGHE(v)}{dt}$ has the same sign as $\frac{dF_s^{\uparrow}(v)}{dt}$, as shown for the water vapor bands in panels (c) and (f) in Fig. 2.6-2.8.
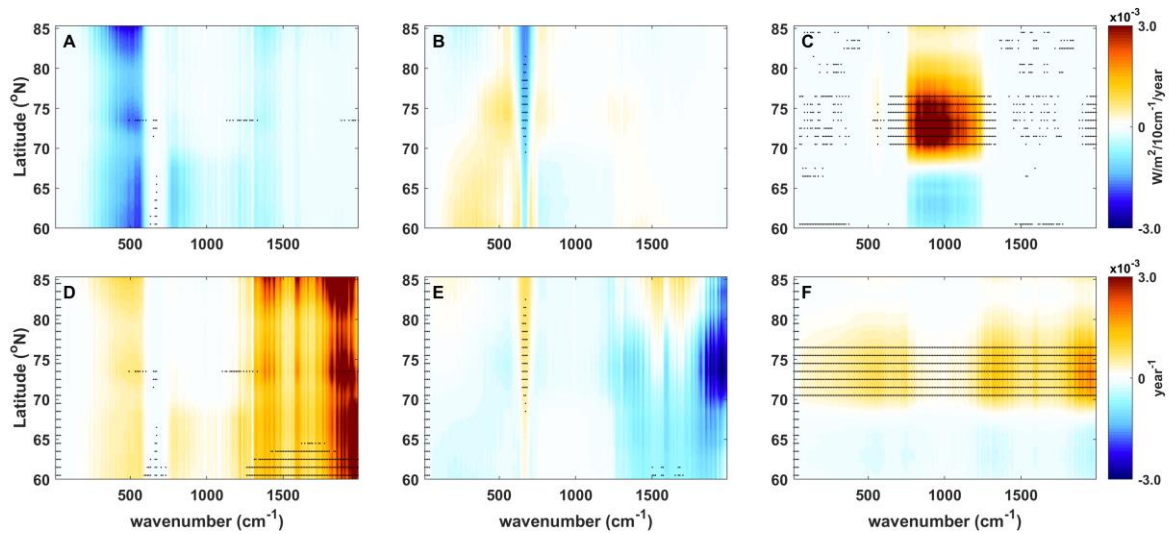
Figure 2.7. Same as Figure 2.6 except for July.
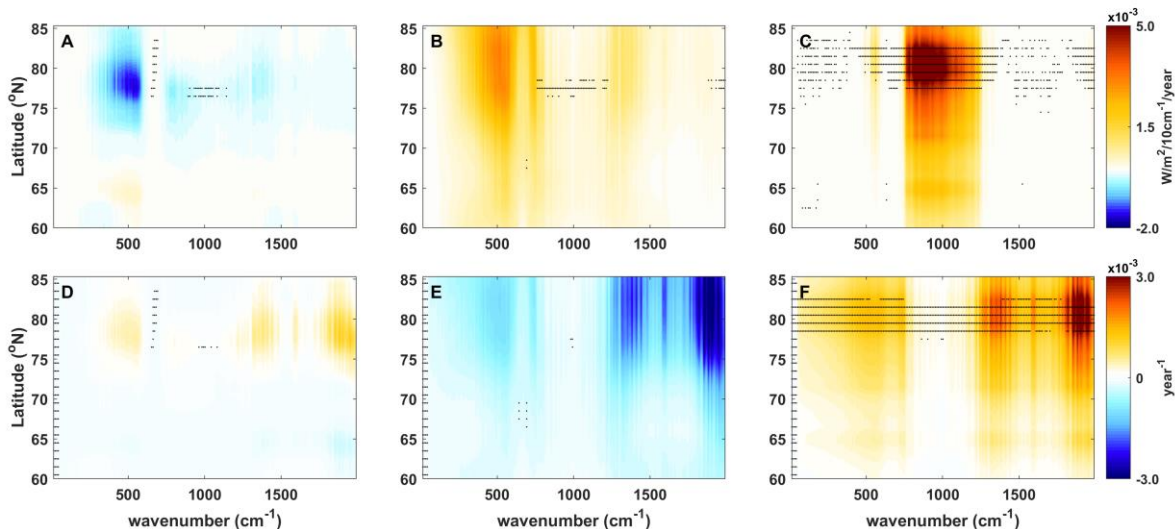
Figure 2.8. Same as Figure 2.7 except for September.

2.4. Discussion and Conclusion

For the first time, observational trends of spectrally resolved radiative flux across the entire LW spectrum in the Arctic are examined using 14 years of AIRS and CERES observations (2003-2016). Simulated trends based on the AIRS L3 retrievals of q_{H2O}, T_{atm}, and T_s agree well with the trends directly derived from the collocated AIRS and CERES observations. The agreement between simulated and observed clear-sky spectral OLR and GHE trends allows for a clear connection to be established between changes (or lack-thereof) in T_s, T_{atm}, q_{H2O} and trends in spectral OLR and GHE. Both March and September exhibit positive trends in spectral OLR over the far-IR dirty window and mid-IR window region for majority of the Arctic; while spectral OLR in July show negative trends over the far-IR dirty window and a mix of positive and negative trends in the mid-IR window region at different latitudes of the Arctic. The spectral GHE trends show an increase of clear-sky greenhouse efficiency in July across the water vapor v_2 band and far-IR for 70-80°N, and a much larger increase of clear-sky greenhouse efficiency occurs in March for

43

regions north of 80°N. Further sensitivity studies reveal that T_s contributes much more than T_{atm} and q_{H2O} to the spectral OLR and GHE trends, while the contributions from the latter two are also discernible over many spectral regions (e.g., the negative trends of spectral flux over the far-IR dirty window in July).

The results of this study support previous findings that the Arctic climate is shifting to a warmer and wetter state and such shift exhibits a strong dependence on season, highlighting the need to understand the changes in each seasonal separately instead of a simple examination of annual-mean statistics. A salient example is that the increase of q_{H2O} leads to an increase of OLR in the far-IR dirty window in March (due to the existence of temperature inversion layer) but a decrease of OLR in the same spectral region in July and September. Even though the T_s change dominates the spectral OLR and GHE changes over many spectral bands, the contributions from T_{atm} and q_{H2O} changes are not negligible or can even be dominant (e.g. q_{H2O} for the July far-IR window OLR trend). Therefore, by a careful selection of spectral regions and comprehensive uncertainty analysis, it might be possible to use spectrally resolved flux observations to monitor changes of q_{H2O} and T_{atm}, especially those in the lower troposphere. Such inferred secular changes in q_{H2O} and T_{atm} can then be used to corroborate the change of downward LW flux at surface, which has direct relevance to the trend of sea-ice melt and can help improve understandings of the actual mechanisms for polar amplification.

This study is focused on the trends in clear-sky spectral OLR and GHE. Due to the complexity and challenges of cloud retrievals at high-latitudes, we did not attempt to simulate cloudy spectra and analyze all-sky spectral trends. The all-sky trends from observations shown in Figures 4 and 5 are similar to their clear-sky counterparts to a large extent, but differences do exist in terms of magnitude and statistical significance. These differences offer some clues to further

infer cloud secular changes from all-sky spectral OLR and GHE data, likely in the conjunction with cloud observations from active sensors such as CloudSat or CALIPSO, as well as with long-term in-situ observations such as those from DoE ARM sites in the Arctic.

References:

Aumann, H. H., Broberg, S., Elliott, D., Gaiser, S., & Gregorich, D. (2006). Three years of Atmospheric Infrared Sounder radiometric calibration validation using sea surface temperatures. *Journal of Geophysical Research: Atmospheres*, 111(D16), 8. https://doi.org/10.1029/2005jd006822

Aumann, H. H., Chahine, M. T., Gautier, C., Goldberg, M. D., Kalnay, E., McMillin, L. M., et al. (2003). AIRS/AMSU/HSB on the aqua mission: Design, science objectives, data products,

and processing systems. *Ieee Transactions on Geoscience and Remote Sensing*, 41(2), 253-264. https://doi.org/10.1109/tgrs.2002.808356

Aumann, H. H., & Pagano, T. S. (2008). *Using AIRS and IASI data to evaluate absolute radiometric accuracy and stability for climate applications*. Paper presented at Conference on Atmospheric and Environmental Remote Sensing Data Processing and Utilization IV - Readiness for GEOSS II, Spie-Int Soc Optical Engineering, San Diego, CA.

Baldridge, A. M., Hook, S. J., Grove, C. I., & Rivera, G. (2009). The ASTER spectral library version 2.0. *Remote Sensing of Environment*, 113(4), 711-715. https://doi.org/10.1016/j.rse.2008.11.007

Bantges, R. J., Brindley, H. E., Chen, X. H., Huang, X. L., Harries, J. E., & Murray, J. E. (2016). On the detection of robust multidecadal changes in Earth's outgoing longwave radiation spectrum. *Journal of Climate*, 29(13), 4939-4947. https://doi.org/10.1175/jcli-d-15-0713.1

Bintanja, R., Graversen, R. G. & Hazeleger, W. (2011). Arctic winter warming amplified by the thermal inversions and consequent low infrared cooling to space. *Nature Geoscience*, 4, 758–761, https://doi.org/10.1038/NGEO1285

Boisvert, L. N., & Stroeve, J. C. (2015). The Arctic is becoming warmer and wetter as revealed by the Atmospheric Infrared Sounder. *Geophysical Research Letters*, 42(11), 4439-4446. https://doi.org/10.1002/2015gl063775

Boisvert, L. N., Wu, D. L., & Shie, C. L. (2015a). Increasing evaporation amounts seen in the Arctic between 2003 and 2013 from AIRS data. *Journal of Geophysical Research: Atmospheres*, 120(14), 6865-6881, https://doi.org/10.1002/2015jd023258

Boisvert, L. N., Wu, D. L., Vihma, T., & Susskind, J. (2015b). Verification of air/surface humidity differences from AIRS and ERA-Interim in support of turbulent flux estimation in the Arctic. *Journal of Geophysical Research: Atmospheres*, 120(3), 945-963. https://doi.org/10.1002/2014jd021666

Cao, Y. F., Liang, S. L., Chen, X. N., He, T., Wang, D. D., & Cheng, X. (2017). Enhanced wintertime greenhouse effect reinforcing Arctic amplification and initial sea-ice melting. *Scientific Reports*, 7, 9. https://doi.org/10.1038/s41598-017-08545-2

Cavalieri, D. J., & Parkinson, C. L. (2012). Arctic sea ice variability and trends, 1979-2010. *Cryosphere*, 6(4), 881-889. https://doi.org/10.5194/tc-6-881-2012

Chahine, M. T., Pagano, T. S., Aumann, H. H., Atlas, R., Barnet, C., Blaisdell, J., et al. (2006). Improving weather forecasting and providing new data on greenhouse gases. *Bulletin of the American Meteorological Society*, 87(7), 911-+. https://doi.org/10.1175/bams-87-7-911

Chen, X., Huang, X., Dong, X., Xi, B., Dolinar, E. K., Loeb, N. G., Kato, S., Stackhouse, P. W., & Bosilovich, M. G. (2018). Using AIRS and ARM SGP clear-sky observations to evaluate meteorological reanalyses: A hyperspectral radiance closure approach. *Journal of Geophysical Research: Atmospheres,* 123, 11,720–11,734. https://doi.org/10.1029/2018JD028850

Chen, X. H., Huang, X. L., & Flanner, M. G. (2014). Sensitivity of modeled far-IR radiation budgets in polar continents to treatments of snow surface and ice cloud radiative properties. *Geophysical Research Letters*, 41(18), 6530-6537. https://doi.org/10.1002/2014gl061216

Chen, X. H., X. L. Huang, & X. Liu (2013a). Non-negligible effects of cloud vertical overlapping assumptions on longwave spectral fingerprinting studies. *Journal of Geophysical Research: Atmospheres*, *118*(13), 7309-7320. https://doi.org/10.1002/jgrd.50562

Chen, X. H., Huang, X. L., Loeb, N. G., & Wei, H. L. (2013b). Comparisons of clear-sky outgoing far-IR flux inferred from satellite observations and computed from the three most recent reanalysis products. *Journal of Climate*, 26(2), 478-494. https://doi.org/10.1175/jcli-d-12-00212.1

Dee, D. P., Uppala, S. M., Simmons, A. J., Berrisford, P., Poli, P., Kobayashi, S., et al. (2011). The ERA-Interim reanalysis: Configuration and performance of the data assimilation system. *Quarterly Journal of the Royal Meteorological Society*, 137(656), 553-597. https://doi.org/10.1002/qj.828

Elsasser, W. M., 1942: *Heat Transfer by Infrared Radiation in the Atmosphere.* Harvard Meteorological Studies, Vol. 6, Harvard University Press, 107 pp.

Fetzer, E. J., Lambrigtsen, B. H., Eldering, A., Aumann, H. H., & Chahine, M. T. (2006). Biases in total precipitable water vapor climatologies from Atmospheric Infrared Sounder and Advanced Microwave Scanning Radiometer. *Journal of Geophysical Research: Atmospheres*, 111(D9), 14. https://doi.org/10.1029/2005jd006598

Feldman, D. R., Algieri, C. A., Collins, W. D., Roberts, Y. L., &Pilewskie, P. A. (2011). Simulation studies for the detection of changes in broadband albedo and shortwave nadir reflectance spectra under a climate change scenario. *Journal of Geophysical Research: Atmospheres*, 116, D24103, doi:10.1029/2011JD016407

Feldman, D. R., Collins, W. D., & Paige, J. L. (2015). Pan-spectral observing system simulation experiments of shortwave reflectance and long-wave radiance for climate model evaluation. *Geoscientific Model Development*, 8, 1943-1954, https://doi.org/10.5194/gmd-8-1943-2015

 Gaiser, S. L., Aumann, H. H., Strow, L. L., Hannon, S. E., & Weiler, M. (2003). In-flight spectral calibration of the Atmospheric Infrared Sounder. *IEEE Transactions on Geoscience and Remote Sensing*, 41(2), 287-297. https://doi.org/10.1109/TGRS.2003.809708

Geier, E. B., Green, R. N., Kratz, D. P., Minnis, P., Miller, W. F., Nolan, S. K., et al. (2001). *Single satellite footprint TOA/surface fluxes and clouds (SSF) collection document.* Retrieved from https://ceres.larc.nasa.gov/documents/DPC/DPC_current/pdfs/DPC_SSF-Ed4_R5V1.pdf

Gong, T. T., Feldstein, S., & Lee, S. (2017). The role of downward infrared radiation in the recent Arctic winter warming trend. *Journal of Climate*, 30(13), 4937-4949. https://doi.org/10.1175/jcli-d-16-0180.1

 Huang, X. L., Chen, X. H., Potter, G. L., Oreopoulos, L., Cole, J. N. S., Lee, D., et al. (2014a). A global climatology of outgoing longwave spectral cloud radiative effect and associated effective cloud properties. *Journal of Climate*, 27(19), 7475-7492. https://doi.org/10.1175/jcli-d-13-00663.1

Huang, X. L., Chen, X. H., Soden, B. J., & Liu, X. (2014b). The spectral dimension of longwave feedback in the CMIP3 and CMIP5 experiments. *Geophysical Research Letters*, 41(22), 7830-7837. https://doi.org/10.1002/2014gl061938

Huang, X. L., Loeb, N. G., & Yang, W. Z. (2010). Spectrally resolved fluxes derived from collocated AIRS and CERES measurements and their application in model evaluation: 2. Cloudy sky and band-by-band cloud radiative forcing over the tropical oceans. *Journal of Geophysical Research: Atmospheres*, 115, 14. https://doi.org/10.1029/2010jd013932

Huang, X. L., Ramaswamy, V., & Schwarzkopf, M. D. (2006). Quantification of the source of errors in AM2 simulated tropical clear-sky outgoing longwave radiation. *Journal of Geophysical Research: Atmospheres*, 111(D14), 12. https://doi.org/10.1029/2005jd006576

Huang, X. L., Yang, W. Z., Loeb, N. G., & Ramaswamy, V. (2008). Spectrally resolved fluxes derived from collocated AIRS and CERES measurements and their application in model evaluation: Clear sky over the tropical oceans. *Journal of Geophysical Research: Atmospheres*, 113(D9), 16. https://doi.org/10.1029/2007jd009219

Huang, Y., & Ramaswamy, V. (2009). Evolution and Trend of the Outgoing Longwave Radiation Spectrum. *Journal of Climate*, 22, 4637–4651, https://doi.org/10.1175/2009JCLI2874.1

Kapsch, M. L., Graversen, R. G., & Tjernstrom, M. (2013). Springtime atmospheric energy transport and the control of Arctic summer sea-ice extent. *Nature Climate Change*, 3(8), 744-748. https://doi.org/10.1038/nclimate1884

Kato, S., Loeb, N. L., Minnis, P., Francis, J., Charlock, T. P., Rutan, D. A., Clothiaux, E. E., Sun-Mack, S. (2006). Seasonal and interannual variations of top-of-atmosphere irradiance and cloud cover over polar regions derived from the CERES data set. *Geophysical Research Letters,* 33(19), L19804. doi:10.1029/2006GL026685

Lee, S., Gong, T. T., Feldstein, S. B., Screen, J. A., & Simmonds, I. (2017). Revisiting the cause of the 1989-2009 Arctic surface warming using the surface energy budget: Downward infrared radiation dominates the surface fluxes. *Geophysical Research Letters*, 44(20), 10654-10661. https://doi.org/10.1002/2017gl075375

Liu, Y., Key, J. R., Ackerman, S. A., Mace, G. G., & Zhang, Q. (2012). Arctic cloud macrophysical characteristics from CloudSat and CALIPSO. *Remote Sensing of Environment*, 124, 159-173. https://doi:10.1016/j.rse.2012.05.006

Liu, X., Smith, W. L., Zhou, D. K., & Larar, A. (2006). Principal component-based radiative transfer model for hyperspectral sensors: Theoretical concept. *Applied Optics*, 45(1), 201-209. https://doi.org/10.1364/ao.45.000201

Loeb, N. G., et al. (2005), Angular distribution models for top‑of‑atmosphere radiative flux estimation from the Clouds and the Earth's Radiant Energy System instrument on the Terra satellite. Part I: Methodology, *Journal of Atmospheric and Oceanic Technology*, 22(4), 338‑351, https://doi.org/10.1175/JTECH1712.1

Loveland, T. R., Reed, B. C., Brown, J. F., Ohlen, D. O., Zhu, Z., Yang, L., et al. (2000). Development of a global land cover characteristics database and IGBP DISCover from 1 km AVHRR data. *International Journal of Remote Sensing*, 21(6-7), 1303-1330. https://doi.org/10.1080/014311600210191

McClatchey, R., Fenn, R. R., Selby, J., Volz, F., & Garing, J. (1972). *Optical properties of the atmosphere* (Rep. AFCRL-72-0497). Bedford, MA: AIR Force Cambridge Research Laboratories.

Olsen, E. (2017). *AIRS/AMSU/HSB Version 6 Data Release User Guide*. Pasadena, CA: Jet Propulsion Laboratory. Retrieved from https://docserver.gesdisc.eosdis.nasa.gov/repository/Mission/AIRS/3.3_ScienceDataProductDoc umentation/3.3.4_ProductGenerationAlgorithms/V6_Data_Release_User_Guide.pdf

Pagano, T. S., Aumann, H. H., Hagan, D. E., & Overoye, K. (2003). Prelaunch and in-flight radiometric calibration of the Atmospheric Infrared Sounder (AIRS*). IEEE Transactions on Geoscience and Remote Sensing*, 41(2), 265-273. https://doi.org/10.1109/tgrs.2002.808324

Pan, F., Huang, X. L., Leroy, S. S., Lin, P., Strow, L. L., Ming, Y., & Ramaswamy, V. (2017). The stratospheric changes inferred from 10 years of AIRS and AMSU-A radiances. *Journal of Climate*, 30(15), 6005-6016. https://doi.org/10.1175/jcli-d-17-0037.1

Parkinson, C. L., & Cavalieri, D. J. (2008). Arctic sea ice variability and trends, 1979-2006. *Journal of Geophysical Research: Oceans*, 113(C7), 28. https://doi:10.1029/2007jc004558

Pithan, F. & Mauritsen, T. (2014). Arctic amplification dominated by temperature feedbacks in contemporary climate models. *Nature Geoscience*, 7, 181–184 (2014), https://doi: 10.1038/NGEO2071

Raval, A., & Ramanathan, V. (1989). Observational determination of the greenhouse-effect. *Nature*, 342(6251), 758-761. https://doi.org/10.1038/342758a0

Screen, J. A., & Simmonds, I. (2010a). The central role of diminishing sea ice in recent Arctic temperature amplification. *Nature*, 464(7293), 1334-1337. https://doi.org/10.1038/nature09051

Screen, J. A., & Simmonds, I. (2010b). Increasing fall-winter energy loss from the Arctic Ocean and its role in Arctic temperature amplification. *Geophysical Research Letters*, 37, 5. https://doi.org/10.1029/2010gl044136

Serreze, M. C., Barrett, A. P., Slater, A. G., Steele, M., Zhang, J., & Trenberth, K. E. (2007). The large-scale energy budget of the Arctic. *Journal of Geophysical Research*: *Atmospheres*, 112(D11). https://doi.org/10.1029/2006JD008230

Serreze, M. C., Barrett, A. P., & Stroeve, J. (2012). Recent changes in tropospheric water vapor over the Arctic as assessed from radiosondes and atmospheric reanalyses. *Journal of Geophysical Research: Atmospheres*, 117, 21. https://doi.org/10.1029/2011jd017421

Serreze, M. C., Barrett, A. P., Stroeve, J. C., Kindig, D. N., & Holland, M. M. (2009). The emergence of surface-based Arctic amplification. *Cryosphere*, 3(1), 11-19. https://doi.org/10.5194/tc-3-11-2009

Serreze, M. C., & Barry, R. G. (2011). Processes and impacts of Arctic amplification: A research synthesis. *Global and Planetary Change*, 77(1-2), 85-96. https://doi.org/10.1016/j.gloplacha.2011.03.004

Serreze, M. C., & Francis, J. A. (2006). The Arctic amplification debate. *Climatic Change*, 76(3-4), 241-264. https://doi.org/10.1007/s10584-005-9017-y

Stroeve, J. C., Serreze, M. C., Holland, M. M., Kay, J. E., Malanik, J., & Barrett, A. P. (2012). The Arctic's rapidly shrinking sea ice cover: A research synthesis. *Climatic Change*, 110(3-4), 1005-1027. https://doi.org/10.1007/s10584-011-0101-1

Susskind, J., Blaisdell, J. M., & Iredell, L. (2014). Improved methodology for surface and atmospheric soundings, error estimates, and quality control procedures: The Atmospheric Infrared Sounder science team version-6 retrieval algorithm. *Journal of Applied Remote Sensing*, 8, 33. https://doi.org/10.1117/1.jrs.8.084994

Yang, P., Mlynczak, M. G., Wei, H., Kratz, D. P., Baum, B. A., Hu, Y. X., et al. (2003). Spectral signature of ice clouds in the far-infrared region: Single-scattering calculations and radiative sensitivity study. *Journal of Geophysical Research: Atmospheres*, 108(D18), 15. https://doi.org/10.1029/2002jd003291

Yue, Q., Fetzer, E. J., Kahn, B. H., Wong, S., Manipon, G., Guillaume, A., et al. (2013). Cloud-state-dependent sampling in AIRS observations based on CloudSat cloud classification. *Journal of Climate*, 26(21), 8357-8377. https://doi.org/10.1175/jcli-d-13-00065.1

Chapter 3 Evaluation of AIRS Cloud Phase Classification over the Arctic Ocean Against Combined CloudSat-CALIPSO Observations

3.1 Introduction

The Arctic is an important component of the global climate system, and changes in this region can have far-reaching impacts. Recent trends in surface-air warming (e.g., Boisvert & Stroeve, 2015; Peterson et al., 2019) and sea ice decline (Cavalieri & Parkinson, 2012) indicate that knowledge of the Arctic surface energy budget is critical for understanding future changes in the region. The radiative effects of clouds can modify the surface climate in the Arctic, particularly through infrared (IR) warming that occurs during most of the year (Intrieri et al., 2002). In the summertime, clouds modulate the amount of solar radiation absorbed by the Arctic ocean (Kay & L'Ecuyer, 2013). The phase of a cloud, i.e., whether it is composed of liquid droplets, ice particles, or both, plays a critical role in the radiative impact of the cloud on surface climate. Liquid clouds tend to have a higher opacity and contribute more to IR warming of the surface than ice clouds (Shupe & Intrieri, 2004; Cesana et al., 2012). Moreover, liquid droplets tend to be smaller than ice

particles, and thus the cloud albedo can also be strongly impacted by cloud phase (Shupe & Intrieri, 2004).

Arctic clouds are unique compared to those in lower-latitudes, as mixed-phase clouds are ubiquitous in the region and can exist at temperatures as cold as -40°C (Shupe, 2011). Thus, clouds containing liquid water can often exist during the Arctic winter. The complexity of Arctic cloud microphysics and a lack of understanding of the connections between Arctic cloud phase and other geophysical parameters has proved to be a challenge for realistically representing Arctic clouds in coupled climate model simulations. For example, Cesana et al. (2012) showed that the underestimation of liquid cloud occurrence in two climate models, particularly in the Arctic fall and winter, can lead to an underestimation of the frequency of occurrence of "radiatively opaque" states in which downwelling longwave radiation from liquid containing clouds nearly balances the upwelling longwave emission from the surface. This can lead to an overestimation of "radiatively clear" states in which the net surface longwave emission can be 50 to 100 W/m^2 larger than the downwelling longwave emission from the atmosphere, resulting in rapid surface cooling.

As it is extremely challenging to maintain long-term ground observation sites in the harsh Arctic weather, satellite observations are critically needed for the understanding of connections between Arctic cloud phase and other surface and atmospheric parameters. Numerous cloud phase algorithms exist for spaceborne instruments such as AVHRR (Key & Intrieri, 2000), POLDER (Goloub et al., 2000; Riedi et al., 2010), CALIPSO (Hu et al., 2009), MODIS (Baum et al., 2012; Marchant et al., 2016), and the Atmospheric Infrared Sounder (AIRS; Kahn et al., 2014). The A-Train constellation includes a suite of instruments whose measurements can be collocated, and this presents a valuable opportunity to use multiple observations to study Arctic cloud phase and to evaluate the cloud phase algorithm designed for each individual instrument. Instruments like the

CALIPSO lidar (which was present in the A-Train from 2006-2011) provide vertical profiles of cloud phase using lidar backscatter and depolarization (Hu et al., 2009). CloudSat, a 94 GHz cloud profiling radar, orbits the Earth together with CALIPSO, and the combination of CloudSat radar and CALIPSO lidar has also been used to estimate cloud phase (Sassen et al., 2008).

While estimating cloud phase with active sensors is considered a benchmark, such estimates are only available along a narrow track (e.g. 90 m – 100 m track width for CALIPSO). Passive A-train instruments like MODIS and AIRS have larger horizontal fields of view (FOV; 1 km and 13.5 km at nadir, respectively) compared to active sensors, and their cross track scanning allows for coverage of areas that the active sensors miss during an overpass. Passive cloud phase discrimination relies mainly on the differences between ice particles and liquid droplets in terms of either IR absorption or shortwave reflection, or both of them. Infrared cloud phase methods are fundamentally limited when mixed-phase clouds are present (e.g. Baum et al., 2000), which presents a challenge in the Arctic where mixed-phase clouds are ubiquitous. However, because solar illumination is scarce throughout the Arctic year, an IR approach is the only practical option for passively estimating Arctic cloud phase during all seasons.

The MODIS Collection 6 products include both an IR only (Baum et al., 2012) and IR-shortwave (Marchant et al., 2016) cloud phase identification at 1-km spatial resolution. AIRS, which estimates cloud phase with IR radiances only (Kahn et al., 2014), differs from MODIS in that it has coarser spatial resolution (13.5 km at nadir) but much finer spectral resolution and more spectral channels. Kahn et al. (2011) showed that AIRS FOVs that contain both cloudy and clear MODIS pixels tended to lead to cloud phase decision errors or unknown-phase classifications by AIRS. However, the finer spectral resolution of AIRS allows for a selection of channels that are less impacted by water vapor absorption and are more sensitive to the spectrally dependent

differences between liquid and ice extinction of IR radiation; this increases the AIRS sensitivity to cloud phase compared to the MODIS IR only approach (Nasiri & Kahn, 2008). The high spectral resolution and over 17 years of observations from AIRS implies that AIRS could be a useful tool for studying Arctic cloud phase climatology. However, AIRS cloud phase retrievals have not been rigorously evaluated against benchmark active sensors in the Arctic region. Such a study must be undertaken before AIRS cloud phase information can be used for studies of Arctic cloud phase climatology.

Jin & Nasiri (2014) (henceforth referred to as JN14) compared AIRS cloud phase classifications to collocated CALIPSO observations on a global scale. Some of the key findings from their study were: (1) AIRS cloud phase agrees with CALIPSO cloud phase more for single-layer systems compared to multilayer systems; (2) AIRS phase tends to agree more with CALIPSO ice-phase than CALIPSO liquid-phase; (3) AIRS tends to classify most liquid cloud scenes as unknown-phase; and (4) AIRS also tends to classify scenes containing both ice and liquid clouds as unknown-phase. These global-scale statistics revealed much about the AIRS phase algorithm's limitations, but performing such an evaluation with a focus on the Arctic region allows for an assessment of AIRS phase classification in a region characterized by markedly different cloud properties, surface conditions, and atmospheric conditions compared to lower latitudes. Water vapor amount is a critical factor for AIRS cloud phase decisions (e.g. Kahn et al., 2011), and the relatively dry-Arctic atmosphere may cause AIRS Arctic cloud phase classification skill to be different than the global classification skill. Given the lack of knowledge and globally climatic importance of Arctic cloud phase, evaluating AIRS cloud phase retrievals in this region is warranted. Also, such an evaluation can provide information for improving the AIRS cloud phase algorithm, especially in the Arctic.

In this study we systematically evaluate AIRS cloud phase in the Arctic from 2007-2010 against active sensor observations, but there are several differences compared to the JN14 approach that make the evaluation of AIRS cloud phase more targeted to the Arctic region:

(1) We use combined CloudSat and CALIPSO (CCL) observations as opposed to CALIPSO only. JN14's mixed-phase category was based on spatial combinations of ice and liquid CALIPSO pixels within the AIRS FOV because CALIPSO cannot detect the coexistence of ice and liquid in a single cloud layer. However, because the CloudSat radar is sensitive to ice particles within liquid layers that the CALIPSO lidar is sensitive to, the use of CCL allows for an evaluation of AIRS phase classification for mixed-phase cloud scenes that exist on smaller spatial scales than CALIPSO can detect, as mixed-phase horizontal scales of tens of meters are common in high latitudes (e.g., Thompson et al., 2018).

(2) JN14 characterized AIRS phase classification in the presence of multiple cloud layers but assumed that AIRS was most sensitive to the phase of the upper most layers and hence did not focus on the underlying cloud layer's phase. This is a valid assumption when the upper cloud layer is optically thick in the IR (e.g. visible optical depths of ~5 or more), but Arctic clouds can be semitransparent, especially ice clouds, and thus the phase of the underlying cloud layers could influence the AIRS cloud phase classification. Therefore, in this study, we investigate the impact of different combinations of phases in multilayer cloud systems on the AIRS phase classification statistics.

(3) JN14 used cloud amount from the narrow CALIPSO track to separate AIRS FOVs into cloud amount categories. In this study, AIRS cloud phase is instead evaluated using "overcast" groupings of CCL FOVs. To further investigate how cloud amount and cloud phase distributions throughout the entire AIRS FOV impact AIRS cloud phase classifications in the Arctic, a case

study of collocated MODIS cloud observations is used to investigate the connections between MODIS cloud phase and cloud fraction, CCL phase classification, and AIRS phase classification. The case study allows for an evaluation of the representativeness of CCL cloud phase throughout the AIRS FOV. Like JN14, the cloud phase along the CCL track is assumed to be statistically representative of the cloud phase in the AIRS FOV, which may not always be valid, but is a necessary assumption when evaluating AIRS phase with CCL.

(4) Given the unique characteristics of the Arctic climate system, the AIRS phase classification is evaluated over open ocean and sea ice. These surface types can represent opposite extremes in Arctic climate conditions such as atmospheric composition and surface emissivity, and such factors may influence AIRS phase classification skill in the Arctic. The relationship between vertical distributions of CCL cloud phase occurrence and AIRS phase classifications over both surface types is also examined. Lastly, the AIRS and CCL cloud phase occurrences are compared at different Arctic zonal bands during different seasons and, using a composite analysis, the impacts of temperature difference between 1000 and 300 hPa ($\Delta T_{1000\text{-}300}$) and total column water vapor (TCWV) on AIRS and CCL cloud phase occurrence over both surface types are examined.

The rest of the paper is organized as follows: section 3.2 describes the instruments and data used, the collocation methods, and considerations pertaining to CCL cloud amount and layering in the AIRS phase evaluation. Section 3.3 includes the results and discussions of the AIRS phase evaluations, section 3.4 discusses the MODIS case study, and section 3.5 describes the conclusions and suggestions for improving the AIRS cloud phase algorithm with respect to the Arctic.

3.2. Data and Methods

3.2.1 AIRS and its Level 2 Cloud Phase Algorithm

The AIRS instrument is an infrared grating spectrometer that is aboard the Aqua satellite in the A-train constellation. Aqua has a sun synchronous orbit with equatorial crossing times of 1:30 and 13:30 local time. AIRS is a cross track scanning instrument with a with a swath range of -49 to 49° and has FOV of 1.1° which corresponds to a 13.5 km nadir footprint. AIRS records spectra in 2,378 channels in three bands spanning the mid-IR to the near-IR and has a spectral resolving power of $\lambda/d\lambda = 1,200$ (Aumann et al., 2003; Chahine et al., 2006).

AIRS thermodynamic cloud phase, which is available in the AIRS Version 6 (V6) Level 2 (L2) Support Product, is based on a set of brightness temperature difference tests and thresholds using the channels 960 cm^{-1}, 1231 cm^{-1}, 930 cm^{-1}, and 1227 cm^{-1} (Nasiri & Kahn, 2008; Kahn et al., 2014). The tests are used to classify the AIRS FOV as containing liquid, ice, or unknown cloud phase. The phase tests are applied only to AIRS FOVs where the total two-layer effective cloud fraction (ECF) is > 0.01. There are 4 ice tests and 2 liquid tests. The results of all tests are summed and the classification is ice if the value is positive (+1 to +4), unknown if 0, and liquid if negative (-1, -2). The larger negative positive or negative values indicate higher confidence in the phase classification. The individual test results are stored in the field called *cloud_phase_bits* and the sum is reported in the field called *cloud_phase_3x3*.

ECF is retrieved after completion of the AIRS V6 cloud clearing steps by comparing observed and computed radiances in a set of channels that are sensitive to cloud amount and height. ECF is the product of cloud amount and cloud emissivity and is retrieved for up to two layers in the AIRS FOV. This is reported in the AIRS L2 Standard Product. The surface characterization

for the AIRS FOVs used in the study is based on AMSU retrievals of surface emissivity in the 45 km AMSU field of regard. The product is called *MWSurfType* and is an AIRS V6 L2 Standard Product. The generalized surface types are unknown, coastline, open ocean, sea ice, non-frozen land, and frozen land. Only open ocean and sea ice surface types are used in this study.

3.2.2 Combined CloudSat-CALIPSO Cloud Retrievals

The version R04 2B-CLDCLASS-Lidar (CCL; Wang et al., 2013) product is used as the benchmark cloud phase reference. This product uses collocated CloudSat radar reflectively factors and CALIPSO attenuated backscatter coefficients (provided in the LIDAR-AUX 004 auxillary CCL product), where up to 15 CALIPSO footprints can lie within a 1.8 x 1.5 km CloudSat FOV. CALIPSO attenuated backscatter coefficients are averaged to the CloudSat horizontal resolution and the native 30-meter vertical CALIPSO resolution is retained.

Radar and lidar have different sensitivities to cloud properties. The CloudSat 94 GHz radar can penetrate deeper into cloud layers and is sensitive to large ice particles, while the CALIPSO 532nm lidar pulse is more sensitive to cirrus clouds and liquid droplets. By synergizing the instruments, CCL can classify up to 10 layers as either ice, liquid, or mixed-phase. Distinct cloud layers are identified with a separation of ~480m (Marchand et al., 2008). In this study, we only use up to 5 layers because higher layer amounts occur in less than 0.06% of global CCL observations during our study period of 2007-2010 (Wang et al., 2016). The CCL product also provides the number of cloud layers and the cloud base and top heights in each CCL FOV. To avoid potential misidentification of cloudy scenes near the surface, which is called "ground clutter" (Tanelli et al., 2008), we only use CCL cloud layers in which the cloud base lies above 0.5 km.

3.2.3 ERA-5 Total Column Water Vapor and Atmospheric Temperature

Total column water vapor (TCWV) and profiles of atmospheric temperature for January 2007- December 2010 were obtained from European Centre for Medium-Range Weather Forecast (ECWMF) ERA-5 (Hersbach et al., 2018). Data are 1-hourly and at 0.25°x0.25° spatial resolution. Profiles of atmospheric temperature are provided at 37 pressure levels from 1000 hPa to 1 hPa.

3.2.4 MODIS Cloud Property Retrievals

Aqua MODIS Collection 6 (MYDO6_L2) L2 cloud 1-km daytime only cloud mask (*Cloud_Mask_1km*; Ackerman et al., 1998). Discriminating clear sky from clouds with MODIS. J. Geophys. Res., 103(D24), 32141– 32157.) and cloud phase (*Cloud_Phase_Optical_Properties*) from the Cloud Optical Properties Product (Marchant et al., 2016; Platnick et al., 2017) are used in the case study described in section 3.4. The cloud mask flags a pixel as confidently clear, probably clear, probably cloudy, or confident cloudy. The cloud phase product flags a pixel as either ice, liquid, or unknown. It should be noted that the IR-only MODIS thermodynamic cloud phase product is not used at all in this study and thus only daytime MODIS data are used.

3.2.5 AIRS, CCL, and MODIS Collocation Strategy

To collocate CCL and AIRS FOVs, collocation indices during 2007-2010 period from the MEaSUREs Project (Fetzer, 2012) were used. A nearest neighbor approach was used to match CloudSat and AIRS FOVs based on the latitude and longitude pair (Kahn et al., 2008; Yue et al., 2011; Fetzer, 2012). Due to the orbital configuration and viewing geometries of the instruments, CloudSat and CALIPSO FOVs can only overlap with near-nadir AIRS FOVs, and thus only such AIRS FOVs are used in this study. Approximately 15-19 CloudSat (and therefore CCL) FOVs lie within a 13.5 km near-nadir AIRS FOV. The MEaSUREs collocation indices contain the AIRS

granule number, FOV indices, and an indexed array of CCL cloud products. Only AIRS granules falling between 60-90°N are used. Since the CCL orbit is limited to <83°N, the study area is
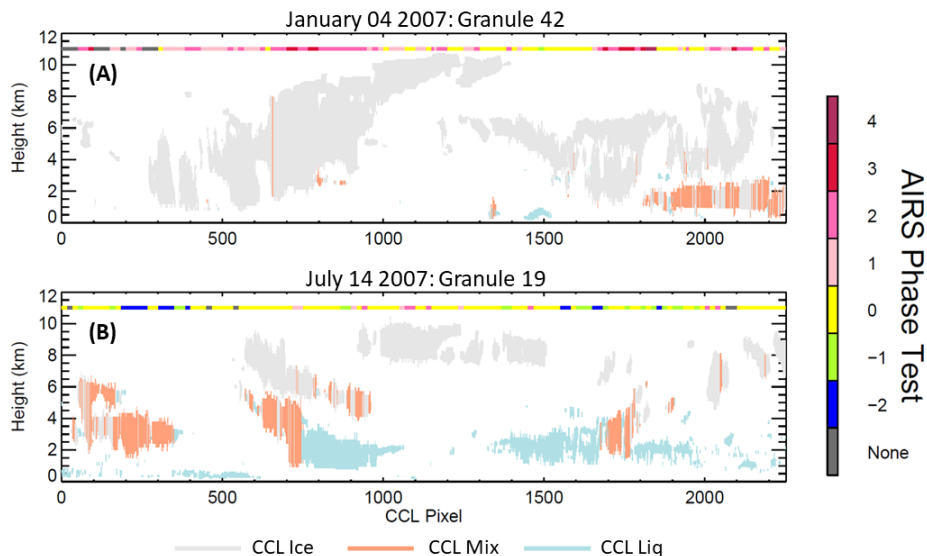
Figure 3.1. (A) Vertical profile of individual cloud layers detected by CCL along an AIRS-CCL collocated ground track on January 4, 2007 from (76.26°N, 106.51°E) to (76.69°N, 1.6°W). The horizontal colored bar at 11 km represents AIRS phase decisions for AIRS FOVs overlapping with groups of CCL FOVs. (B) Same as for (A) except for July 14, 2007 from (80.8°N, 60.62°E) to (63.85°N, 12.1°E).

confined to 60-83°N. This provides a sample set of ~4 million near-nadir AIRS FOVs and ~61 million CCL FOVs over the four-year period. To provide an illustration of the AIRS-CCL collocation strategy, Figure 3.1 shows vertical curtains of CCL cloud phase and AIRS phase decisions that are collocated with groups of CCL FOVs for two separate granules in summer and winter.

For the MODIS case study described in section 3.3.4, 1-km MODIS pixels are collocated within each AIRS FOV where CCL is also collocated in the AIRS FOV during the month of July 2009 for daytime only. The collocation is based on the method developed by Schreier et al. (2010). There are ~200 MODIS 1-km pixels for a 13.5-km nadir AIRS FOV.

3.2.6 Cloud Amount and Layering Considerations for AIRS Cloud Phase Evaluations

3.2.6.1 Selection of CCL Cloud Layering in AIRS FOVs

      Cho et al. (2009) and JN14 both reported that, for MODIS and AIRS respectively, a higher cloud phase classification skill is achieved for single-layer cloud systems. However, multilayer cloud systems occur frequently on a global scale and should not be ignored. Since this study focuses on the Arctic, it is important to first evaluate the frequency of occurrence of different cloud layer amounts in the Arctic. Figure 3.2 shows the relative frequency of occurrence of the cloud layer amount using groups of CCL pixels where ≥90% of the collocated CCL FOVs within the AIRS FOVs are either all covered by single-layer clouds or all covered by two-layer clouds over open ocean and sea ice. These will be referred to as single-layer-overcast and two-layer-overcast CCL FOV groups. Regardless of the surface type, single-layer-overcast systems are the most prevalent (75-80%) while two-layer-overcast systems are the second most common (15-20%). A similar conclusion is drawn using cloud layer numbers from individual CCL FOVs (not shown). CCL FOV groups with more than two layers are scarce in the collocated observations. It is possible that some single-layer clouds detected by CCL may have underlying cloud layers, but these lower layers may not be detected by CCL due to full attenuation of the CALIPSO lidar, which occurs for the cloud layer with a visible optical depth greater than ~3. Given the cloud layering statistics described here, we use single-layer and two-layer CCL FOV groupings in the AIRS phase evaluation.

3.2.6.2 Selection of CCL Cloud Cover in AIRS FOVs

In addition to assessing the consistency of cloud phase classifications between AIRS and CCL, it is also important to assess the qualitative cloud detection consistency of the AIRS and CCL products. Such an evaluation will determine if AIRS cloud detection is consistent with the single-layer-overcast CCL groups, which are the main CCL groups used in the AIRS cloud phase evaluation. Figure 3.3 shows the occurrence of AIRS FOVs within five ECF intervals compared with CCL FOV groups with different cloud amounts. Also, the distribution of AIRS ECF occurrence within two different CCL cloud amount categories is explored. It is important to note that AIRS ECF and CCL cloud amount are physically different and the comparison here is qualitative and relative.
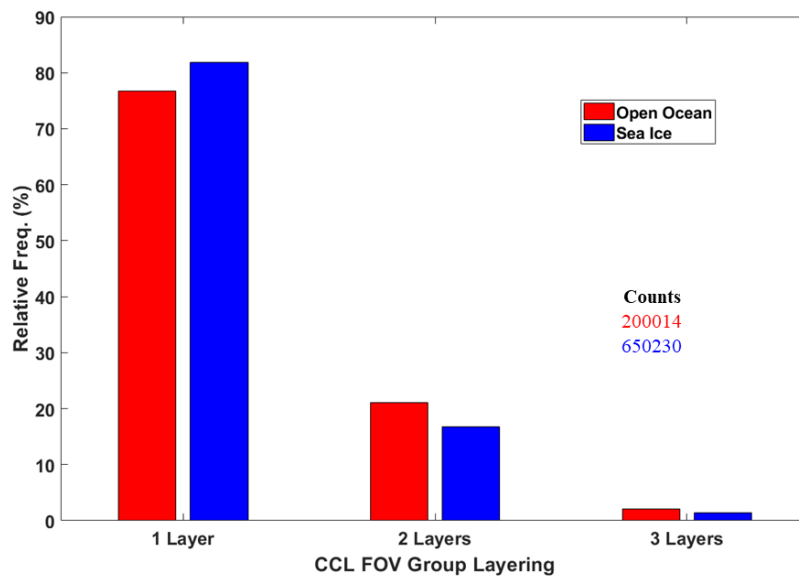
Figure 3.2. Relative frequency of occurrence of overcast CCL FOV groups with a given layering number for sea ice and open ocean. For the layers to be counted, ≥90% of CCL FOVs must detect cloud and must all have the same number of layers. The normalization is with respect to all FOV groups over each surface type, respectively. The counts represent the number of CCL FOV groups included for each surface type, respectively.

Four single-layer CCL cloud amount categories are created for CCL FOV groups within AIRS FOVs: (1) CCL clear-sky when ≥90% of the CCL FOVs indicate no cloud layer; (2) CCL partly-cloudy conditions when between 10% and 90% of CCL FOVs are covered by single-layer or multilayer clouds; (3) the aforementioned single-layer overcast grouping and (4) multilayer

overcast conditions which include all cases where ≥90% of CCL FOVs detect clouds with at least one FOV having more than one cloud layer.
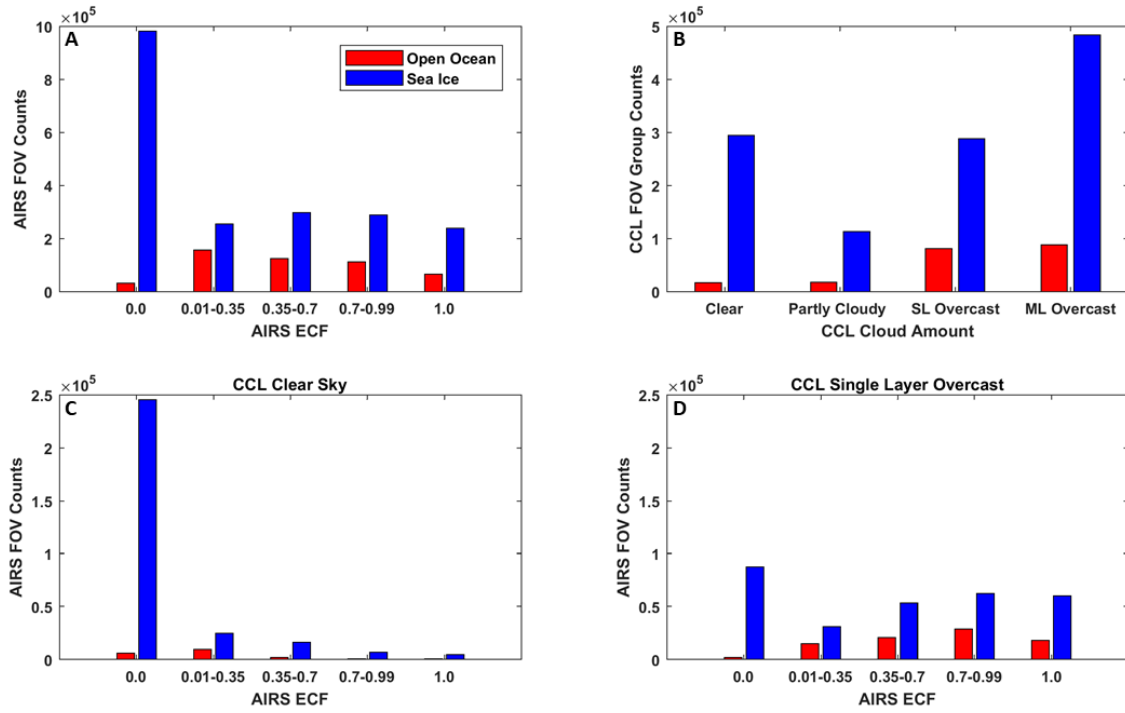
Figure 3.3. (A) Counts of AIRS FOVs over sea ice and open ocean separated based on AIRS effective cloud fraction (ECF). (B) Counts of CCL FOV groups collocated within AIRS FOVs over sea ice and open ocean for four CCL cloud amount categories. CCL clear-sky is defined as ≥90% of the CCL FOVs with no cloud layer. CCL partly cloudy is defined as between 10% and 90% of CCL FOVs with clouds detected. Single layer (SL) overcast is for ≥90% of CCL FOVs detected as single-layer clouds and multilayer (ML) overcast is for ≥90% of CCL FOVs with clouds detected with at least one FOV having more than one layer of cloud. (C) Same as (A) except that only AIRS FOVs corresponding to CCL FOV clear-sky groups are included. (D) Same as (C) expect for the CCL FOV group being SL overcast.

Figures 3.3a and 3.3b show a comparison between counts of AIRS FOVs in five ECF intervals and CCL groups in four CCL cloud amount categories over sea ice and open ocean. Over open ocean, most AIRS FOVs and CCL FOV groups indicate cloud presence, which is consistent with the annual peak of cloud amount occurring in the Arctic summer and fall when open ocean represents a large fraction of surface area. Over sea ice, both AIRS and CCL show that the fractions of cloudy and clear-sky AIRS FOVs, as detected by the AIRS and CCL algorithms respectively, are more comparable. This is consistent with the fact the cloud cover minimum in the Arctic occurs in the winter and spring when there is more sea ice coverage. CCL partly cloudy groups occur less

often than overcast and clear-sky CCL groups, which is consistent with the overall high cloud cover observed in the Arctic throughout the year. Figures 3.3c and 3.3d show AIRS ECF occurrence within the CCL clear-sky and CCL single-layer-overcast groups, respectively (CCL partly cloudy not included). Most AIRS FOVs in which AIRS detects cloud (ECF>0) fall into the CCL overcast category regardless of surface type. However, over sea ice, about half of clear-sky AIRS FOVs (ECF=0) fall into the CCL clear-sky category while the rest fall into the CCL overcast category, and this suggests that AIRS can misidentify cloudy scenes as clear over sea ice from a lack of thermal contrast between the surface and cloud top (Fig. 3.3d). Overall, the single-layer-overcast CCL FOV groupings are associated with AIRS FOVs that will have a cloud phase assigned (i.e. when ECF > 0.01), which further justifies the use of such overcast CCL groupings for AIRS cloud phase evaluation.

3.3. Results and Discussion

3.3.1 Overview of Arctic Cloud Phase Occurrence using Collocated AIRS and CCL FOVs

For an initial comparison between AIRS and CCL Arctic cloud phase, the occurrence of AIRS and CCL cloud phase over sea ice and open ocean is examined using the collocated AIRS-CCL FOV dataset. Different homogenous and heterogeneous-phase categories are defined using collocated single-layer-overcast CCL FOVs within the AIRS FOV as follows: homogenous ice, liquid, and mixed-phase CCL groups when ≥90% of the CCL FOV groups have that phase, respectively, and the heterogeneous-phase groups (ice + liquid, liquid + mixed, ice + mixed) when each phase in any two-phase-mixture makes up 45-55% of the CCL FOV group. The heterogeneous groups are defined similarly to the JN14 mixed-phase category. As was mentioned in section 2.1, the AIRS cloud phase algorithm employs 4 ice tests and 2 liquid tests. The results

of all tests are summed and the classification is ice if the value is positive (+1 to +4), unknown if 0, and liquid if negative (-1, -2).

Figure 3.4 shows the relative frequency of occurrence of cloud phase over sea ice and open ocean for the homogenous and heterogeneous-phase CCL groups (Fig. 3.4b) and by the AIRS phase algorithm in which the AIRS FOVs are subsampled based on collocation with these CCL groups (Fig. 3.4a). Since homogenous-phase CCL occurrence is dominant, only these groups will be discussed here. CCL mixed-phase is the most dominant cloud type over open ocean, where its occurrence is nearly 50%. Over sea ice, the occurrence of CCL mixed-phase is ~40%. Over open
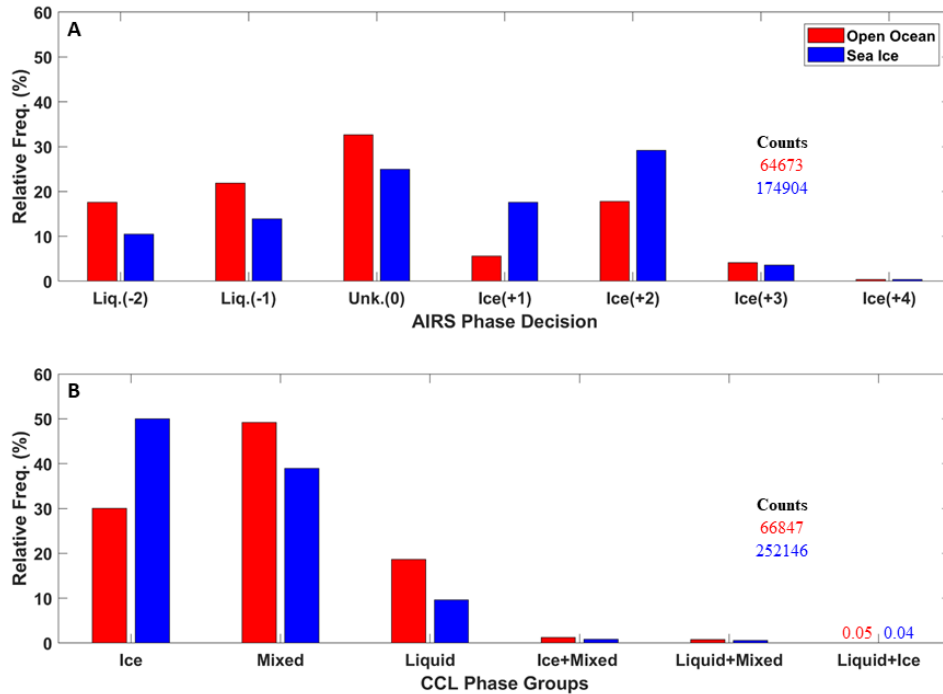
Figure 3.4. (A) Frequency of occurrence of AIRS phase decisions over open ocean and sea ice for only those AIRS FOVs that coincide with a single-layer-overcast homogenous or heterogeneous phase CCL FOV groups. The counts represent the number of AIR FOVs included in the analysis for each surface type, respectively and the normalization is with respect to these counts. (B) Frequency of occurrence of homogenous and heterogeneous phase groupings of single-layer-overcast CCL FOV groups collocated with AIRS. Ice, liquid and mixed-phase groups represent CCL homogenous-phase groups, while the ice+liquid, ice+mixed, and liquid+mixed are for the CCL heterogenous-phase groups. The counts represent the number of CCL FOV groups included in the analysis for each surface type, respectively. The normalization is with respect to these counts. Numerical percentages for each surface type replace bars when the bars are not visible.

ocean, 30% of CCL groups are ice-phase, where ice-phase occurrence for AIRS is 27.9%. Over sea ice, the ice-phase occurrence is 50% for CCL and 50.7% for AIRS ice-phase. For CCL liquid-phase over open ocean, the occurrence is 20%, where for AIRS liquid-phase it is 39.5%. Over sea ice, the CCL liquid-phase occurrence is 10% and 23.3% for AIRS liquid-phase.

When considering AIRS FOVs that are collocated with homogenous-phase CCL groups, the frequency of occurrence of AIRS and CCL ice-phase agree within 2.5%, while AIRS tends to overestimate the occurrence of CCL liquid-phase by as much as 20%. Overall, 27% of the AIRS Arctic cloud phase classifications associated with the homogenous and heterogeneous-phase CCL groups are unknown-phase, and 42% are unknown-phase when considering all AIRS Arctic FOVs with a cloud phase assigned. This prompts a thorough examination of the conditions associated with these unknown-phase classifications as well as other AIRS phase classifications, which will be discussed in the following section.

3.3.2 AIRS Arctic Cloud Phase Evaluations

3.3.2.1 Single Layer Systems

To evaluate AIRS Arctic cloud phase classifications against single-layer-overcast CCL groups, we first assess AIRS classification tendency for various CCL phase groupings and subsequently evaluate AIRS phase classification skill for the Arctic.

Figure 3.5 shows the frequency of occurrence of AIRS phase classifications partitioned based on AIRS cloud phase test summations for single-layer-overcast homogenous and heterogeneous-phase CCL groupings. Overall, the percentage of homogenous-phase CCL groups classified as a particular AIRS phase is not dependent on surface type. AIRS classifies 78% of homogeneous CCL ice-phase groups over open ocean (82.4% over sea ice) as ice-phase and the

rest as unknown-phase (Fig. 3.5a). This high rate of agreement between AIRS and CCL ice-phase scenes is consistent with AIRS being more sensitive to ice-phase than liquid-phase (Kahn et al., 2014), and JN14 reported a similar result for AIRS comparisons with CALIPSO on the global scale. For homogenous CCL liquid-phase groups over open ocean, AIRS classifies 71.5% as liquid-phase (71% over sea ice) and the rest as unknown-phase (Fig. 5b). JN14 found that on a global scale, ~40% of homogenous CALIPSO liquid-phase groups were classified as liquid-phase by AIRS, compared to ~70% in this study. It is possible that a higher fraction of liquid clouds can be classified correctly in the Arctic compared to lower latitudes due to the drier Arctic atmosphere,
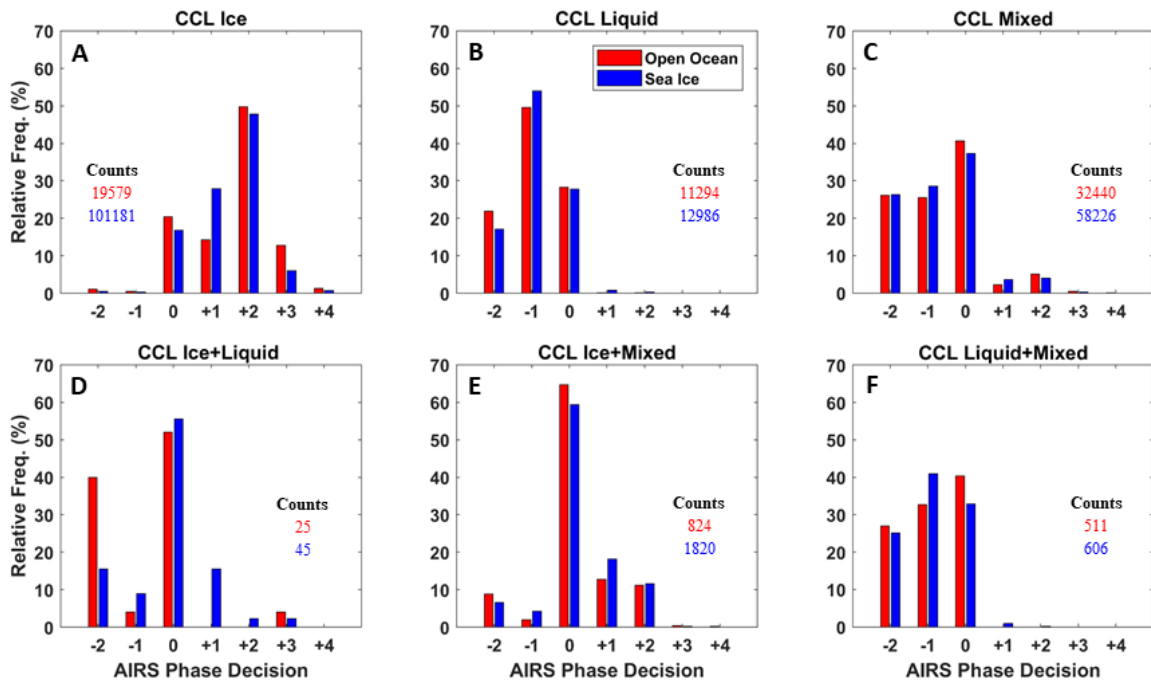
Figure 3.5. Frequencies of occurrence of AIRS phase classifications for AIRS FOVs corresponding to single-layer-overcast groups of CCL FOVs with a homogenous (A-C) or heterogenous (D-F) phase type. The counts represent the number of AIRS FOVs included in the analysis for each surface type, respectively. Normalization is with respect to these counts.

especially since liquid clouds tend to occur lower in the atmosphere.

What is more interesting is the homogenous CCL mixed-phase groups (Fig. 3.5c). Over open ocean, AIRS classifies 52% of these groups as liquid, 41% as unknown and 8% as ice-phase.

For sea ice, it is 55%, 38%, and 8% for AIRS liquid, unknown, and ice-phase, respectively. This can be contrasted against the results of JN14 where the majority of CALIPSO mixed-phase groups were classified as unknown-phase by AIRS. The tendency for AIRS to classify the homogenous mixed-phase CCL groups as liquid-phase could be related to the structure of Arctic mixed-phase clouds, as such clouds tend to have a thin liquid layer at the cloud-top (e.g. Morrison et al., 2012).

The AIRS phase classifications of heterogenous-mixed-phase CCL groups appear to differ from that of the homogenous-mixed-phase CCL groups, but it is also important to note that there are less samples in the heterogeneous-phase cases. For the heterogeneous ice+liquid and ice+mixed CCL groups (Fig. 3.5d,e), most of the AIRS phase classifications are unknown, which is similar to the results of JN14. It should be noted that the JN14 CALIPSO mixed-phase groups are like the CCL heterogeneous-mixed-phase groups. AIRS classified relatively more of the liquid+mixed CCL phase groups as liquid-phase compared to the homogenous-mixed-phase CCL groups (Fig. 3.5f), which may simply be a result of more liquid cloud being present in the AIRS FOV. The results here suggest that AIRS phase classifications could be dependent on the spatial scale of cloud phase mixing.

AIRS Phase Classification Skill Matrix			
Phase Class	CCL Ice	CCL Liquid	CCL Mixed
AIRS Ice	85.76 (94.64)	0.13 (0.17)	14.11 (5.18)
AIRS Liquid	1.2 (1.88)	32.13 (21.98)	66.65 (76.14)
AIRS Unknown	19.62 (40.1)	15.69 (8.53)	64.68 (51.37)

Table 3.1. Percentage composition of all AIRS FOVs with a given phase classification in terms of CCL phase using homogenous single-layer-overcast CCL FOV groups over open ocean. The values in parentheses are for sea ice.

Table 3.1 shows percentage composition of all AIRS FOVS classified as AIRS liquid, ice, or unknown-phase in terms of the homogenous-phase CCL groups. This represents an assessment of AIRS classification skill in the Arctic. Over open ocean, 86% of AIRS FOVs classified as ice-

phase by AIRS were classified as ice-phase by CCL, where over sea ice the ice-phase classification skill is 95%. The majority of AIRS liquid-phase classifications correspond to CCL mixed-phase over both surface types. For open ocean, the percentage of AIRS FOVs classified as liquid-phase by AIRS that are classified as mixed-phase by CCL is 67% and over sea ice the value is 76%. AIRS liquid-phase classification skill differs over the surface types, where it is 32% over open ocean and 22% over sea ice. It is possible that the ~10% difference in AIRS liquid and ice-phase classification skill over the surface types is related to differences in the surface emissivity of the surfaces for cases in which the cloud is not entirely opaque.

AIRS unknown-phase classifications are mainly composed of CCL ice-phase and CCL mixed-phase, but the relative contribution of these CCL phase groups is different over each surface type. Over sea ice, 40% of AIRS FOVs classified as AIRS unknown-phase are classified as ice-phase by CCL and 51% are classified as mixed-phase by CCL. Over open ocean, it is 19% and 65% for CCL ice-phase and mixed-phase, respectively.

Overall, mixed-phase clouds appear to contribute the most to AIRS unknown and liquid-phase classifications in the Arctic. As discussed previously, the liquid-topped structure of mixed-phase clouds could contribute to AIRS liquid-phase classifications, but if the upper region of the mixed-phase cloud is more homogenously mixed in terms of ice and liquid particles, this could lead to AIRS unknown-phase classifications.

3.3.2.2 Two-layer Systems

Two-layer-overcast CCL groups occur 15-20% of the time in the Arctic compared to all overcast CCL groups in which ≥90% CCL FOVs have the same layer number. Figure 3.6a shows the frequency of occurrence of two-layer phase combinations in which each layer are overcast CCL groups with homogenous-phase. The most common two-layer phase systems are ice-phase-over-liquid-phase and ice-phase-over-mixed-phase. Such two-layer systems typically consist of

69

ice clouds above 4 km and lower-level liquid and mixed-phase clouds, which is illustrated in Figure 3.1.
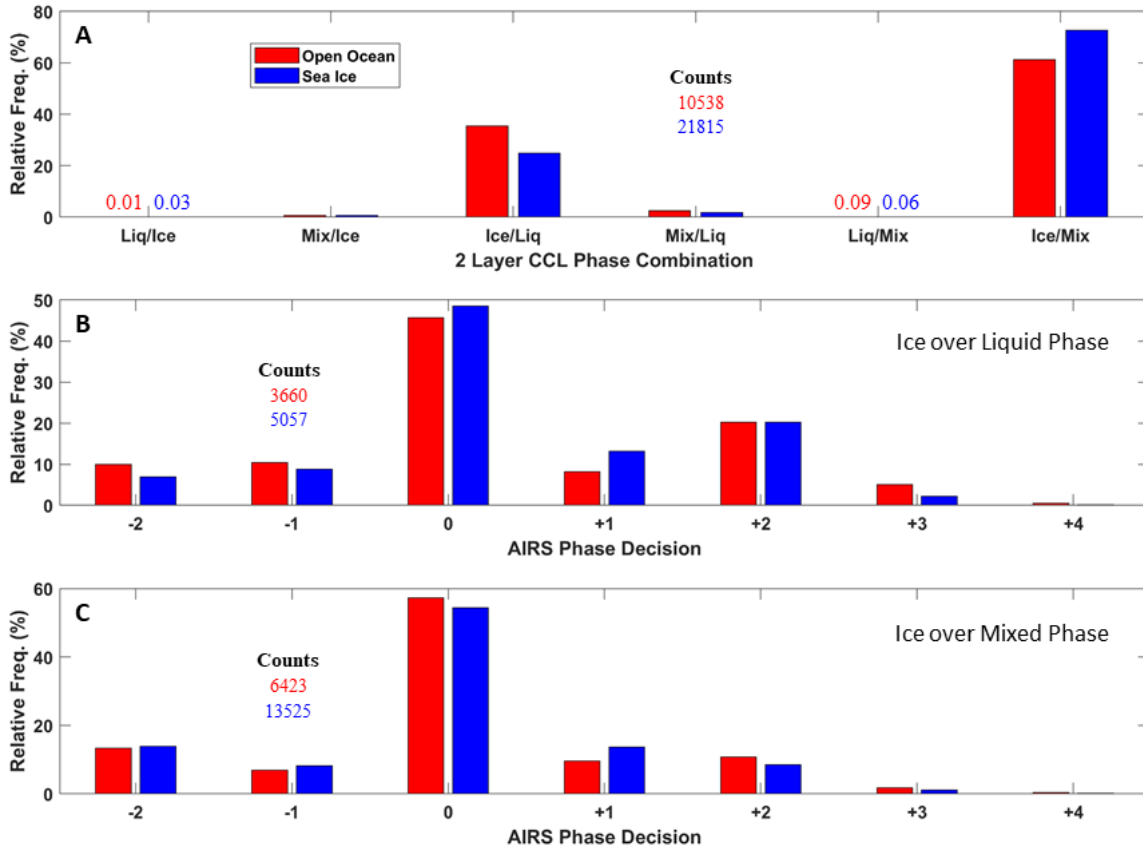
Figure 3.6. (A) Frequency of occurrence of two-layer-overcast CCL phase groups over open ocean and sea ice. The counts represent the number of CCL groups included in the analysis for each surface type, respectively. Normalization is with respect to these counts. (A) Frequency of occurrence AIRS phase decisions for two-layer-overcast CCL ice-phase-over-liquid-phase for open ocean and sea ice. The counts represent the number of AIRS FOVs included in the analysis for each surface type, respectively. (C) Same as (B) expect for CCL ice-phase-over-mixed-phase. Numerical percentages for each surface type replace bars when the bars are not visible.

Figures 3.6b and 3.6c show the relative frequency of occurrence of AIRS phase decisions for the ice-phase-over-liquid-phase and ice-phase-over-mixed-phase groups, respectively. For both groups, regardless of surface type, most AIRS classifications are unknown-phase, but a non-negligible amount of AIRS FOVs are classified as liquid and ice-phase for both two-layer groups. For the cases in which the upper layer ice cloud is optically thick in the IR, it is expected that most of those cases will be classified as ice-phase by AIRS given the high ice-phase classification skill.

When the upper layer is not completely opaque in the IR, the underlying mixed-phase or liquid-phase layer could be contributing to the AIRS liquid and unknown-phase classifications.

3.3.2.3 AIRS Phase Evaluation in the Vertical Dimension

Figure 3.7 shows the frequency of occurrence of CCL cloud phase from individual CCL cloud layers that are binned based on the overlying AIRS phase decision and surface type. The cloud layers are shown for 39 altitude bins from 0-10 km. All CCL FOVs that have successful cloud phase detections are used, including those with vertical layer numbers larger than 1. This provides another perspective for evaluating AIRS cloud phase classifications compared to the overcast CCL FOV grouping methods previously shown.
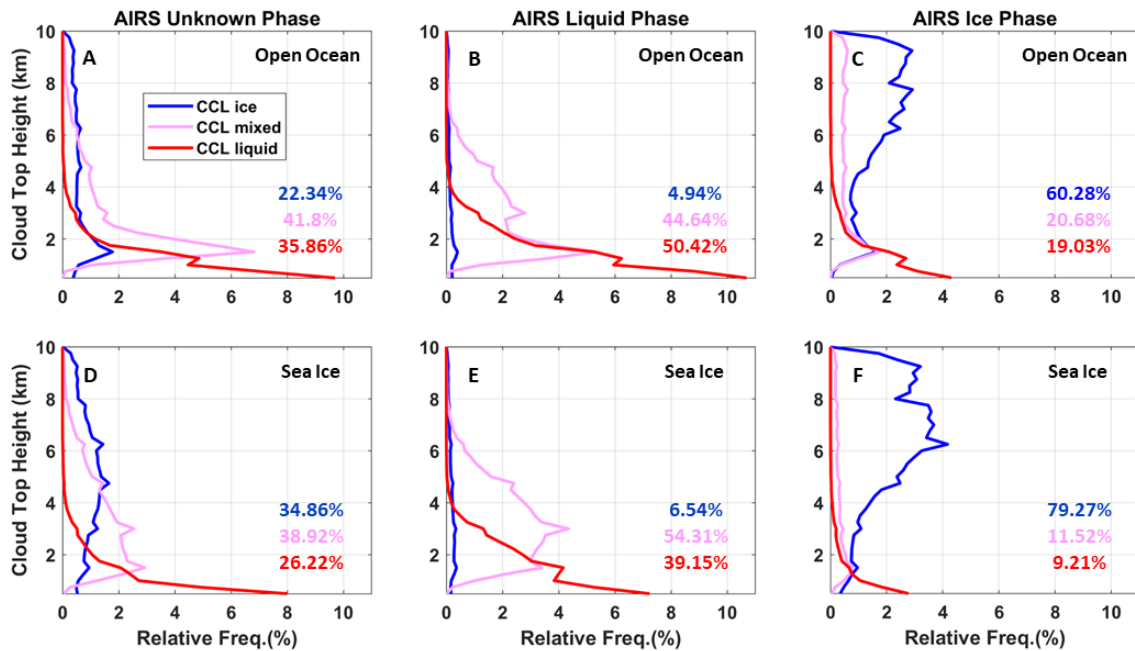
Figure 3.7. (A-C) Frequency of occurrence of individual mixed-phase, ice, or liquid CCL layers that are binned based on the overlying AIRS phase classification over open ocean and sea ice. Each individual CCL layer within a single CCL FOV is counted here separately and there are 39 altitude bins from 0-10 km. The percentages represent the vertical sums of each phase type frequency for each panel, respectively. The normalization is with respect to the total number of cloud layers detected by CCL that occur within an AIRS phase category over each surface type, respectively.

AIRS FOVs classified as ice-phase by AIRS tend to correspond to the presence of CCL ice cloud layers above 4 km (Fig. 3.7c,f), which is consistent with the high ice-phase classification skill of AIRS (Table 1). There are also CCL liquid and mixed-phase layers present ~40% of the time over open ocean, and ~20% of the time over sea ice (Fig. 3.6c,f), which are mostly excluded when selecting only overcast groups of CCL FOVs. The vertical distribution of CCL phase within AIRS FOVs classified as liquid-phase by AIRS over open ocean (Fig. 3.7b) shows very little CCL ice-phase layers (<5%) and a comparable mixture of liquid (from 0 to 4 km) and mixed-phase (from 0 to 6 km) CCL layers. A similar vertical distribution of CCL phase within AIRS FOVS classified as liquid by AIRS can also be seen over sea ice (Fig. 3.7e), but in this case mixed-phase clouds are more dominant compared to open ocean. This is consistent with AIRS liquid classifications having most contributions from CCL liquid and mixed-phase groupings, and more AIRS liquid-phase being classified as mixed-phase by CCL over sea ice (Table 3.1). For the AIRS unknown-phase category (Fig. 3.7a,d), the occurrence of CCL ice, liquid and mixed-phase cloud layers are more comparable from 0 to 10 km, with the largest contributions coming from CCL mixed-phase over both surface types, which is a feature also seen in Table 3.1. The larger rate of misclassification of CCL ice-phase groups as unknown by AIRS over sea ice (see Table 3.1) is also seen here in the vertical cloud information.

3.3.3 Climatological Perspectives of AIRS and CCL Arctic Cloud Phase Comparisons

In this section, the evaluation of AIRS cloud phase retrievals in the Arctic is extended to a climatological context in which AIRS and CCL cloud phase from the collocated AIRS-CCL dataset is compared seasonally, zonally, and by compositing by TCWV and the temperature difference between 1000-300 hPa ($\Delta T_{1000-300}$). The composite with respect to TCWV and $\Delta T_{1000-300}$ is used to examine the cloud phase classification with respect to large-scale dynamic and

thermodynamic factors, in addition to the zonal and seasonal characterization of the cloud phases as identified by the AIRS and CCL algorithms. Here, all collocated AIRS and CCL FOVs with a cloud phase assigned are used. For the TCWV and $\Delta T_{1000\text{-}300}$ composites, AIRS and CCL FOVs were matched with the nearest hourly $0.25°x0.25°$ ERA-5 grid.

3.3.3.1 Seasonal and Zonal Comparisons

Figure 3.8 shows the relative frequency of occurrence of AIRS and CCL cloud phase using all CCL cloud layers for 5° zonal bands during all four seasons (top row) and the Arctic-wide vertical frequency of occurrence of CCL cloud phase using all layers during each season (bottom row). All surface types are used here.
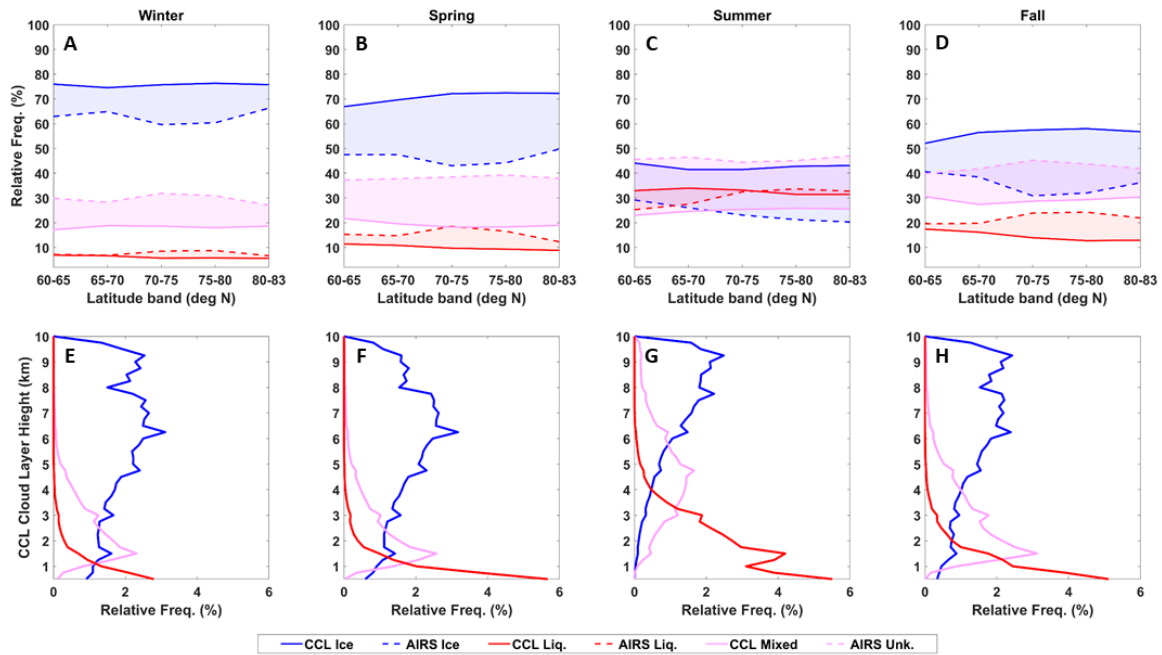
Figure 3.8. (A-D) Frequency of occurrence of CCL phase using all CCL detected cloud layers (solid lines) and AIRS cloud phase (dashed lines) for 5° latitudinal bands (except for 80-83°N) for winter, spring, summer, and fall, respectively. All surface types are included. The frequencies are relative to the total FOV count in each latitudinal band for each instrument for each season, respectively. (E-H) Frequency of occurrence of individual mixed-phase, ice, or liquid CCL layers over all surface types during winter, spring, summer, and fall, respectively. Each individual CCL layer within a single CCL FOV is counted here separately and there are 39 altitude bins from 0-10 km. The normalization is with respect to the total number of cloud layers detected by CCL during a season.

For all seasons and latitudes, the relative occurrence of liquid-phase is similar for AIRS and CCL (top row of Fig. 3.8), where the differences tend to be within 10%. Furthermore, AIRS underestimates ice-phase relative occurrence compared to CCL during all seasons, where the difference in relative occurrence between AIRS and CCL ice-phase ranges from ~10-30% depending on the latitude and season. It is important to note here that AIRS ice and liquid-phase occurrence is relative to AIRS unknown-phase while CCL ice and liquid-phase occurrence is relative to CCL mixed-phase. Given that most AIRS unknown-phase classifications correspond to CCL ice and mixed-phase groups, it is unsurprising that the liquid-phase relative occurrence agrees more between the instruments. When the AIRS and CCL cloud phase is compared seasonally and zonally using the single-layer-overcast and homogenous-phase CCL groups only (not shown), the ice-phase occurrence between the instruments agrees more than for liquid-phase, which is consistent with AIRS phase classification skill shown in Table 3.1.

Although there are differences in the magnitude of relative occurrence of cloud phase from AIRS and CCL, the relative occurrence of cloud phase from each instrument follow a similar seasonal cycle (top row of Fig. 3.8), where ice and liquid-phase peak in the winter and summer, respectively. Overall, AIRS unknown-phase classifications tend to follow the seasonal change in CCL mixed-phase, as most AIRS unknown-phase classifications correspond to CCL mixed-phase (Table 3.1). However, a significant fraction of AIRS unknown-phase classifications also corresponds to CCL ice-phase as well, and therefore the opposing seasonal cycles of CCL ice and mixed/liquid-phase can act to dampen changes in AIRS unknown-phase occurrence across seasons.

The seasonal cycle of the vertical relative frequency of occurrence of CCL phase (bottom row of Fig. 3.8) shows agreement with the zonal patterns. In winter and spring, most clouds are

ice-phase and occur throughout the atmosphere and peak at ~6 km. In the summer and fall, the overall occurrence of liquid-phase increases, mainly below 4 km. CCL mixed-phase occurrence peaks in the fall at ~2km.

3.3.3.2 Total Column Water Vapor Composite

Figure 3.9 shows the relative frequency of occurrence of AIRS cloud phase and CCL cloud phase using all CCL detected cloud layers over sea ice and open ocean for TCWV intervals spanning 1-20 kg/m^2. Over open ocean, most cloudy AIRS and CCL FOVs are associated with the TCWV range of 4-12 kg/m^2 (Fig. 3.9a,c). This can be contrasted with the sea ice scenes, where the regime shifts to 1-4 kg/m^2 (Fig. 9b,d). This is consistent with sea ice being associated with colder and drier regions and the largely reduced local evaporation.

Over both surface types, CCL liquid-phase occurrence relative to the other CCL phases has a similar magnitude and relationship with TCWV, where it increases from 5-10% to 30-35% as TCWV is increased (Fig. 3.9,b). The presence of more liquid clouds relative to the other phases at higher TCWV values is likely physical. Over open ocean, mixed-phase cloud relative occurrence is largest at 40% in the driest TCWV regimes and decreases to 30% as TCWV is increased. This relationship between CCL mixed-phase and TCWV is different over sea ice, where mixed-phase cloud relative occurrence is largest in the wettest TCWV regime. Such differences highlight the complex relationship between Arctic mixed-phase clouds and humidity. For CCL ice-phase occurrence, the relationship between TCWV and ice-phase cloud relative occurrence is similar over each surface type, where the relative occurrence of ice clouds decreases with increasing TCWV, which could be explained by more of the cloud condensate being allocated to liquid-water content.

AIRS tends to underestimate the relative occurrence of ice-phase compared to CCL in all but the wettest TCWV regime and the relative occurrence of liquid-phase is more comparable across the TCWV regimes (Fig. 3.9c,d). Over open ocean, AIRS ice-phase relative occurrence increases with TCWV, which is opposite to CCL, and is underestimated compared to CCL by ~40% in the driest TCWV regime. Over sea-ice, the relationship between AIRS ice-phase relative occurrence and TCWV is like CCL, where ice-phase relative occurrence decreases with TCWV.
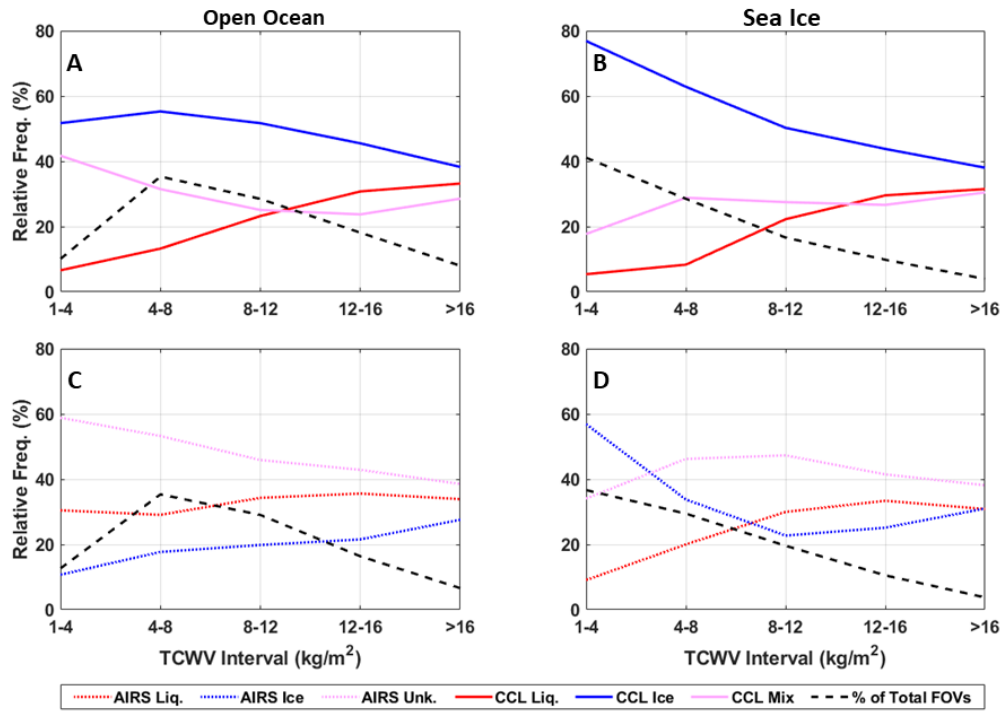
Figure 3.9. (A) Frequency of occurrence of CCL cloud phase using all CCL detected cloud layers over open ocean for intervals of TCWV. The dotted black line represents the percentage of cloudy CCL FOVs that fall within a TCWV interval. Normalization is with respect to all CCL FOVs with a cloud phase assigned in a given TCWV interval. (B) Same as (A) expect for sea ice. (C) Frequency of occurrence of AIRS cloud phase over open ocean for intervals of TCWV. The dotted black line represents the percentage of cloudy AIRS FOVs that fall within a TCWV interval. Normalization is with respect to all AIRS FOVs with a cloud phase assigned in a given TCWV interval. (D) Same as (C) expect for sea ice.

For both surface types, AIRS overestimates liquid-phase relative occurrence anywhere from 5-20% depending on the TCWV regime. However, for each surface type, just like CCL, AIRS liquid-phase increases with TCWV. Over each surface type, AIRS unknown-phase relative occurrence is largest for all TCWV regimes except for 1-4 kg/m^2 over sea ice. For open ocean, AIRS unknown

is largest in the driest TCWV regime, which coincides with the peak of CCL mixed-phase, and linearly decreases with increasing TCWV. For sea ice, AIRS unknown-phase relative occurrence remains between 35-55% for all TCWV regimes, which corresponds to CCL mixed-phase having small variations across TCWV regimes.

3.3.3.3 1000-300 hPa Temperature Difference Composite

Figure 3.10 shows the frequency of occurrence of AIRS cloud phase and CCL cloud phase using all CCL detected cloud layers over sea ice and open ocean for $\Delta T_{1000-300}$ intervals ranging from 30-65 K. Over open ocean, the $\Delta T_{1000-300}$ intervals most associated with cloudy AIRS and CCL FOVs are 50-55 K (Fig. 3.10a,c). Over sea ice, the $\Delta T_{1000-300}$ occurrence peak shifts to smaller values (Fig. 3.10b,d) which is consistent with colder surface conditions producing a more stable troposphere.

Over each surface type, CCL liquid-phase relative occurrence shows a general increasing trend from 5-10% to 10-15% with increasing $\Delta T_{1000-300}$. At higher $\Delta T_{1000-300}$, the Arctic troposphere can be more unstable and could thus favor the development of liquid cloud water. CCL mixed-phase cloud relative occurrence is largest in the smallest $\Delta T_{1000-300}$ regime (30-35 K) over open ocean and linearly decreases with increasing $\Delta T_{1000-300}$. Over sea ice, CCL mixed-phase relative occurrence varies from 15-30% and peaks between 50-55 K. CCL ice-phase relative occurrence has a distinctly different relationship with $\Delta T_{1000-300}$ over each surface type. Over open ocean, it increases from ~50% to 60% with increasing $\Delta T_{1000-300}$, and over sea ice it decreases from ~80% at the most stable $\Delta T_{1000-300}$ regimes, is minimum at 50% between 45-50 K, and then linearly increases with increasing $\Delta T_{1000-300}$.

AIRS underestimates the relative occurrence of ice-phase over open ocean by 20-40% when compared to CCL (Fig. 3.10a,c), but the relationship between ice-phase occurrence and

$\Delta T_{1000-300}$ is similar to CCL. Over sea ice, AIRS and CCL agree that ice-phase occurrence is larger than liquid-phase across the $\Delta T_{1000-300}$ regimes and both AIRS and CCL's ice-phase relative
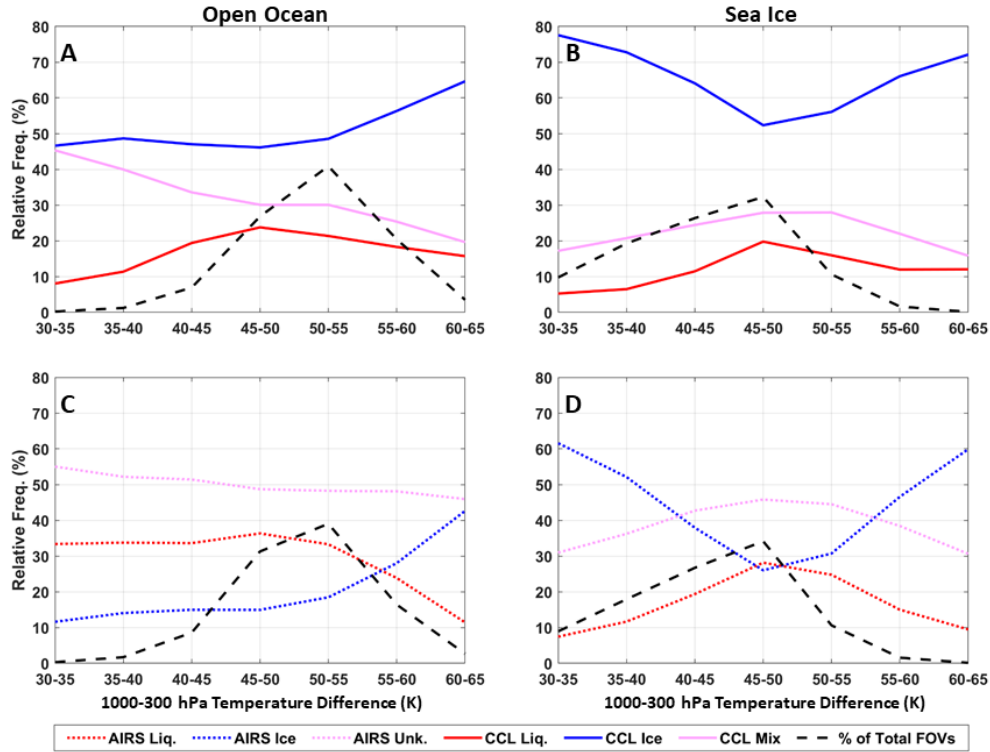
Figure 3.10. (A) Frequency of occurrence of CCL cloud phase using all CCL detected cloud layers over open ocean for intervals of the temperature difference between 1000 and 300 hPa ($\Delta T_{1000-300}$). The dotted black line represents the percentage of cloudy CCL FOVs that fall within a $\Delta T_{1000-300}$ interval. Normalization is with respect to all CCL FOVs with a cloud phase assigned in a given $\Delta T_{1000-300}$ interval. (B) Same as (A) expect for sea ice. (C) Frequency of occurrence of AIRS cloud phase over open ocean for intervals of $\Delta T_{1000-300}$. The dotted black line represents the percentage of cloudy AIRS FOVs that fall within a $\Delta T_{1000-300}$ interval. Normalization is with respect to all AIRS FOVs with a cloud phase assigned in a given $\Delta T_{1000-300}$ interval. (D) Same as (C) expect for sea ice.

occurrence have a very similar functional relationship with $\Delta T_{1000-300}$ (Fig. 3.10b,d). However, AIRS still underestimates ice-phase relative occurrence over sea ice by 10-20%. AIRS tends to overestimate the relative occurrence of liquid-phase by 10-20% over open ocean compared to CCL. Also, AIRS liquid-phase relative occurrence is largest in the smallest $\Delta T_{1000-300}$ regimes and smallest in the highest $\Delta T_{1000-300}$ regime, which is opposite to that of CCL over open ocean. Over sea ice, AIRS and CCL liquid-phase occurrence have a similar relationship with $\Delta T_{1000-300}$, but AIRS tends to overestimate liquid-phase relative occurrence by 5% to 10% compared to CCL.

AIRS unknown-phase occurrence is larger than AIRS liquid and ice-phase over all $\Delta T_{1000\text{-}300}$ regimes for open ocean and is not highly dependent on $\Delta T_{1000\text{-}300}$. Over sea ice, AIRS unknown-phase is only greater than AIRS liquid and ice-phase within the 40-55 K regimes.

The TCWV and $\Delta T_{1000\text{-}300}$ composite analyses indicate that AIRS and CCL disagree on the magnitude of relative occurrence of liquid and ice-phases in the regimes. The AIRS unknown-phase is a major contributor to such biases, especially over open ocean where CCL mixed-phase clouds are more prevalent. However, the relationship between AIRS cloud phase and TCWV and $\Delta T_{1000\text{-}300}$ regimes is similar to CCL, mainly over sea ice, and this indicates that AIRS cloud phase retrievals can be realistically used in Arctic cloud process studies. Lastly, it was determined that neither $\Delta T_{1000\text{-}300}$ nor TCWV regime significantly impacted AIRS phase classification skill.

3.4. MODIS-AIRS-CCL Case Study

A case study was conducted using daytime only collocated Arctic MODIS-AIRS-CCL FOVs for July 2009 in order to understand (1) the relationship between MODIS cloud amount and phase and AIRS Arctic cloud phase occurrence statistics and (2) the agreement between MODIS and CCL cloud phase classifications. MODIS cloud fraction (CF) within an AIRS FOV is defined as the ratio of MODIS pixels within an AIRS FOV that are flagged as probably or confident cloudy with respect to the total number of MODIS pixels in the AIRS FOV. Only AIRS FOVs with >95% of MODIS pixels having a cloud mask decision are included.

Figure 3.11 (top row) shows the occurrence frequency of AIRS cloud phase over open and sea ice together using all collocated MODIS-AIRS-CCL AIRS FOVs (black bars) and for those in which there is only greater than 90% MODIS CF in the AIRS FOVs (gray bars). This is shown for collocation with single-layer-overcast and homogeneous CCL ice-phase groups (left column), CCL liquid-phase groups (middle column) and for CCL mixed-phase groups (right column). For

each of the CCL phase groups (Fig. 3.11a-3.11c), the frequency of occurrence of AIRS phase

decisions is similar to what is observed for the entire four-year period. This indicates that the AIRS
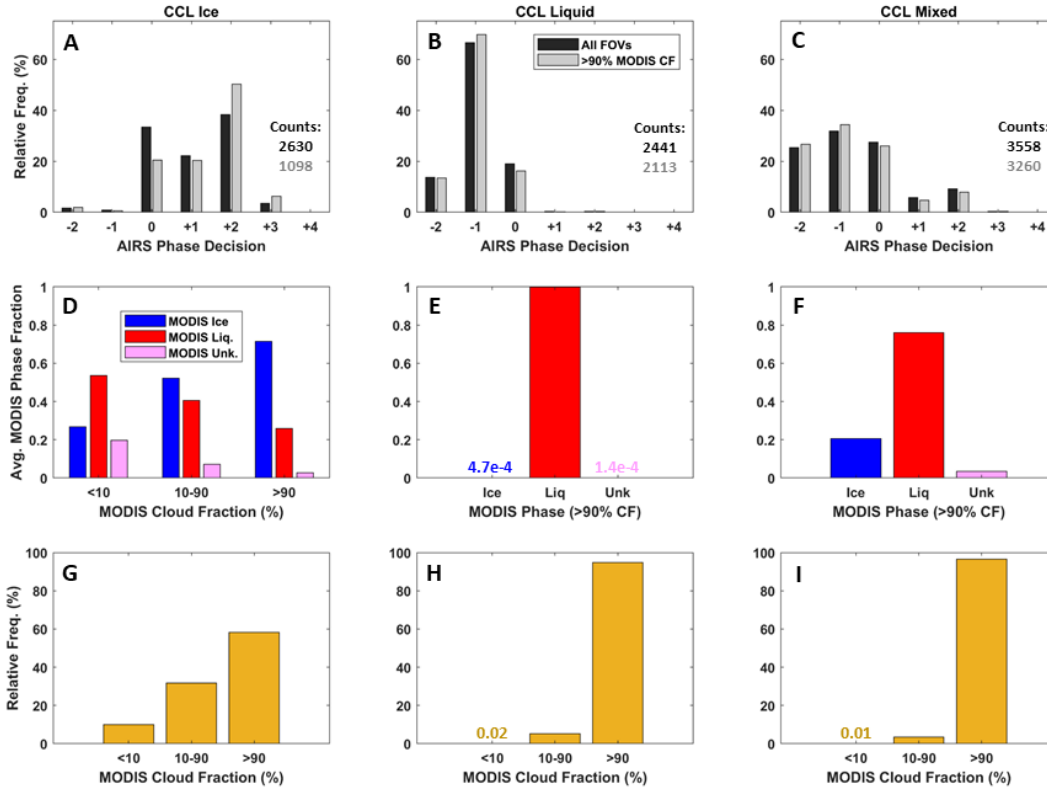
Figure 3.11. All panels are for July 2009 over open ocean and sea ice and each column is for AIRS FOVs that contain single-layer-overcast homogenous ice, liquid or mixed-phase CCL FOV groups, respectively: (A-C) Frequency of occurrence of AIRS phase decisions for all AIRS FOVs collocated with CCL and MODIS and for which the MODIS cloud fraction (CF) within the AIRS FOV is >90%. The counts represent the number of AIRS FOVs included for the "All FOVs" and ">90% MODIS CF" categories. The normalization is with respect to these counts. (D) Average MODIS cloud phase fraction (the number the MODIS pixels of a given phase divided by all MODIS pixels that are assigned a phase in the AIRS FOV and then averaged across all respective AIRS FOVs) for 3 intervals of MODIS CF. (E-F) Same as D except for >90% MODIS CF only. (G-I) Frequency of occurrence of MODIS CF in three intervals. The normalization here is with respect to the number of all AIRS FOVs included in the analysis (count numbers in black, top row)

cloud phase classification skill determined in Section 3.3 is robust to sampling differences. Figure

3.11 (middle row) shows the average MODIS cloud phase fraction (CPF) from AIRS FOVs that

are collocated with each CCL cloud phase group (Fig. 3.11d-3.11f). Here, MODIS CPF is defined

as the ratio of MODIS pixels of a given phase relative to all MODIS pixels with a phase assigned

in the AIRS FOV. This shown for three regimes of MODIS CF (CF>10%, 10%<CF<90%, and

CF>90%) in Figure 3.11d. For Figures 3.11e and 3.11f, MODIS CF is greater than 90% only. Figure 3.11 (bottom row) shows the frequency of occurrence of MODIS CF within three CF regimes. This is shown for collocation with each of the three CCL cloud phase groups (Fig. 3.11g-3.11i).

MODIS CF occurrence in Figures 3.11h and 3.11i indicates that most AIRS FOVs containing the CCL liquid and mixed-phase groups have greater than 90% cloud cover. Cloud amount in the Arctic reaches its peak in July and thus it is reasonable to observe a high occurrence of horizontal cloud coverage within these AIRS FOVs. For the AIRS FOVs with CCL liquid-phase groups, the average MODIS liquid CPF is ~0.99 (Fig. 3.11e). Marchant et al. (2016) shows that when evaluated with CALIPSO, MODIS correctly classifies liquid cloud scenes at a higher rate than ice cloud scenes, which could help explain the liquid-phase agreement between MODIS and CCL seen in this study. For the AIRS FOVs with CCL mixed-phase groups, average MODIS liquid and ice CPF is ~0.75 and ~0.25, respectively (Fig. 3.11f). This indicates that CCL mixed-phase clouds tend to correspond to MODIS liquid-phase classifications just as they corresponds to AIRS liquid-phase. For the AIRS FOVs with CCL ice groups, greater than 90% MODIS CF occurs about 60% of the time (Fig. 3.11g), and for such cases the average MODIS ice and liquid CPF is ~0.7 and ~0.3, respectively.

When AIRS FOVs with less than 90% MODIS CF are selected in the AIRS cloud phase evaluation for the CCL liquid and ice-phase groups, the amount of unknown-phase classifications increases. This corroborates the results of Kahn et al. (2011) and Guillaume et al. (2019), who presented a similar result for global AIRS observations. However, it should be noted that when 10-90% MODIS CF is included in the AIRS phase evaluations for the CCL ice-phase groups, the average ice and liquid MODIS CPF becomes comparable, and this effect can also be responsible

for increasing AIRS unknown-phase classifications, as was shown in Kahn et al. (2011). Overall, MODIS cloud phase classification for ice and liquid scenes was consistent with CCL, which provides more confidence of the use of CCL for AIRS cloud phase evaluations during the four-year period.

3.5. Conclusion

In this study, AIRS Arctic cloud phase classification was evaluated against combined CloudSat-CALIPSO (CCL) observations over a four-year period. Our approach for this AIRS phase evaluation was distinctly different compared to the global evaluation performed by JN14, especially in our use of CCL mixed-phase classification. Overall, AIRS ice-phase classification skill in the Arctic for single-layer clouds is >85% depending on the surface type, which is much higher than the classification skill for liquid-phase. However, AIRS tends to classify more liquid-phase clouds as liquid-phase in the Arctic compared to what was reported for the entire globe in JN14. It is possible that dry atmospheres lead to less ambiguous AIRS liquid phase classification, and this warrants future investigation. Mixed-phase clouds correspond to AIRS unknown and liquid-phases. AIRS phase classification changes with horizontal scale of cloud phase mixing, thus the morphology of mixed-phase cloud systems could influence AIRS phase decisions. The results of the two-layer AIRS phase evaluation indicate that, in some cases, the upper layer cloud is transparent enough in the IR for the lower cloud layer's phase signal to influence AIRS phase decisions. The two-layer systems produce mostly unknown AIRS phase classifications, and such systems should be considered when improving the AIRS cloud phase algorithm.

When using all collocated AIRS and CCL FOVS, AIRS ice-phase occurrence relative to the other AIRS phases was less than that for CCL ice-phase relative occurrence across latitudes, seasons, and TCWV and $\Delta T_{1000-300}$ regimes over both sea ice and open ocean. However, the liquid-

phase relative occurrence had more agreement. This result likely is due to AIRS unknown-phase classifications corresponding to CCL ice-phase and mixed-phase. The seasonal cycle, and in some cases, the dependence of cloud phase relative occurrence on TCWV and $\Delta T_{1000-300}$ regime, was similar between CCL and AIRS. This indicates that AIRS cloud phase data can capture the connections between the physical properties and processes in the Arctic atmosphere and cloud phase. Moreover, the accurate seasonal cycle of AIRS liquid and ice cloud phase indicates that AIRS could provide accurate occurrence anomalies on inter-seasonal to inter-annual scales.

The MODIS case study indicates that heterogenous cloud cover and cloud phase distributions in the AIRS FOV correspond to increased unknown-phase classifications by AIRS, which verifies the findings of previous studies. Because MODIS cloud phase throughout the AIRS FOVs tended to correspond to cloud phase detected by CCL, and the case-study-based AIRS phase decision statistics were similar to that of the entire four-year period, the case study provides more confidence in the use of the CCL narrow track for AIRS phase evaluations.

Given that 42% of AIRS FOVs over the Arctic Ocean were classified as unknown-phase by AIRS, it is pertinent to improve the algorithm. The results of this study both illuminate factors to consider for algorithm improvement and factors of secondary importance. For example, both TCWV and $\Delta T_{1000-300}$ did not significantly impact AIRS phase classification skill. However, surface type did correspond to ~10% differences in AIRS phase classification skill for ice and liquid-phase. Given that window channels are used in the AIRS phase algorithm, it is possible that differences in the surface emissivity of open ocean and sea ice may play a role in phase misclassifications for thin clouds. Channels that are less useful in moist lower latitudes could be used to improve cloud phase classifications in the dry Arctic. An information content analysis

could shed light onto how cloud phase signatures influence AIRS channels in variable TCWV regimes.

Mixed-phase cloud identification using the IR continues to be a challenge. Over the Arctic, AIRS frequently classifies mixed-phase clouds as either liquid or unknown and, according to the case study, MODIS frequently classifies them as liquid-phase. However, because CCL can only identify the presence of liquid and ice within a single cloud layer, we could not further investigate how the influence of mixed-phase cloud vertical structure relates to AIRS or MODIS cloud phase decisions. This could be addressed by collocating ground-based high-spatial-resolution lidar measurements of Arctic mixed-phase clouds with AIRS and MODIS observations or generating synthetic radiances for cloud phase classification from large eddy simulations that capture realistic mixed-phase cloud processes.

Acknowledgments

References

Ackerman, S. A., Strabala, K. I., Menzel, P., Frey, R. A., Moeller, C. C., Gumley, L. E. (1998). Discriminating clear sky from clouds with MODIS. *Journal of Geophysical Research,* 103(D24), 32141– 32157. https://doi.org/10.1029/1998JD200032

Aumann, H. H., Chahine, M. T., Gautier, C., Goldberg, M. D., Kalnay, E., Mcmillin, L. M., et al. (2003). AIRS/AMSU/HSB on the aquamission: Design, science objectives, data products, and processing systems. *IEEE Transactions on Geoscience and Remote Sensing*, **41(2)**, 253–264. https://doi.org/10.1109/tgrs.2002.808356

Baum, B. A., Menzel, W. P., Frey, R. A., Tobin, D. C., Holz, R. E., Ackerman, S. A., et al. (2012). MODIS cloud-top property refinements for Collection 6. *Journal of Applied Meteorology and Climatology*, **51(6)**, 1145-1163. doi:10.1175/jamc-d-11-0203.1

Baum, B. A., Soulen, P. F., Strabala, K. I., King, M. D., Ackerman, S. A., Menzel W. P., et al. (2000). Remote sensing of cloud properties using MODIS Airborne Simulator imagery during SUCCESS. II. Cloud thermodynamic phase. *Journal of Geophysical Research*, 105, 11,781-11,792. https://doi.org/10.1029/1999JD901089

Boisvert, L. N., & Stroeve, J. C. (2015). The Arctic is becoming warmer and wetter as revealed by the Atmospheric Infrared Sounder. *Geophysical Research Letters*, 42(11), 4439-4446. https://doi.org/10.1002/2015gl063775

Cavalieri, D. J., & Parkinson, C. L. (2012). Arctic sea ice variability and trends, 1979-2010. *The Cryosphere*, **6**, 881-889. https://doi.org/10.5194/tc-6-881-2012

Cesana, G., Kay, J. E., Chepfer, H., English, J. M., & de Boer, G. (2012). Ubiquitous low-level liquid-containing Arctic clouds: New observations and climate model constraints from CALIPSO-GOCCP. *Geophysical Research Letters*, **39**, 6, doi:10.1029/2012gl053385

CHAHINE, M. T., PAGANO, T. S., AUMANN, H. H., ATLAS, R., BARNET, C., BLAISDELL, J., et al. (2006). AIRS, *Bulletin of the American Meteorological Society*, *87*(7), 911-926. https://doi.org/10.1175/BAMS-87-7-911

Cho, H. M., Nasiri, S. L., & Yang, P. (2009). Application of CALIOP measurements to the evaluation of cloud phase derived from MODIS infrared channels. *Journal of Applied Meteorology and Climatology*, 48(10), 2169-2180. doi:10.1175/2009jamc2238.1

Fetzer, E. J. (2012): A multi-sensor water vapor climate data record using cloud classification. NASA MEaSUREs Project. [Available online at http://disc.sci.gsfc.nasa.gov/ daac-bin/DataHoldingsMEASURES.pl?PROGRAM_List5 EricFetzer.]

Goloub, P., Herman, M., Chepfer, H., Riedi, J., Brogniez, G., Couvert, P., et al. (2000). Cloud thermodynamical phase classification from the POLDER spaceborne instrument. *Journal of Geophysical Research*, **105**, 14 747–14 759. https://doi.org/10.1029/1999JD901183

Guillaume, A., Kahn, B. H., Fetzer, E. J., Yue, Q., Manipon, G. J., Wilson, B. D., et al. (2019). Footprint-scale cloud type mixtures and their impacts on Atmospheric Infrared Sounder cloud property retrievals, *Atmospheric Measurement Techinques*, **12**, 4361–4377. https://doi.org/10.5194/amt-12-4361-2019

Hersbach, H., de Rosnay, P., Bell, B., Schepers, D., Simmons, A., Soci, C. (2018). Operational global reanalysis: progress, future directions and synergies with NWP, *ECMWF ERA Report Series* 27.

Hu, Y., Winker, D., Vaughan, M., Lin, B., Omar, A., Trepte, C. et al. (2009). CALIPSO/CALIOP Cloud Phase Discrimination Algorithm. *Journal of Atmospheric and Oceanic Technology,* **26**, 2293–2309. https://doi.org/10.1175/2009JTECHA1280.1

Intrieri, J. M., Fairall, C. W., Shupe, M. D., Persson, P. O. G., Andreas, E. L., Guest, P. S., et al. (2002). An annual cycle of Arctic surface cloud forcing at SHEBA. *Journal of Geophysical Research: Oceans*, 107(C10), **14**. doi:10.1029/2000jc000439

Jin, H. C., & Nasiri, S. L. (2014). Evaluation of AIRS cloud-thermodynamic-phase determination with CALIPSO. *Journal of Applied Meteorology and Climatology*, **53(4)**, 1012-1027. doi:10.1175/jamc-d-13-0137.1

Kahn, B. H., Chahine, M. T., Stephens, G. L., Mace, G. G., Marchand, R. T., Wang, Z., et al (2008). Cloud type comparisons of AIRS, CloudSat, and CALIPSO cloud height and amount. *Atmospheric Chemistry and Physics*, **8**, 1231-1248. https://doi.org/10.5194/acp-8-1231-2008

Kahn, B. H., Irion, F. W., Dang, V. T., Manning, E. M., Nasiri, S. L., Naud, C. M. (2014) The Atmospheric Infrared Sounder version 6 cloud products, *Atmospheric Chemistry and Physics*, 14, 399–426, https://doi.org/10.5194/acp-14-399-2014, 2014.

Kahn, B. H., Nasiri, S. L., Schreier, M. M., & Baum, B. A. (2011). Impacts of sub-pixel cloud heterogeneity on infrared thermodynamic phase assessment. *Journal of Geophysical Research,* **116**, D20201. doi:10.1029/2011JD015774

Kay, J. E., & L'Ecuyer T. (2013). Observational constraints on Arctic Ocean clouds and radiative fluxes during the early 21st century. *Journal of Geophysical Research: Atmospheres*, **118**, 7219–7236. doi:10.1002/jgrd.50489

Key, J., & Intrieri, J. (2000). Cloud particle phase determination with the AVHRR. *Journal of Applied Metoerology*, **39**, 1797–1805. https://doi.org/10.1175/1520-0450-39.10.1797

Marchand, R., Mace G. G., Ackerman, T., & Stephens, G. (2008). Hydrometeor detection using CloudSat—An Earth-orbiting 94-GHz cloud radar. *Journal of Atmospheric and Oceanic Technology*, **25(4)**, 519–533. doi: 10.1175/2007JTECHA1006.1

Marchant, B., Platnick, S., Meyer, K., Arnold, G. T., & Riedi, J. (2016). MODIS Collection 6 shortwave-derived cloud phase classification algorithm and comparisons with CALIOP. *Atmospheric Measurement Techniques*, **9**, 1587-1599. doi.org/10.5194/amt-9-1587-2016

Morrison, H., de Boer, G., Feingold, G., Harrington J., Shupe, M. D., & Sulia, K. (2012). Resilience of persistent Arctic mixed-phase clouds. *Nature Geoscience*, **5,** 11–17, doi:10.1038/ngeo1332

Nasiri, S. L., & Kahn, B. H. (2008). Limitations of bispectral infrared cloud phase determination and potential for improvement. *Journal of Applied Meteorology and Climatology*, **47(11)**, 2895-2910. doi:10.1175/2008jamc1879.1

Peterson, C. A., Chen, X., Yue, Q., & Huang, X. (2019). The spectral dimension of Arctic outgoing longwave radiation and greenhouse efficiency trends from 2003 to 2016. *Journal of Geophysical Research: Atmospheres*,**124**, 8467–8480. https://doi.org/10.1029/2019JD030428

Platnick, S., Kerry, K, G., King, M. D., Wind, G., Amarasingahe, N., Marchant, B. (2017). The MODIS Cloud Optical and Microphysical Products: Collection 6 Updates and Examples from Terra and Aqua. *IEEE Transactions on Geoscience and Remote Sensing*, **55(1)**, 502-525. doi: 10.1109/TGRS.2016.2610522

Sassen, K., Wang, Z., & Liu, D. (2008). Global distribution of cirrus clouds from CloudSat/Cloud-Aerosol Lidar and Infrared Pathfinder Satellite Observations (CALIPSO) measurements. *Journal of Geophysical Research*, **113**, D00A12. doi:10.1029/2008JD009972

Schreier, M.M., Kahn, B.H., Eldering, A., Elliott, D. A., Fishbein, E., Irion, F.W., et al. (2010). Radiance Comparisons of MODIS and AIRS Using Spatial Response Information. *Journal of Atmospheric and Oceanic Technology,* **27**, 1331–1342. https://doi.org/10.1175/2010JTECHA1424.1

Shupe, M. D. (2011). Clouds at Arctic atmospheric observatories. Part ii: Thermodynamic phase characteristics. *Journal of Applied Meteorology and Climatology*, **50(3)**, 645-661. doi:10.1175/2010jamc2468.1

Shupe, M. D., & Intrieri, J. M. (2004). Cloud radiative forcing of the Arctic surface: The influence of cloud properties, surface albedo, and solar zenith angle. *Journal of Climate*, **17(3)**, 616-628. doi:10.1175/1520-0442(2004)017<0616:crfota>2.0.co;2

Riedi, J., Platnick, S., Baum, B. A., Thieuleux, F., Oudard, C., Parol, F., et al. (2010). Cloud thermodynamic phase inferred from merged POLDER and MODIS data. *Atmospheric Chemistry and Physics*, **10**, 11 851–11 865. https://doi.org/10.5194/acp-10-11851-2010

Tanelli, S., Durden, S. L., Im, E., Pak, K. S., Reinke, D. G., Partain, P., et al. (2008). CloudSat's Cloud Profiling Radar After Two Years in Orbit: Performance, Calibration, and Processing, *IEEE Transactions on Geoscience and Remote Sensing,* **46**, 3560-3573. doi:10.1109/TGRS.2008.2002030

Thompson, D. R., Kahn, B. H., Green, R. O., Chien, S. A., Middleton, E. M., & Tran, D. Q. (2015). Global spectroscopic survey of cloud thermodynamic phase at high spatial resolution, 2005–2015, *Atmospheric Measurement Techniques*, **11**, 1019–1030. https://doi.org/10.5194/amt-11-1019-2018

Wang, T., Fetzer, E. J., Wong, S., Kahn, B. H., & Yue Q. (2016). Validation of MODIS cloud mask and multilayer flag using CloudSat-CALIPSO cloud profiles and a cross-reference of their cloud classifications. *Journal of Geophysical Research: Atmospheres*, **121(11)**, 620–11,635. doi:10.1002/2016JD025239

Wang, Z., Vane D., Stephens, G., & Reinke, D., (2013). CloudSat Project: Level 2 Combined Radar and Lidar Cloud Scenario Classification Product Process Description and Interface Control Document, 61 pp., California Institute of Technology, Jet Propulsion Laboratory.

Yue, Q., Kahn, B. H., Fetzer, E. J., & Teixeira, J. (2011). Relationship between marine boundary layer clouds and lower tropospheric stability observed by AIRS, CloudSat and CALIOP. *Journal of Geophysical Research*, **116**, D18212. doi:10.1029/2011JD016136

Chapter 4 Synergistic use of Far- and Mid-Infrared Spectral Radiances for Satellite-based Detection of Polar Ice Clouds over Ocean

The material in this chapter was published in

Peterson, A, C., Huang, X., Chen, X., Yang, P. (2022) Synergistic use of Far- and Mid-Infrared Spectral Radiances for Satellite-based Detection of Polar Ice Clouds over Ocean. *Journal of Geophysical Research: Atmosphere.* In press.

4.1. Introduction

Clouds play an important role in the energy budget and, hence, climate of the polar regions. On average, clouds tend to warm the surfaces of both polar regions through infrared (IR) emission (Intrieri et al., 2002; Scott et al., 2017). The thermodynamic phase of a cloud, or whether it is composed of liquid droplets, ice particles, or both (mixed phase), influences the radiative effects. With the same cloud water content, liquid clouds tend to be optically thicker than ice clouds, which can result in a stronger surface warming by liquid clouds than by ice clouds in polar regions (Shupe & Intrieri, 2004; Scott et al., 2017; Di Natale et al., 2020; Lubin & Vogelmann, 2006; Garrett & Zhao, 2006). Mixed phase clouds, which are common over the Arctic and Southern Oceans (Shupe, 2011; Korolev et al., 2017; Lawson & Gettelman, 2014), are produced and maintained by complex microphysical and meteorological processes that interconvert liquid droplets and ice particles and are not well characterized for the vast and remote polar regions (e.g., Morrison et al., 2012; Listowski & Lachlan-Cope, 2017). Polar mixed phase clouds are generally stratiform with a super-liquid layer of liquid water at the cloud top (de Boer et al., 2011). Based on Arctic ground

89

observations of clouds at Barrow and Eureka sites, ice-phase cloud occurs annually at a frequency of 60-70% while liquid-phase cloud occurrence frequency can be as high as 56% (Shupe, 2011). Using combined CALIPSO and CloudSat observations for grid boxes of 2° in latitude and 5° in longitude, Listowski et al. (2019) found that Antarctic ice-only cloud occurrence frequency can be up to 70% relative to all cloud observations. The occurrence frequency of super-cooled-liquid-containing clouds relative to all cloud observations can be as high as 85% over the Southern Ocean. Overall, a lack of understanding of cloud-phase-related processes leads to biases in simulations of radiative fluxes over the Arctic (Cesana et al., 2012; Kay et al., 2016) and Southern Oceans (Vergara-Temprado et al., 2018; Listowski & Lachlan-Cope, 2017).

Satellite observations are needed to estimate the spatial distribution and variability of clouds across the vast polar regions, and cloud phase is a key property. While active remote sensing techniques such as radar and lidar can be considered as benchmark tools for cloud phase detection, such measurements are only available along narrow ground tracks (e.g., ~1.5 km track width for CloudSat). Passive remote-sensing measurements such as those from AIRS and MODIS have much wider swaths, and thus, larger spatial coverages, than active remote-sensing measurements. In the polar regions, there is a limited period of solar illumination and large solar zenith angles even at solar noon. Thus, passive IR measurements are generally more useful than reflected shortwave measurements in polar regions. The mid-IR window (~800-1250 cm^{-1}) is conventionally used for cloud phase retrievals due to weak greenhouse gas absorption and the differences in the spectral variations of ice and liquid absorption across this spectral region. These differences in absorption variations, normally formulated as brightness temperature differences (BTDs) between two spectral channels in the mid-IR, can be used to detect the presence of cloud ice or liquid from space. This has been widely known as the "bi-spectral" method (e.g., Ackerman

et al., 1990; Baum et al., 2000; Strabala et al., 1994). Both the MODIS Collection 6 (Baum et al., 2012) and AIRS (Kahn et al., 2014) cloud phase algorithms utilize such mid-IR BTDs to classify clouds as ice, liquid, or uncertain phase.

The mid-IR has notable limitations when used to determine cloud phase in polar regions. A fundamental limitation is related to cloud-surface thermal contrast, i.e., the difference between the cloud top temperature (CTT) and the surface skin temperature. In polar regions, especially in winter, it is not uncommon for cloud layers to be as warm as or warmer than the surface. This can lead to clouds being indistinguishable from nearby clear-sky pixels. Moreover, if the cloud becomes increasingly opaque, it can become more difficult to use mid-IR BTDs for cloud phase determination, and the mid-IR BTDs approach 0 K as the cloud optical depth approaches infinity (if only cloud absorption and emission are considered). Another major limitation is that the mid-IR cannot determine if a cloud contains both liquid and ice particles (Baum et al., 2000; Cho et al., 2009). These problems contribute to a misclassification of 70-80% of liquid-containing clouds in the Arctic by the AIRS algorithm compared to combined CloudSat-CALIPSO observations (Peterson et al., 2020).

In the present study, we aim to demonstrate that mid-IR polar cloud phase determination can be supplemented, or even improved, by introducing far-infrared (far-IR; $<\sim 600$ cm^{-1}) spectral radiance observations. The far-IR makes up over 60% of outgoing IR radiation in polar regions, and due to the cold and dry conditions, numerous semi-transparent water vapor micro-windows between 400 and 600 cm^{-1} become available for cloud phase detection. In this study, we refer to the entire 400-600 cm^{-1} band as the dirty window region, a term introduced in Yang et al. (2003). The far-IR has been historically underutilized for spaceborne remote sensing due to technological limitations. However, two upcoming missions will measure the far-IR radiances, namely the Polar

Radiant Energy in the Far Infrared Experiment (PREFIRE) (L'Ecuyer et al., 2021) and the Far-infrared-Outgoing-Radiation Understanding and Monitoring (FORUM) missions (Palchetti et al., 2020). The planned spectral range for the sensors used in these missions is 5-54 μm for PREFIRE and 100-1600 cm^{-1} for FORUM, respectively.

Recent studies have investigated the use of high spectral resolution far-IR radiances for cloud phase classification (i.e., Maestri et al 2019a,b; Sgheri et al., 2021; Cossich et al., 2021) based on observed downwelling radiances and synthetic satellite observations. These studies utilize numerous spectral channels across the far-IR and mid-IR for the radiance inputs to a principal component analysis-based machine learning algorithm for cloud identification. Meanwhile, it may be possible to use a simple and physically based two-channel bi-spectral method for far-IR cloud phase determination because, like the mid-IR, ice and water absorption vary across the far-IR spectrum. The spectral variation of ice cloud scattering also varies across the far-IR and can be larger in the far-IR compared to the mid-IR, which can potentially provide additional information to help discriminate different cloud phases using a bi-spectral approach. Furthermore, it is possible that a far-IR BTD cloud phase algorithm can supplement or improve the conventional mid-IR BTD approach, as multiple studies have indicated that the far-IR and mid-IR can be used synergistically for cloud phase determination (e.g., Cossich et al., 2021; Turner, 2005; Rathke et al., 2002; Rowe et al., 2019). It has also been shown that the prominent far-IR scattering can be used synergistically with the mid-IR for ice cloud property retrievals (Merrelli & Turner, 2013; Libois & Blanchet, 2017; Saito et al., 2020). All the above facts and studies motivated us to further understand and exploit the synergy of the far-IR and mid-IR for polar ice cloud detection with a BTD algorithm.

This study explores the use of spaceborne far-IR radiances to improve mid-IR based ice cloud detection in the polar regions using a simple bi-spectral approach. Section 4.2 describes the reanalysis data and radiative transfer simulations used to generate synthetic spectra. Using such synthetic outgoing spectra at the top of the atmosphere (TOA), section 4.3 describes the theoretical basis for the far-IR ice phase determination and presents a far-IR BTD test for such determination. Section 4.4 provides a comparison between the far-IR and mid-IR ice phase determination skills and their relationship with ice cloud properties. A summary and conclusions are given in Section 4.5.

4.2. Reanalysis Data and Radiative Transfer Modeling

4.2.1 ERA5 Reanalysis Data

ECMWF ERA5 reanalysis fields (Hersbach et al., 2020) are used as inputs to MODerate Resolution Atmospheric TRANsmission Version 5 (MODTRAN5; Berk at al., 2005), a widely used radiative transfer model in optical remote sensing studies, to generate synthetic spectral radiances for this study. Data over both polar regions (60°N-90°N and 60°S-90°S) in January and July 2005 are used. The months are chosen to represent the contrasting physical features of winter and summer seasons. ERA5 data have a 0.25°x0.25° horizontal resolution and hourly temporal resolution. Hourly vertical profiles in ERA5 are provided at 37 fixed pressure levels from 1000 hPa to 1 hPa. The ERA5 surface pressure (Ps) is also used as input MODTRAN5 as well. The altitudes of these pressure levels are calculated using the hydrostatic approximation. A similar synthetic spectral approach has been used in previous studies of downward spectral radiance retrievals such as Rowe et al. (2019) and Rowe et al. (2016).

Profiles of atmospheric temperature, specific humidity, specific cloud liquid water content, and specific cloud ice water content, as well as surface skin temperature are used as input to the MODTRAN5 radiance calculations. In this study we only use "single-phase" clouds profiles (i.e., liquid- or ice-only) based on thresholds of ice cloud water path (IWP) and liquid cloud water path (LWP). If a cloud profile has IWP > 1 g/m^2 and LWP < 1 g/m^2, it is treated as an ice-only cloud profile. If a cloud profile has LWP > 1 g/m^2 and IWP < 1 g/m^2, it is treated as a liquid-only cloud profile. Based on ERA5 3-hourly IWP and LWP over the polar regions for the entire year of 2005, 90.9% of IWP values are greater than 1 g/m^2. For the LWP, 82.3% of the values are greater than 1 g/m^2. For the finalized set of cloud profiles (see details below) used in this study, the median LWP for the liquid-only clouds is 70.6 g/m^2 while the median IWP for the ice-only clouds is 58.1 g/m^2.

A profile that does not qualify as a liquid- or ice-only cloud profile is not considered for this study, which excludes mixed phase clouds. Once a profile is selected, it only has one single phase and, for any vertical layer with cloud water content, the cloud coverage is assumed to be 100% over the grid box. Cloud top pressure (CTP) is defined as the first pressure level from the TOA down at which the cloud water mixing ratio exceeds 1×10^{-3} g/kg.

A total of 4000 ice-only and 4000 liquid-only ERA5 profiles were selected based on the single-phase criteria described above. Land profiles are excluded and the ocean spectral surface emissivity from Huang et al. (2016) was used for all simulations. Note that extending this study over land would require considering land surface emissivity. The selected profiles only lie over the Arctic and Southern Oceans and include cases above sea ice and snow. However, using the bare ice emissivity from Huang et al. (2016) for radiance simulations did not significantly impact the far-IR and mid-IR BTDs established here (not shown).

For input into MODTRAN5, the ERA5 specific cloud water content profiles are first converted to cloud water concentration profiles. If the cloud water concentration is greater than $1x10^{-5}$ g/m^3 at a given ERA5 model level, the concentration value is directly used in MODTRAN5, otherwise that level is assumed to be cloud free. The same set of fixed pressure levels from ERA5 is directly used in MODTRAN. Based on whether a given ERA5 cloud water concentration value exceeds the $1x10^{-5}$ g/m^3 threshold, there can be a single cloud consisting of multiple consecutive levels in the MODTRAN5, a cloud consisting of only a single layer in the MODTRAN5, or multiple layers of clouds separated by clear-sky in between.

MODTRAN5 limits the number of discrete pressure levels in which cloud water content can be specified to between 3 and 16. As we use the original ERA5 vertical levels in the input file to MODTRAN5, this cloud layering limitation reduces the total ice and liquid cloud profiles used in this study to 2102 and 3860, respectively.

For both the liquid and ice cloud profiles, 300 profiles are randomly selected and used as training samples. These random training profiles consist of samples from both months and polar regions and are used to establish far-IR and mid-IR BTD thresholds. The test data for validation and evaluation purposes consists of the remaining 1802 ice and 3560 liquid cloud samples.

4.2.2 Simulations of Spectral Radiance

Two sets of spectral radiances are simulated using each cloudy profile, one with the clouds and the other with the clouds removed. The latter cases are referred to as "clouds-removed" cases and are included so that the role of the clouds in the BTDs can be examined. Additionally, a total of 500 randomly selected ERA5 polar clear-sky profiles (not the same as clouds-removed) are used

for clear-sky radiance simulations so that the role of water vapor in far-IR ice phase determination can be assessed.

Nadir-view outgoing spectral radiances at the TOA are generated from 400 cm^{-1} to 1300 cm^{-1} with a spectral resolution of 1 cm^{-1}. An eight-stream DISORT solver (Stamnes et el., 1988) built into MODTRAN5 is used for all scattering calculations.

The ice bulk absorption and scattering models from Baum et al. (2014) are used in ice cloud radiance calculations. These models are based on the ice particle single scattering property database developed by Yang et al. (2013). Specifically, the ice cloud optical property (COP) models are based on a general habit mixture, which consists of nine common ice habits (Baum et
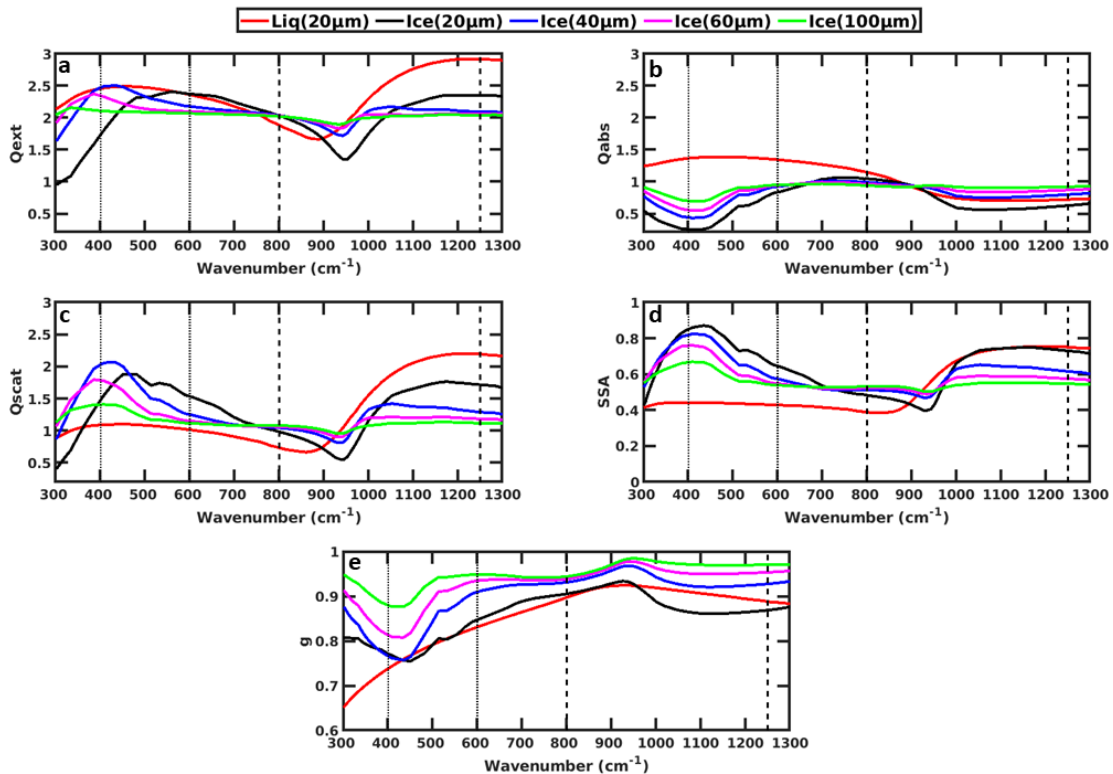
Figure 4.1. Bulk ice cloud and liquid cloud optical properties (COPs): (a) Extinction efficiency, (b) absorption efficiency, (c) scattering efficiency, (d) single scattering albedo, (e) scattering asymmetry parameter. Colors as labeled above the plots indicate one liquid droplet diameter and four ice effective diameters. Vertical dotted and dashed lines bracket the far-IR dirty window region and mid-IR window, respectively.

al., 2014). The bulk ice COP models are developed for a given wavelength by integrating over the single scattering properties of individual habit and particle size distributions (PSDs) from 14,000 aircraft measurements, and the ice COPs are then averaged across the 14,000 cases. The ice PSDs were assumed to be gamma distributions. Figure 4.1 shows five COPs: Bulk absorption efficiency (Q_{abs}), scattering efficiency (Q_{scat}), extinction efficiency (Q_{ext}), single scattering albedo (SSA), and scattering asymmetry factor (*g*). COPs are provided at wavelengths from 3 to 99 µm and for effective ice particle diameters (D_{eff_ice}) ranging from 10 to 180 µm at 5 µm increments. Such ice COPs are linearly interpolated to the spectral channels in our simulations. D_{eff_ice} values of 20, 40, 60, and 100 µm are used respectively for ice cloud radiance simulations, so cloudy training and test spectra for each D_{eff_ice} value are derived. These groups of spectra are henceforth referred to as the D_{eff_ice} groups. Mie scattering is used to derive the COPs for all liquid clouds assuming a 20 µm droplet diameter. Reducing diameter to 10 µm has a negligible impact on the BTD performance on liquid cloud cases (not shown). Thus, for brevity, only the 20 µm droplet diameter is used for liquid clouds in the following discussion.

Figure 4.2 shows the histograms of visible cloud optical depth (COD; see section 4.2.2 for details on COD calculation) and CTP for the finalized set of liquid and ice cloud profiles used in this study. In addition, to obtain cloud optical depth (COD or τ) in each spectral channel mentioned above, the cloud extinction optical depth at 0.55 µm is also computed assuming $Q_{ext\_ice}=2$ at 0.55 µm. Following the convention in optical cloud remote sensing, unless specified otherwise, all cloud optical depths mentioned hereafter refer to the visible cloud optical depth at 0.55 µm.
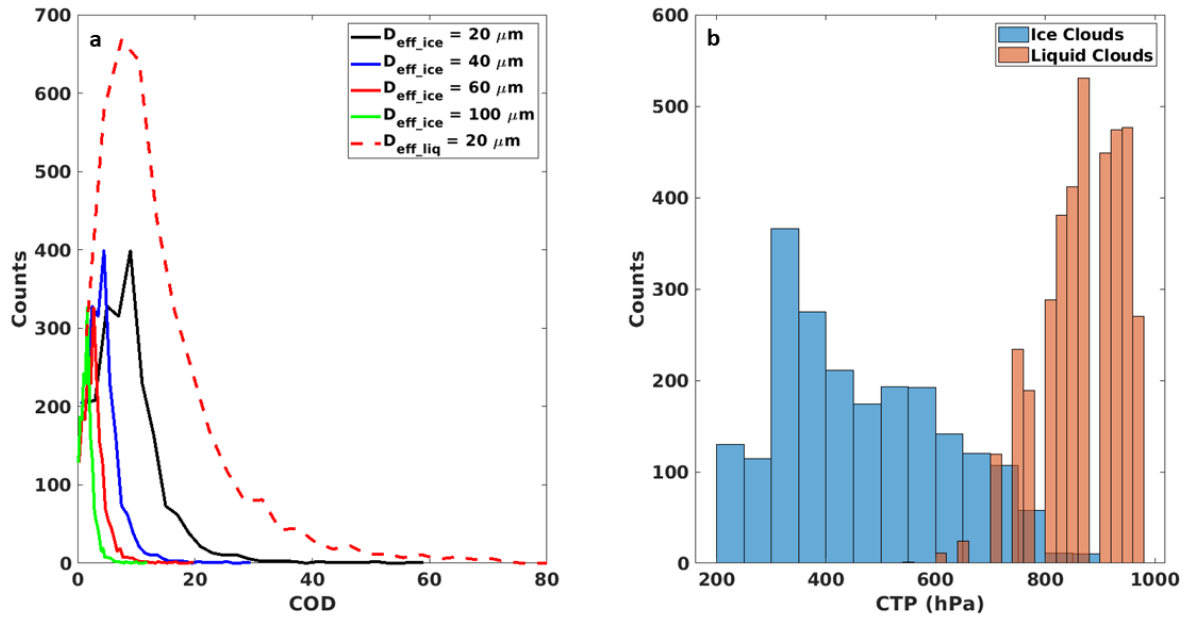
Figure 4.2. Visible cloud optical depth (COD) and cloud-top-pressure (CTP) histograms for the 2102 ice cloud cases using all four D_{eff_ice} and 3860 liquid cloud cases with one droplet size. The data includes both the training and testing datasets.

4.3. Theoretical Basis for Far-IR Ice Phase Determination

This section first compares the far-IR and mid-IR ice and liquid COPs. The roles of scattering, absorption, and water vapor are then discussed in more detail, followed by a description of the far-IR ice phase BTD test. In general, the channels of choice should sit within a spectral micro window between absorption lines such that the influence of water vapor can be minimized. Such channels should have enough contrast in terms of ice vs. liquid COPs (as well as ice COPs vs. clear-sky absorption) so the BTD can be used for ice cloud detection. Based on these considerations, 449 cm^{-1} and 521 cm^{-1} are chosen as the two channels for the far-IR BTD ice cloud determination. The far-IR BTD test metric is thus referred to as BTD$_{449\text{-}521}$ (i.e., BT$_{449}$ − BT$_{521}$, where BT is the brightness temperature of the stated channel). The selection of these two channels is determined by optimizing the synergy between far-IR ice absorption and scattering and accounting for clear-sky water vapor absorption in each channel, as discussed below.

4.3.1 Comparison of Far-IR and Mid-IR Ice Cloud Optical Properties

Using a BTD test to determine whether a cloud is composed of ice or liquid particles relies on the ways that cloud particles can affect the TOA brightness temperature in two different channels. Figure 4.1 shows the optical properties of ice cloud particles with the four aforementioned D_{eff_ice} values as well as liquid cloud particles with a diameter of 20 µm. Comparing the spectral variations of COPs in the far-IR dirty window region to their counterparts in the mid-IR window, several noteworthy facts are as follows:

(1) Except for g, other optical properties of liquid cloud have much smaller spectral variations in the far-IR dirty window region than in the mid-IR window. For example, Q_{ext_liq} varies between 1.67 and 3 in the mid-IR window, but only between 2.37 and 2.5 in the far-IR dirty window region. The SSA of liquid clouds remain essentially flat in the far-IR dirty window region but changes from 0.39 to 0.76 in the mid-IR window.

(2) In contrast, ice COPs exhibit much larger spectral variations in the far-IR dirty window region than liquid cloud counterparts. Q_{abs_ice} monotonically increases from 400 to 600 cm^{-1} for all ice particles examined here, and SSA monotonically decreases over the same spectral region. The SSA of ice clouds over 400-500 cm^{-1}, part of the far-IR dirty window region, can be significantly larger compared to the mid-IR window region, especially for small ice cloud particles. This implies that scattering can be more important in the far-IR BTDs than in the mid-IR BTDs. Consistent with the SSA spectral variation, except for the case of 20-µm D_{eff_ice}, Q_{scat_ice} also monotonically decreases from 400 to 600 cm^{-1}.

(3) Unlike the case in the far-IR dirty window region, ice COPs do not have a monotonic dependence with frequency in the mid-IR window. Note that spectral variation of

99

Q_{abs_ice} in the mid-IR window is one motivation for the mid-IR window BTD cloud phase classification (e.g., Ackerman et al., 1990).

(4) A larger ice particle has a larger forward scattering peak, as expected from the scattering theory. As a result, g increases with ice particle size for all frequencies. Moreover, over the far-IR dirty window region, SSA decreases with ice particle size for all frequencies, which is not the case for the mid-IR window.

4.3.2 Role of Absorption, Scattering, and Thermal Emission in Far-IR Ice Phase Determination

4.3.2.1 Dependence of BTD on cloud optical depth, cloud top pressure, and cloud particle size

A sufficient difference in ice attenuation of incident radiation between two spectral channels v_1 and v_2 can lead to a large enough BTD between the two channels (BTD$_{v1-v2}$) to confidently determine the cloud phase. For example, assuming the surface is warmer than the cloud and the cloud is semi-transparent, then more cloud absorption at v_1 than at v_2 can lead to a negative BTD. However, the far-IR dirty window region Q_{scat_ice}, in general, exhibits an opposite spectral dependence compared to Q_{abs_ice}, as described in the previous section. Moreover, thermal emission by clouds can further complicate the change of BT. This section focuses on the extent to which these radiative processes, namely scattering, absorption, and emission, can negate or support one another in far-IR ice phase determination.

For all four D_{eff_ice}, absorption efficiency at 521 cm^{-1}, denoted as $Q_{abs\_ice}(521)$, is greater than at 449 cm^{-1} $Q_{abs\_ice}(449)$. Thus, for an ice cloud, absorption and emission alone would always result in a non-negative BTD$_{449-521}$ if the surface is warmer than the cloud, assuming the surface emissivity is similar between the far-IR spectral channels, which is the case for the ocean surface

emissivity used for all simulations. On the other hand, $Q_{scat\_ice}(449)$ is greater than $Q_{scat\_ice}(521)$ in all the ice cloud cases. Figure 4.3 shows the simulated $BTD_{449-521}$ for two single-layer ice clouds
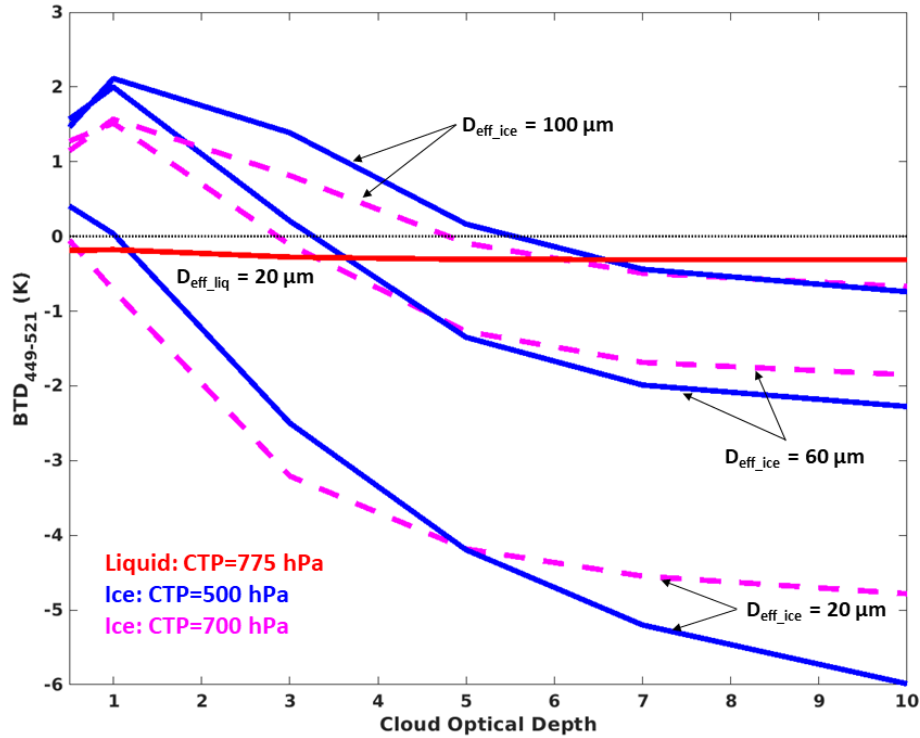
Figure 4.3. Brightness temperature (BT) difference (BTD; 449 cm^{-1} BT minus 521 cm^{-1} BT) for a single-layer cloud. The ice cloud tops are at 500 hPa (blue solid lines) or 700 hPa (pink dashed lines) and the liquid cloud top is 775 hPa (solid red line). All ice clouds are 50 hPa thick and the liquid cloud is 25 hPa thick. Results are shown for ice clouds with 100 μm, 60 μm and 20 μm D_{eff_ice}. A set of typical Arctic winter temperature and humidity profiles from the ERA5 reanalysis is used for all calculations.

with different CTPs and a single-layer liquid cloud. The results are shown for a range of CODs (0.5-10) and for three different D_{eff_ice} values and one D_{eff_liq} value (20 μm). The liquid cloud $BTD_{449-521}$ is between -0.2 and -0.3 K, nearly constant, when COD varies from 0.5 to 10. When D_{eff_liq} is changed from 20 μm to 10 μm (not shown), the $BTD_{449-521}$ range only changes from -0.3 K to -0.35 K. The $BTD_{449-521}$ range also changes by a negligible amount when the liquid cloud CTP is changed to 500 hPa (i.e., cloud base at 550 hPa).

In ice clouds, both D_{eff_ice} and CTP can impact the sign of $BTD_{449-521}$. The difference between two CTPs shows the influence of water vapor between 500 and 700 hPa on $BTD_{449-521}$.

For the same COD and CTP, $BTD_{449-521}$ increases with D_{eff_ice}. For a D_{eff_ice} of 60 or 100 µm, $BTD_{449-521}$ increases slightly with COD until COD = 1 and then decreases when COD >1. For the 20 µm case, $BTD_{449-521}$ decreases monotonically with COD. Note that $BTD_{449-521}$ can be either positive or negative, which is a clear indication that absorption and emission alone cannot be used to interpret the variation of $BTD_{449-521}$ and scattering must play a non-negligible role.

4.3.2.2 A sensitivity study and its implication for the importance of far-IR scattering

To understand the effects of far-IR ice cloud scattering vs. absorption and emission on $BTD_{449-521}$, we performed a sensitivity study with artificially modified SSA at 449 cm^{-1}. The COPs at 521 cm^{-1} are the same as in Figure 4.3, along with Q_{ext_ice} and g at 449 cm^{-1}. SSA at 449 cm^{-1} is artificially changed from 0.1 to 0.98. To reduce the influence of water vapor absorption, the CTP
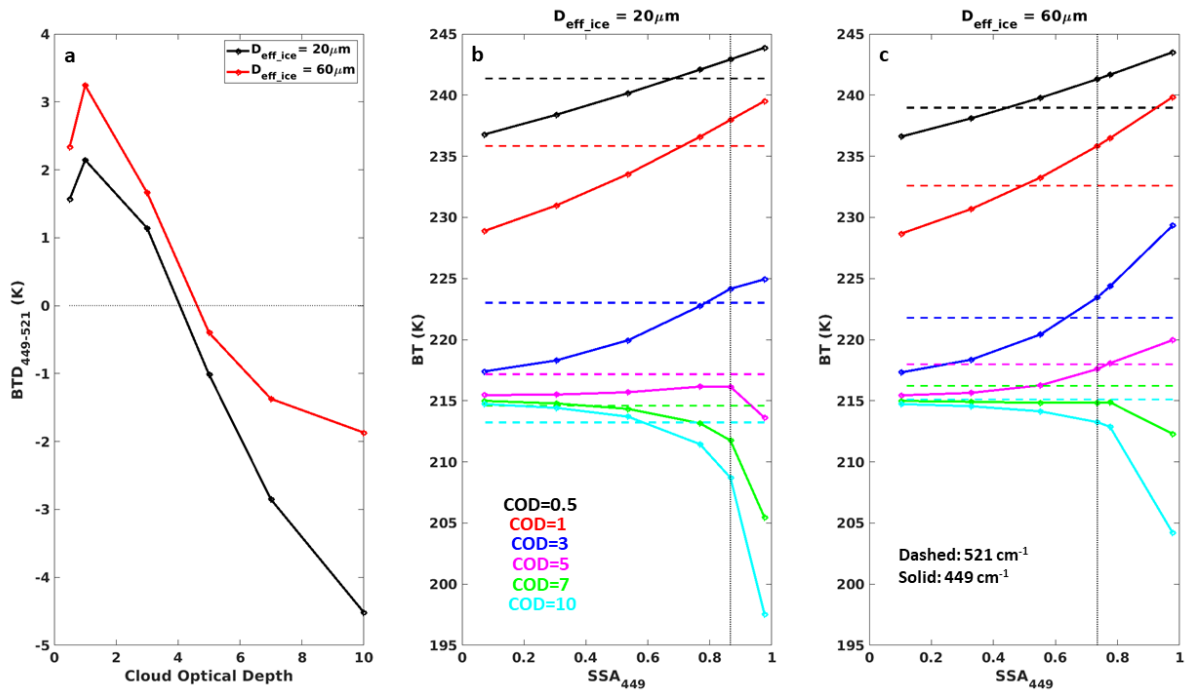
Figure 4.4. (a) BTD at 449 cm-1 minus 521 cm-1 for a single-layer ice cloud topping at 300 hPa and Deff_ice = 20 µm (black line) or 60 µm (red line). The cloud thickness is 50 hPa. (b) BT at 449 cm-1 (solid lines) for the same cloud as in (a) with Deff_ice = 20 µm and varying optical depth as labeled. SSA at 449 cm-1 varies while Qext_ice remains constant. For comparison, the actual BT at 521 cm-1 as in (a) is shown as a horizontal dashed line. The vertical dotted line indicates the actual SSA for 449 cm-1 as used in (a). (c) Same as (b) but for Deff_ice = 60 µm. The temperature and humidity profiles are the same as used in Figure 4.3.

in this sensitivity study is set at 300 hPa (CTT = 214 K). The surface temperature is 249 K. Computing BT_{449} and BT_{521} using MODTRAN5, Figure 4.4 shows results for a range of CODs and D_{eff_ice} values of 20 and 60 µm.

For both D_{eff_ice} cases, BT_{449} increases with SSA when the cloud is not opaque enough (i.e., when COD < 7 for the 20 µm case and COD < 10 for the 60 µm case). However, when COD ≥ 5 for the 20 µm D_{eff_ice} case and COD ≥ 7 for the 60 µm D_{eff_ice} case, BT_{449} first increases and then decreases with SSA. For the actual SSA at 449 cm^{-1} (0.87 for 20 µm and 0.73 for 60 µm; vertical dotted lines in Figure 4.4b and 4.4c), BT_{449} is larger than BT_{521} for the non-opaque cloud but smaller than BT_{521} for the opaque cloud, leading to a positive $BTD_{449-521}$ for the non-opaque cloud and negative $BTD_{449-521}$ for the opaque cloud (Figure 4.4a). This confirms that negative $BTD_{449-521}$ values seen in Figure 3 indeed can be caused by clouds as water vapor amounts above 300 hPa in the polar regions are negligible.

As mentioned above, considering only absorption and emission, $BTD_{449-521}$ should be always non-negative if the surface temperature is higher than the CTT (approaching 0 K when COD approaches infinity). Negative $BTD_{449-521}$ implies that scattering must play an important role in the far-IR cloudy radiative transfer. To further understand why BT_{449} changes with SSA in different ways for non-opaque and opaque clouds, we employed the two-stream approximation method to analytical solve multiple-scattering radiative transfer in the presence of thermal emission (Fu et al., 1997). Details can be found in the Appendix. When the COP and the atmosphere profile are chosen to be consistent with those used in Figure 4, the two-stream solution can reproduce the change of BT_{449} with SSA for both opaque and non-opaque cases (Figure A3d). Moreover, the two-stream solution elucidates on the reasons for such dependence of BT_{449} on SSA.

In brief, upwelling radiance at the cloud top consists of three components, coupled together due to the nature of multiple scattering: (1) Upwelling radiance that is originated below the cloud but attenuated by the cloud, (2) reflection of downwelling radiance by and throughout the cloud, and (3) thermal emission throughout the cloud that reaches the cloud top. The optical thickness of the cloud plays an important role for modulating the relative contributions of both components (1) and (3) compared to component (2). As SSA increases from zero to one, cloud absorption optical depth decreases from τ_{ext} (cloud extinction optical depth at 449 cm^{-1}) to zero, thus, components (1) and (3) always increase regardless of the cloud optical depth. However, the rate of increase for components (1) and (3) with SSA is much slower for an opaque case (i.e., $\tau_{ext} \gg 1$) compared to a non-opaque case (i.e., $\tau_{ext} \sim 1$ or $\tau_{ext} < 1$). This is because when $\tau_{ext} \gg 1$, for a wide range of SSA, $(1-SSA)\tau_{ext}$ is much larger than one. As a result, little upwelling radiance originating below the cloud base, or in-cloud thermal emission below the cloud top, can reach the cloud top. For the non-opaque case however, upwelling radiance originating below the cloud base or in-cloud thermal emission can always reach the cloud top, and thus the rate of increase of components (1) and (3) with SSA is much larger compared to the opaque case.

Component (2), reflection of downwelling radiance by and throughout the cloud, is fundamentally related to multiple scattering. For both the opaque and the non-opaque cases, component (2) decreases with SSA due to the upper boundary condition and the dependence of multiple scattering with SSA, however, but the rate of decrease is almost the same for both cases, at least for the COP studied here. As a result, when all components are combined, the change of components (1) and (3) with SSA dominates over the change of component (2) for the non-opaque case, increasing BT$_{449}$ with SSA; the change of component (2) dominates for the opaque case, decreasing BT$_{449}$ with SSA.

Both the two-stream results and MODTRAN5 sensitivity studies shown in Figure 4.4 indicate that the $BTD_{449-521}$ is affected by multiple scattering the most when the cloud is opaque, where $BTD_{449-521}$ becomes negative due to the dominance of component (2).

4.3.3 Contribution of Water Vapor Absorption and Emission to the Far-IR BTDs

Over the entire spectral range, the far-IR dirty window region has much stronger water vapor absorption than the mid-IR window. However, so-called "micro-windows" exist between adjacent water vapor absorption lines within the far-IR window as shown in Figure 4.5a. These micro-windows are utilized for BTD channel selections in the far-IR. The contribution of water vapor to the BTD signal depends on the amount of water vapor above the cloud, as well as the difference in clear-sky optical depths in the two channels caused by this amount of water vapor. It is most desirable for the BTD channels to have water vapor optical depths as small as possible so
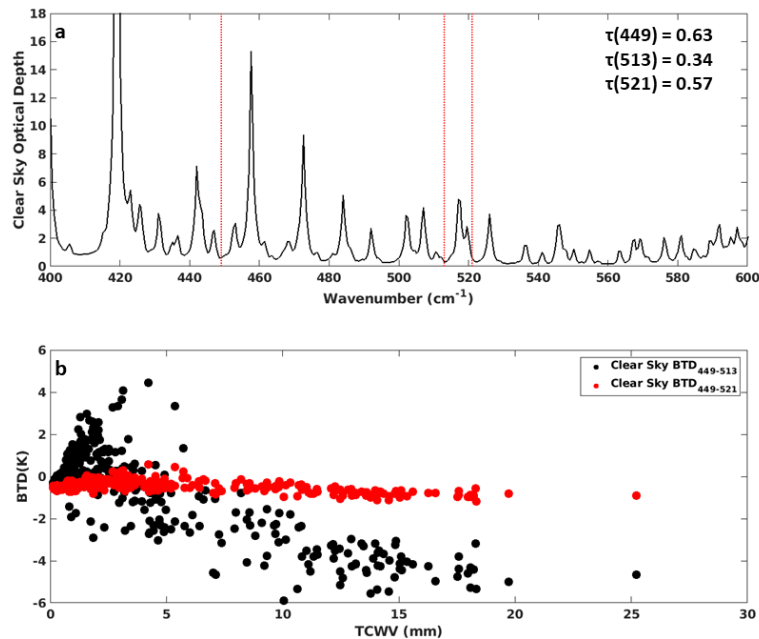
Figure 4.5. (a) The clear-sky optical depth for the far-IR dirty window region. The temperature and humidity profiles are the same as in Figure 3. The TCWV of this profile is 3 mm. Red vertical lines correspond to three wavenumbers, 449 cm^{-1}, 513 cm^{-1}, and 521 cm^{-1}. (b) BTDs as a function of total column water vapor for 500 clear sky profiles from ERA5 data over the polar regions (60°N-90°N and 60°S-90°S) for January and July 2005.

the cloud phase throughout the troposphere can be determined. Moreover, the two channels should

have similar water vapor optical depths. For the two channels that we chose for the far-IR BTD test (i.e., 449 and 521 cm^{-1}), their clear-sky optical depth is 0.63 and 0.57 (transmissivities of 0.53 and 0.57), respectively, for a typical Arctic winter profile.

Figure 4.5b shows BTDs with respect to total column water vapor for 500 clear-sky profiles. For comparison, BTDs between 449 cm^{-1} and another micro-window channel, 513 cm^{-1}, are also shown where the clear-sky optical depth for 513 cm^{-1} is 0.34 (a transmissivity of 0.71) For BTD$_{449-513}$, the clear-sky contribution ranges from 4.25 K to -6 K and becomes more negative as total column water vapor (TCWV) is increased, as the clear-sky optical depth is larger at 449 cm^{-1} than at 513 cm^{-1}. When 521 cm^{1} is used instead of 513 cm^{-1}, BTD$_{449-521}$ has much less variation with total column water vapor and is narrowly confined within -1.2 to 0.56 K. This contrast between BTD$_{449-521}$ and BTD$_{449-513}$, from the point of view of water vapor interference, supports the 449 and 521 cm^{-1} pair.

4.3.4 Establishing the BTD$_{449-521}$ Thresholds for Ice Cloud Detection

Figure 4.6a shows BTD$_{449-521}$ computed for all training profiles of the four D$_{eff\_ice}$ groups, and BTD$_{449-521}$ values for the training ice cloud-removed profiles. Figure 4.6b shows BTD$_{449-521}$ derived from all liquid cloud training profiles and from the liquid-cloud removed profiles. Figure 4.6c shows BTD$_{449-521}$ derived from the 500 clear-sky profiles used in Figure 4.5b. BTD$_{449-521}$ ranges from -6.5 K to 3.2 K in the four D$_{eff\_ice}$ groups, with large particle groups tending to have more positive BTD$_{449-521}$. BTD$_{449-521}$ values for cloud-removed profiles, liquid cloud training profiles, and clear-sky profiles are mostly between -1.5 K and 0 K. Based on these observations, two thresholds are chosen by visual inspection for the ice cloud determination: BTD$_{449-521}$ ≥ 0.5 K and BTD$_{449-521}$ ≤ -1.5 K (two horizontal dashed lines in Figure 4.6a). The conservative thresholds are chosen to avoid misclassification of clear sky and liquid cloud scenes as ice clouds, while also

accounting for the signs and magnitudes of the ice cloud BTDs. For -1.5 K< $BTD_{449-521}$ <0.5 K,

further tests can be made to determine whether the pixel is a liquid cloud, ice cloud, or clear-sky
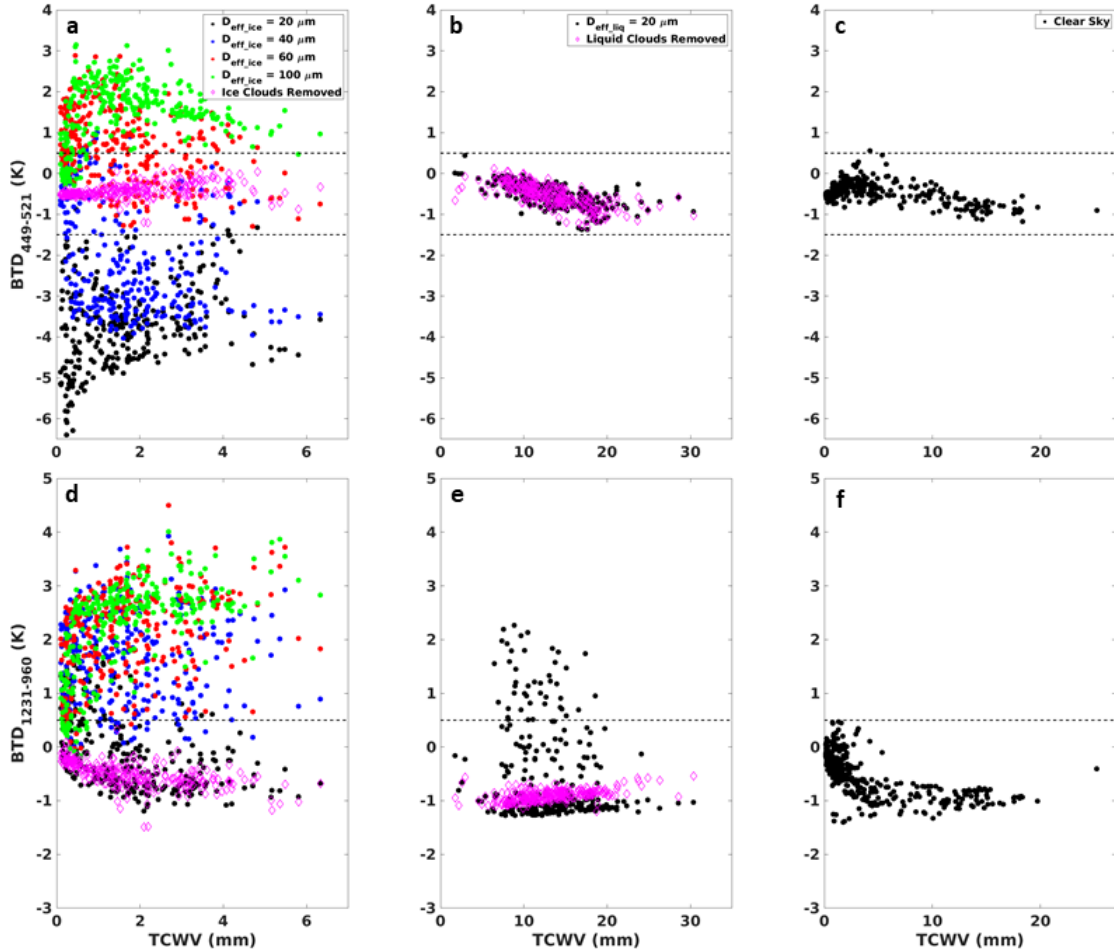
Figure 4.6. (a) BTDs at 449 cm^{-1} minus 521 cm^{-1} from the training dataset. Solid filled circles are for different D_{eff_ice} and pink diamonds are for the same profiles with clouds removed. Horizontal dashed lines represent the thresholds defined in the $BTD_{449-521}$ test. (b) Same as in (a) but only for the liquid cloud training profiles (black dots) and the same profiles with clouds removed (pink diamonds). (c) Similar to (b) but for the same polar clear sky profiles used in Figure 4.5. (d-f) same as (a-c) but for the $BTD_{1231-960}$ test.

scene. Figure 4.6a shows some misclassified ice-cloud cases in the (-1.5 K, 0.5 K) range. The 40

and 60 µm D_{eff_ice} groups are misclassified more so than the other size groups mainly due to the

competing effects of absorption and scattering (see Figures 4.3 and 4.4). It should be noted that

the TCWV of the data used in this study is correlated with COD, where the driest ice-cloud cases

tend to have CODs smaller than 1, and this causes $BTD_{449-521}$ to approach zero as the cloud becomes less and less opaque.

4.4. A Comparison of the Far-IR and Mid-IR Ice Cloud Determination Skill

Using the test data sets, this section compares the $BTD_{449-521}$ test performance with a comparable mid-IR BTD test. First a mid-IR BTD test that closely follows the AIRS cloud phase algorithm is introduced, followed by an assessment of the relative roles of $D_{eff\_ice,}$ COD and CTP on the performance of the $BTD_{449-521}$ and mid-IR BTD tests.

4.4.1 Selection of the Mid-IR BTD Test

The mid-IR BTD test used here is based on the AIRS ice cloud classification tests described in Kahn et al. (2014). For ice cloud classification, AIRS uses three BTD tests: $BTD_{1231-960}$ >0 K, $BTD_{1227-960}$ >-0.5 K and $BTD_{1231-930}$ >1.75 K. The mid-IR test will be henceforth referred to as $BTD_{1231-960}$ test because we use the BTs at 1231 and 960 cm^{-1} directly from our simulation, which are not the same as the synthetic AIRS radiances (slightly different spectral frequencies, and no convolution with the AIRS individual spectral response function). Nevertheless, with a resolving power of $\Delta\nu/\nu=1200$, the spectral resolution of the two AIRS channels (1231 cm^{-1} and 960 cm^{-1}) are comparable to the spectral resolution in our simulation. Due to aforementioned differences between the "AIRS-Like" mid-IR and true AIRS channels, our $BTD_{1231-960}$ threshold is modified based on inspection of $BTD_{1231-960}$ values derived using the ice and liquid cloud training profiles (Figure 4.6 d-f): $BTD_{1231-960} \geq 0.5$ K is used to classify an ice-phase cloud. Note that the results from the $BTD_{1231-960}$ test used in this study should not be directly compared to results obtained from the true AIRS spectra (i.e., the spectra obtained by convolving the AIRS instrument response

function). The same synthetic spectra are used for the $BTD_{449-521}$ and $BTD_{1231-960}$ tests so that the results can be directly compared.

4.4.2 Influence of Ice Particle Size on the Performance of Far-IR and Mid-IR BTDs

Figure 4.7a shows the true positive rates (percentage of cases that ice clouds are correctly identified from the simulated BTs) for four different BTD tests: (1) The $BTD_{449-521}$ test, (2) the $BTD_{1231-960}$ test, (3) a test in which either test is passed, and (4) a test in which both tests are passed
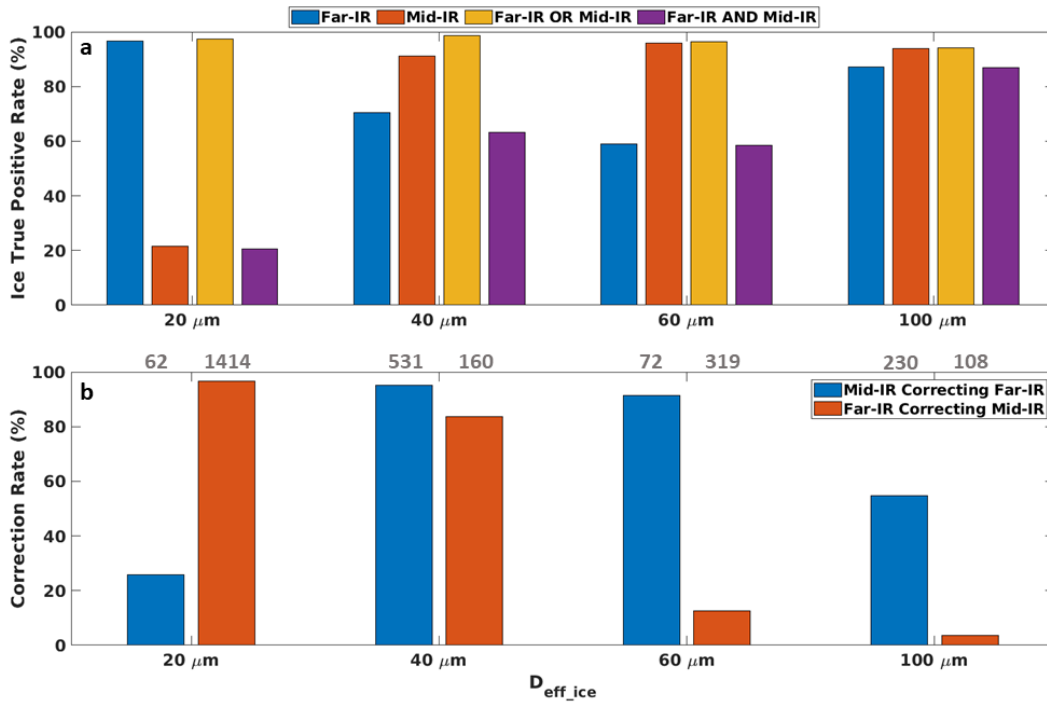
Figure 4.7. (a) True postive rates for ice-phase determination when the BTD tests are applied to the testing dataset. (b) Percentage of ice cloud cases misclassified by one BTD test but classified correctly by the other BTD test. Numbers above bars represent the actual number of cases misclassified by a given BTD test. The far-IR and mid-IR tests refer to $BTD_{449-521}$ and $BTD_{1231-960}$, respectively.

simultaneously.

For the $BTD_{449-521}$ test, the true positive rates are 96.6%, 70.5%, 59.0%, and 87.2% for 20, 40, 60, and 100 µm D_{eff_ice}, respectively. The results above suggest that the $BTD_{449-521}$ test is most

effective for the 100 and 20 µm D_{eff_ice} groups. This is expected because the 100 µm cases tend to have large positive BTDs and the 20 µm cases tend to have large negative BTDs, i.e., well separated from the double thresholds defined in Subsection 4.3.4 (shown in Figure 4.6).

For the $BTD_{1231-960}$ test, the true positive rate for ice cloud classification is 21.5%, 91.2%, 96.0%, and 94.0% for 20, 40, 60, and 100 µm D_{eff_ice}, respectively. Such true positive rates are larger than the counterparts from the $BTD_{449-521}$ test for all D_{eff_ice} groups except the 20 µm group. For the 20 µm group, the difference in the true positive rate between the two methods is ~ 75%, indicating the $BTD_{449-521}$ test is highly effective for identifying ice clouds consisting of such small ice particles. For the rest of the D_{eff_ice} groups, the $BTD_{1231-960}$ true positive rate exceeds the $BTD_{449-521}$ true positive rate by ~7%-37%. When either the $BTD_{449-521}$ or the $BTD_{1231-960}$ test is used to identify an ice cloud, the true positive rate exceeds 90% for all D_{eff_ice} groups. This suggests a synergy in the joint use of the $BTD_{449-521}$ and $BTD_{1231-960}$ tests. When both the $BTD_{449-521}$ and $BTD_{1231-960}$ tests must be passed, the test is much stricter; as a result, the true positive rate largely follows the $BTD_{1231-960}$ test for the 20 µm group, follows the $BTD_{449-521}$ test for the 60 µm and 100 µm groups, and is significantly smaller than the true positive rate of both $BTD_{449-521}$ and $BTD_{1231-960}$ tests for the 40 µm group.

Given the different performances of the $BTD_{449-521}$ and $BTD_{1231-960}$ BTD tests shown in Figure 4.7a, it is of interest to evaluate the extent to which the two BTD tests can correct for each other's misclassifications. Figure 4.7b shows the percentage of the $BTD_{449-521}$ test misclassifications that can be classified correctly by the other test. The $BTD_{1231-960}$ test corrects 25%, 95.1%, 91.5%, and 54.8% of the $BTD_{449-521}$ misclassification cases for the 20, 40, 60, and 100 µm D_{eff_ice}, respectively. The $BTD_{449-521}$ test corrects 96.7%, 83.8%, 12.5%, and 3.7% of the $BTD_{1231-960}$ test misclassifications for the 20, 40, 60, and 100 µm D_{eff_ice}, respectively. These results

further show the synergy between the $BTD_{449-521}$ and $BTD_{1231-960}$ tests: The $BTD_{449-521}$ test works better than the $BTD_{1231-960}$ test for cases of smallest ice particle size while the $BTD_{1231-960}$ test works better for cases of larger ice particle sizes.

Out of all the liquid cloud cases from the test data, the $BTD_{1231-960}$ test misclassified 14.41 % of them as ice clouds while the $BTD_{449-521}$ test misclassified 0.1%. For the 500 clear-sky cases, the misclassification rates are 0.2% and 0%, respectively.

4.3 Influence of CTP and COD on the Performance of Far-IR and Mid-IR BTD Tests

This subsection further examines the dependence of the $BTD_{449-521}$ and $BTD_{1231-960}$ test skill on COD and CTP, using the test dataset. Following International Satellite Cloud Climatology Project (ISCCP; Rossow & Schiffer, 1999) conventions, CTP is categorized into three groups (50-440 hPa, 440-680 hPa, and >680 hPa) and COD into two groups (non-opaque cloud COD < 3.6 and opaque cloud COD $\geq$ 3.6). Results are shown in Figure 4.8. Each of the CTP-D_{eff_ice} bins for each COD group can have different amounts of cloud cases associated with it (see gray numbers in Figure 4.8b and 4.8e), as changing D_{eff_ice} for the cloud cases changes the CODs of those cases. It should be noted that the testing data used here is randomly sampled from the cases with COD and CTP distributions shown in Figure 4.2. A few notable points in Figure 4.8 are as follows:

(1) Figure 4.7 shows the superiority of the far-IR to the mid-IR for 20 µm D_{eff_ice}. Figure 4.8 reveals more pronounced superiority for opaque than for non-opaque cloud cases. The $BTD_{1231-960}$ test has a 40-68% true positive rate for non-opaque clouds depending on CTP (Figure 4.8b) but a 9-47% true positive rate for opaque clouds (Figure 4.8e). However, the $BTD_{449-521}$ test has greater than 97% true positive rate for opaque clouds at CTP >680 hPA

and an 88% true positive rate for CTP >680, while it is between 80% and 94% for the non-opaque clouds.
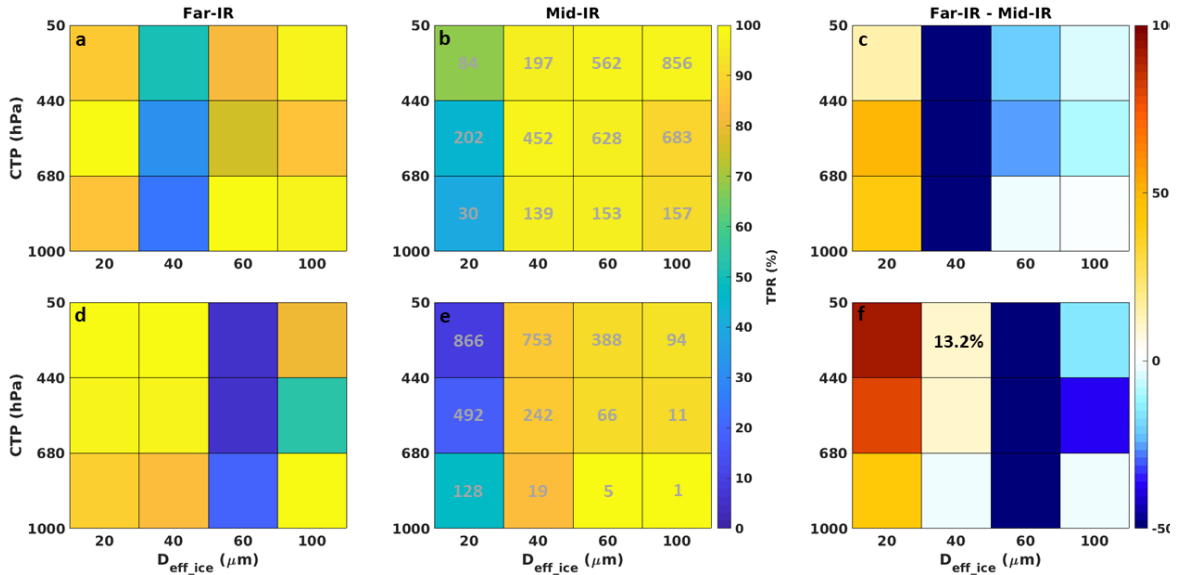
Figure 4.8. (a) True positive rates of far-IR BTD test applied to the testing dataset with COD < 3.6. The results are shown for each CTP group and each D_{eff_ice}. (b) same as (a) except for the mid-IR test. (c) Difference, (a) minus (b). (d)-(f) Same as (a)-(c), respectively, but for COD ≥ 3.6. The gray numbers in (b) and (e) represent the total number of samples in the testing dataset falling into each CTP bin. The black number in (f) indicates the true positive rate difference for that bin. The far-IR and mid-IR tests refer to $BTD_{449\text{-}521}$ and $BTD_{1231\text{-}960}$, respectively.

(2) For the non-opaque group with a 40-µm D_{eff_ice}, the true positive rate of the $BTD_{1231\text{-}960}$ test exceeds that of the $BTD_{449\text{-}521}$ test by 47% to 68%, depending on CTP (Fig. 4.8c). However, for the opaque group with the same D_{eff_ice}, the situation is opposite: The $BTD_{449\text{-}521}$ test true positive rate exceeds the $BTD_{1231\text{-}960}$ test by 11% to 13% for CTP >680 hPa, while both tests have equal true positive rates for CTP>680 hPa (Fig. 4.8f). Similar to what has been discussed in Section 3.2, the scattering effect on $BTD_{449\text{-}521}$ is more prominent in opaque clouds with small particles, while the $BTD_{1231\text{-}960}$ test (based on ice cloud absorption) is less useful. For non-opaque clouds with the same ice particle size, the absorption effect is strong enough that the $BTD_{1231\text{-}960}$ test has sufficient skill. Such a synergy between the $BTD_{449\text{-}521}$ and $BTD_{1231\text{-}960}$ tests can also be seen in Figure 7, where

the joint use of both BTD tests leads to a true positive rate for 40 µm D_{eff_ice} that exceeds the rates of each individual test (which is not the case for the other D_{eff_ice} groups). The high (>80%) mutual correction rate between the $BTD_{449-521}$ and $BTD_{1231-960}$ tests (see Fig. 7b) for the 40-µm D_{eff_ice} cases are due to this far-IR and mid-IR synergy.

(3) In general, D_{eff_ice} appears to be responsible for the most variability in true positive rates for both $BTD_{1231-960}$ and $BTD_{449-521}$ tests. The dependence on COD and CTP is secondary, which indicates that ice cloud microphysical properties are the major determining factor of performance of both $BTD_{449-521}$ and $BTD_{1231-960}$ tests in this study.

4.4 Impact of Measurement Uncertainty on the Far-IR and Mid-IR BTDs

This section briefly addresses the implications of random measurement noise on $BTD_{449-521}$ and $BTD_{1231-960}$ for the ice cloud scenes. Here we use the noise equivalent spectral radiance (NeSR) estimates for the FORUM instrument in Ridolfi et al. (2020), i.e., 0.4 mW $m^{-2}sr^{-1}cm^{-1}$ for 200–800 cm^{-1} and 1.0 mW $m^{-2}sr^{-1}cm^{-1}$ for 800–1,600 cm^{-1}. As usual, the noise distribution in each channel is assumed to be gaussian with standard deviations equal to the corresponding NeSR. Conversion of "noisy" radiances to BT results in the BT at each channel having a noise equivalent differential temperature (NeDT). The resulting variance of the BTD between two channels will be the sum of the squared NeDT for each channel used in the BTD.

To numerically illustrate how the NeSR translates to the $BTD_{449-521}$ and $BTD_{1231-960}$ uncertainty, radiances at 449, 521, 1231, and 960 cm^{-1} are generated for 500 ice cloud cases (250 in January and July, respectively). For each ice cloud case and at a given spectral channel, 100 noise instances are added to the channel radiance to produce 100 instances of BTs at that channel. For each channel, the group of 100 noise instances are different. The $BTD_{449-521}$ and $BTD_{1231-960}$ are computed for each of the 100 instances of the BT spectra and the BTD variance is computed

directly from the data. Such BTD variances are computed for all 500 ice cloud samples and then averaged across all the samples. This results in the uncertainty (defined here as the square root of the sum of the squared NeDTs of the two channels in the BTD) of $BTD_{449-521}$ to be 0.6 K, while it is 3.1 K for $BTD_{1231-960}$.

These results imply that the estimated FORUM NeSR can result in ice cloud misclassifications using the $BTD_{449-521}$ and $BTD_{1231-960}$ tests. However, it is important to note that the actual FORUM NeSR could be different from the estimates in Ridolfi et al. (2020). It is also important to note that these NeSR estimates are for the native 0.36 cm^{-1} spectral resolution of FORUM. To approximately obtain the BT at the 1 cm^{-1} spectral resolution used in this study, the BT between three adjacent FORUM channels can be averaged. This would reduce the NeDT for the averaged results and the uncertainty of the BTD between two channels by a factor of $\sqrt{3}$. Assuming the BTD uncertainty estimates in our calculations can be applied to the FORUM channel resolution, this would result in a $BTD_{449-521}$ and $BTD_{1231-960}$ uncertainty of 0.35 K and 1.79 K, respectively. In this sense, a BTD tests with spectral resolution at the order of 1 cm^{-1} can be still applicable for FORUM-like measurements.

4.5. Summary and Conclusion

This study uses synthetic spectra generated from the ERA-5 reanalysis profiles to develop a physically based far-IR BTD test ($BTD_{449-521}$) and to compare this far-IR BTD test with the normally used mid-IR BTD test for ice cloud identification. The dry polar atmosphere makes the far-IR dirty window region more transparent than elsewhere. As a result, the far-IR dirty window region can be used for cloud phase determination. Ice cloud optical properties exhibit different spectral dependences between the far-IR dirty window and mid-IR window regions. As a result, multiple scattering needs to be considered in the far-IR, especially when the cloud is opaque.

The channel selection process for the $BTD_{449\text{-}521}$ test involves accounting for water vapor and the variation in ice COPs across the far-IR dirty window region. The resulting $BTD_{449\text{-}521}$ test is subjected to competing effects of absorption and scattering, where absorption tends to result in positive $BTD_{449\text{-}521}$ and multiple scattering causes negative $BTD_{449\text{-}521}$. Thus, conservative positive and negative $BTD_{449\text{-}521}$ thresholds are selected to minimize the chance that a clear-sky or liquid cloud scene is misclassified as an ice cloud scene. Our study assumes a spectral resolution of 1 cm^{-1}, which is about three times as coarse as the spectral resolution of the future FORUM mission. Thus, three adjacent FORUM spectral channels can be merged to make such a $BTD_{449\text{-}521}$ test applicable. Similarly, for actual observations made at a comparable spectral resolution but different spectral sampling grids, channels around 449 and 521 cm^{-1} can be chosen and the thresholds can be adjusted accordingly.

Far-IR ice phase determination skill is assessed based on applying the $BTD_{449\text{-}521}$ test to test spectra generated with four assumed D_{eff_ice} values. A mid-IR BTD test ($BTD_{1231\text{-}960}$) that mimics the BTD test used by the AIRS operational algorithm was used here to evaluate the ice phase determination synergy between the far-IR and mid-IR. The $BTD_{449\text{-}521}$ test is more successful than the $BTD_{1231\text{-}960}$ test for identifying cloud scenes with the smallest ice particles studied here (20 µm). The $BTD_{1231\text{-}960}$ test is more successful than the $BTD_{449\text{-}521}$ test in cloud scenes with large particle sizes of 60 and 100 µm. For the intermediate D_{eff_ice} of 40 µm, the synergy between the $BTD_{449\text{-}521}$ and $BTD_{1231\text{-}960}$ tests is most obvious. While both BTD tests show some dependence on CTP and COD, they are more sensitive to the ice cloud particle size than other factors.

This study reveals that far-IR scattering, in addition to far-IR absorption, can be utilized for passive IR satellite detection of ice cloud phase in polar regions. Unlike absorption and

emission, scattering is not temperature dependent. As a result, when clouds are opaque, and the cloud and surface thermal contrast is low, the scattering signal can still be detected by the $BTD_{449-521}$ test. Given the ubiquitous existence of near-isothermal and inversion layers in the polar lower troposphere during the wintertime, this far-IR scattering effect makes far-IR measurements advantageous in cloud phase identification.

A couple of factors can affect the applicability of this study in reality. The most important assumption made in this study was that the ice COP database used to generate the synthetic radiances resembles the actual ice cloud properties in the Arctic. This database represents the state-of-the-art knowledge of ice cloud single scattering properties for many different habits. The bulk ice COPs are generated using a combination of common habits which is based on over 14,000 aircraft measurements taken over the tropics and midlatitudes, with one field campaign from Alaska (Verlinde et al., 2007). Thus, it is possible that, in polar regions, a different combination of habits would be more representative of the ice clouds in these regions. However, due in part to a limited number of aircraft campaigns in these regions, no bulk ice COP database has been produced specifically for the polar regions. The other factor is the fidelity of ERA5 temperature, humidity, and cloud water profiles in the Arctic. As reanalysis heavily relies on assimilated satellite observations for generating profiles in such regions, especially for cloud water profiles, the quality of assimilation can inevitably affect our results. The ERA5 reanalysis profiles were chosen for its spatial and temporal coverage. Future validation of ERA5 reanalysis profiles against in-situ observations in the Arctic can further improve the confidence of using ERA5 reanalysis in such studies.

This study provides an idealized perspective, and thus a demonstration with actual observations is a necessary next step before adoption of the far-IR BTD algorithm. Furthermore,

116

the applicability of this algorithm will be highly dependent on an instrument's spectral resolution and sampling due to the need for the BTD channels to coincide with water vapor micro-windows in the far-IR. It should also be noted that the impacts of mixed phase clouds were not addressed in this study, and such impacts should be investigated in the future.

The $BTD_{449-521}$ test developed here can be added to cloud detection algorithms in future space-borne far-IR remote sensing. Figure 4.9 proposes a decision tree. The first test, a cold-scene threshold test, passes if the 11µm BT is lower than 238 K, the threshold used in the MODIS Collection 6 cloud phase algorithm (Baum et al., 2012). If not passed, the $BTD_{449-521}$ test can be applied, followed by the $BTD_{1231-960}$ test. The $BTD_{449-521}$ test should precede the $BTD_{1231-960}$ test because the $BTD_{449-521}$ test has fewer misclassifications of liquid cloud and clear-sky scenes. Such decision tree can be integrated as part of a more comprehensive cloud physical retrieval algorithm for future missions with far-IR observational capability.

The far-IR alone is not suitable for liquid phase detection due to the lack of liquid COP spectral variation across the far-IR. However, from the far-IR dirty window to the mid-IR window, liquid COPs exhibit a large spectral variation. This indicates a possible use of one channel each from the far-IR and mid-IR to detect liquid cloud scenes. When used together with the far-IR ice

test in the polar region, there might be even a chance for further identifying mixed-phase cloud scenes.
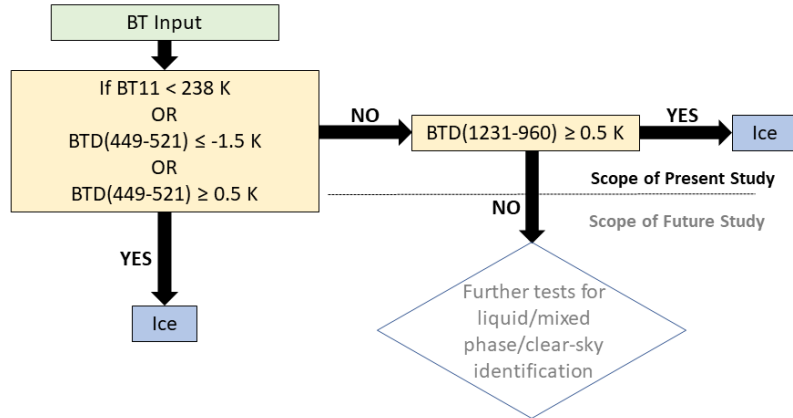
Figure 4.9. A proposed cloud phase determination decision tree that incorporates far-IR and mid-IR tests. Note that this study only investigates ice phase determination.

Acknowledgements

References

Ackerman, S. A., Smith, W. L, Spinhirne, J. D., & Revercomb, H. E. (1990). The 27-28 October 1986 FIRE IFO cirrus case study: Spectral properties of cirrus clouds in the 8-12 μm window. *Monthly Weather Review*, **118,** 2377–2388. https://doi.org/10.1175/1520-0493(1990)118<2377:TOFICC>2.0.CO;2

Baum, B., Kratz, D., Yang, P., Ou, S., Hu, Y., Soulen, P., & Tsay, S. (2000). Remote sensing of cloud properties using MODIS airborne simulator imagery during SUCCESS: 1. Data and models. *Journal of Geophysical Research: Atmospheres*, 105(D9), 11767– 11780. https://doi:10.1029/1999JD901089

Baum, B. A., Menzel, W. P., Frey, R. A., Tobin, D. C., Holz, R. E., Ackerman, S. A., et al., (2012). MODIS cloud-top property refinements for Collection 6. *Journal of Applied Meteorology and Climatology*, 51(6). 1145-1163. https://doi:10.1175/jamc-d-11-0203.1

Baum, B. A., Yang, P., Heymsfield, A. J., Bansemer, A. R., Cole, B. H., Merrelli, A., et al. (2014). Ice cloud single-scattering property models with the full phase matrix at wavelengths from 0.2 to 100 um. *Journal Of Quantitative Spectroscopy & Radiative Transfer*, 146, 123-139. https://doi:10.1016/j.jqsrt.2014.02.029

Berk, A., Anderson, G. P., Acharya, P. K., Bernstein, L. S., Muratov, L., Lee, J., et al. (2005). MODTRAN5: A reformulated atmospheric band model with auxiliary species and practical multiple scattering options. *Proceedings, Multispectral and Hyperspectral Remote Sensing Instruments and Applications II*, 5665. https://doi.org/10.1117/12.578758

Cesana, G., Kay, J. E., Chepfer, H., English, J. M., & de Boer, G. (2012). Ubiquitous low-level liquid-containing Arctic clouds: New observations and climate model constraints from CALIPSO-GOCCP. *Geophysical Research Letters*, 39, L20804. https://doi:10.1029/2012gl053385

Cho, H. M., Nasiri, S. L., & Yang, P. (2009). Application of CALIOP measurements to the evaluation of cloud phase derived from MODIS infrared channels. *Journal of Applied Meteorology and Climatology*, 48(10), 2169-2180. https://doi:10.1175/2009jamc2238.1

Cossich, W., Maestri, T., Magurno, D., Martinazzo, M., Natale, G. D., et al. (2021). Ice and Mixed-Phase Cloud Statistics on Antarctic Plateau. *Atmospheric Chemistry and Physics*, 21, 13811-13833, https://doi.org/10.5194/acp-21-13811-2021.

de Boer, G., Morrison, H., Shupe, M. D., & Hildner, R. (2011) Evidence of liquid dependent ice nucleation in high-latitude stratiform clouds from surface remote sensors, *Geophysical Research Letters,* 38, L01803, doi:10.1029/2010GL046016.

Di Natale, G., Bianchini, G., Del Guasta, M., Ridolfi, M., Maestri, T., et al. (2020). Characterization of the Far Infrared Properties and Radiative Forcing of Antarctic Ice and Water Clouds Exploiting the Spectrometer-LiDAR Synergy. *Remote Sensing*, 12, 3574. https://doi.org/10.3390/rs12213574.

Fu, Q., Liou, K. N., Cribb, M. C., Charlock, T. P., & Grossman, A. (1997). Multiple Scattering Parameterization in Thermal Infrared Radiative Transfer. *Journal of the Atmospheric*

Sciences, 54(24), 2799-2812. https://doi.org/10.1175/1520 0469(1997)054<2799:MSPITI>2.0.CO;2

Garrett, T., & Zhao, C. (2006). Increased Arctic cloud longwave emissivity associated with pollution from mid-latitudes. *Nature,* 440, 787–789. https://doi.org/10.1038/nature04636

Hersbach, H., Bell, B., Berrisford, P., Hirahara, S., Horányi, A., Muñoz-Sabater, J., et al. (2020). The ERA5 global reanalysis. *Quarterly Journal of the Royal Meteorological Society*, 146, 1999–2049. https://doi.org/10.1002/qj.3803

Huang, X. L., Chen, X.H., Zhou, D. K., Liu, X. (2016) An observationally based global band-by-band surface emissivity dataset for climate and weather simulations. *Journal of the Atmospheric Sciences*, 73, 3541-3555, doi:10.1175/JAS-D-15-0355.1

Intrieri, J. M., Fairall, C. W., Shupe, M. D., Persson, P. O. G., Andreas, E. L., Guest, P. S., & Moritz, R. E. (2002). An annual cycle of Arctic surface cloud forcing at SHEBA. *Journal of Geophysical Research: Oceans*, 107(C10), 14. https://doi:10.1029/2000jc000439

Kay, J. E., Bourdages, L., Miller, N. B., Morrison, A., Yettella, V., Chepfer, H., & Eaton, B. (2016). Evaluating and improving cloud phase in the Community Atmosphere Model version 5 using spaceborne lidar observations. *Journal of Geophysical Research: Atmospheres*, 121(8), 4162-4176. https://doi:10.1002/2015jd024699

Kahn, B. H., Irion, F. W., Dang, V. T., Manning, E. M., Nasiri, S. L., Naud, C. M., et al. (2014) The Atmospheric Infrared Sounder version 6 cloud products. *Atmospheric Chemistry and Physics*, 14, 399-426. https://doi.org/10.5194/acp-14-399-2014

Korolev, A., McFarquhar, G., Field, P. R., Franklin, C., Lawson, P., Wang, Z., et al. (2017). Mixed-Phase Clouds: Progress and Challenges, *Meteorological Monographs*, *58*, 5.1-5.50. https://doi.org/10.1175/AMSMONOGRAPHS-D-17-0001.1

Lawson, R., & Gettelman, A. (2014). Impact of Antarctic cloud on climate. *Proceedings of the National Academy of Sciences,* 111 (51) 18156-18161; DOI: 10.1073/pnas.1418197111.

L'Ecuyer, T. S., Drouin, B. J., Anheuser, J., Grames, M., Henderson, D., Huang, X., et al. (2021). The Polar Radiant Energy in the Far InfraRed Experiment: A New Perspective on Polar Longwave Energy Exchanges, *Bulletin of the American Meteorological Society*, 1-46. https://doi.org/10.1175/BAMS-D-20-0155.1

Libois, Q., & Blanchet, J. P. (2017). Added value of far-infrared radiometry for remote sensing of ice clouds. *Journal of Geophysical Research: Atmospheres*, 122(12), 6541-6564. https://doi:10.1002/2016jd026423

Listowski, C., Delanoë, J., Kirchgaessner, A., Lachlan-Cope, T., and King, J. (2019). Antarctic clouds, supercooled liquid water and mixed phase, investigated with DARDAR: geographical and seasonal variations. *Atmospheric Chemistry and Physics*, 19, 6771–6808, https://doi.org/10.5194/acp-19-6771-2019

Listowski, C., & Lachlan-Cope, T. (2017). The microphysics of clouds over the Antarctic Peninsula – Part 2: Modelling aspects within Polar WRF. *Atmospheric Chemistry and Physics,* 17, 10195–10221. https://doi.org/10.5194/acp-17-10195-2017

Lubin, D., & Vogelmann, A. (2006). A climatologically significant aerosol longwave indirect effect in the Arctic. *Nature,* 439, 453–456. https://doi.org/10.1038/nature04449

Maestri, T., Arosio, C., Rizzi, R., Palchetti, L., Bianchini, G., & Del Guasta, M. (2019a). Antarctic ice cloud identification and properties using downwelling spectral radiance from 100 to 1,400 cm^{-1}. *Journal of Geophysical Research: Atmospheres*, 124, 4761– 4781. https://doi.org/10.1029/2018JD029205

Maestri, T., Cossich, W., & Sbrolli, I. (2019b). Cloud identification and classification from high spectral resolution data in the far infrared and 840 mid-infrared. *Atmospheric Measurement Techniques*, 12, 3521–3540, https://doi.org/10.5194/amt-12-3521-2019

Merrelli, A., & Turner, D. D. (2013). Information content for cloud ice microphysics in the FIR radiance spectrum. *AIP Conference Proceedings,* 1531, 348. https://doi.org/10.1063/1.4804778

Morrison, H., de Boer, G., Feingold, G., Harrington J., Shupe, M. D., & Sulia, K., (2012). Resilience of persistent Arctic mixed-phase clouds. *Nature Geoscience*, 5**,** 11–17. https://doi:10.1038/ngeo1332

Palchetti, L., Brindley, H., Bantges, R., Buehler, S. A., Camy-Peyret, C., Carli, B., et al. (2020). FORUM: Unique Far-Infrared Satellite Observations to Better Understand How Earth Radiates Energy to Space. *Bulletin of the American Meteorological Society*, 101(12), E2030-E2046. https://doi.org/10.1175/BAMS-D-19-0322.1

Peterson, C. A., Yue, Q., Kahn, B. H., Fetzer, E., & Huang, X. (2020). Evaluation of AIRS Cloud Phase Classification over the Arctic Ocean against Combined CloudSat–CALIPSO Observations. *Journal of Applied Meteorology and Climatology*, 59(8), 1277-1294. https://doi.org/10.1175/JAMC-D-20-0016.1

Rathke, C., Fischer, J., Neshyba, S., & Shupe, M. (2002). Improving IR cloud phase determination with 20 microns spectral observations. *Geophysical Research Letters*, 29(8). doi:10.1029/2001GL014594

Rossow, W. B., & Schiffer, R. A. (1999). Advances in understanding clouds from ISCCP. *Bulletin of the American Meteorological Society*, 80, 2261–2287. https://doi.org/10.1175/1520-0477(1999)080<2261:AIUCFI>2.0.CO;2

Rowe, P. M., Cox, C. J., & Walden, V. P. (2016). Toward autonomous surface-based infrared remote sensing of polar clouds: cloud-height retrievals. *Atmospheric Measurement Techniques*, 9, 3641–3659, https://doi.org/10.5194/amt-9-3641-2016

Rowe, P. M., Cox, C. J., Neshyba, S., & Walden, V. P. (2019). Toward autonomous surface-based infrared remote sensing of polar clouds: retrievals of cloud optical and microphysical properties. *Atmospheric Measurement Techniques*, 12, 5071–5086, https://doi.org/10.5194/amt-12-5071-2019

Saito, M., Yang, P., Huang, X., Brindley, H. E., Mlynczak, M. G., & Kahn, B. H. (2020). Spaceborne middle- and far-infrared observations improving nighttime ice cloud property retrievals. *Geophysical Research Letters*, 47, e2020GL087491. https://doi.org/10.1029/2020GL087491

Scott, R. C., Lubin, D., Vogelmann, A. M., & Kato, S. (2017). West Antarctic ice sheet cloud cover and surface radiation budget from NASA A-Train satellites. *Journal of Climate*, 30(16), 6151-6170. https://doi.org/10.1175/JCLI-D-16-0644.1

Sgheri, L., Belotti, C., Ben-Yami, M., Bianchini, G., Carnicero Dominguez, B., et al. (2021). The FORUM End-to-End Simulator project: architecture and results. *Atmospheric Measurement Techniques Discussion*, [preprint], https://doi.org/10.5194/amt-2021-196, in review.

Shupe, M. D. (2011). Clouds at Arctic atmospheric observatories. Part ii: Thermodynamic phase characteristics. *Journal of Applied Meteorology and Climatology*, 50(3), 645-661. https://doi:10.1175/2010jamc2468.1

Shupe, M. D., & Intrieri, J. M., (2004). Cloud radiative forcing of the Arctic surface: The influence of cloud properties, surface albedo, and solar zenith angle. *Journal of Climate*, 17(3), 616-628. https://doi:10.1175/1520-0442(2004)017<0616:crfota>2.0.co;2

Stamnes, K., Tsay SC., Wiscombe, W., & Jayaweera, K. (1988). Numerically stable algorithm for discrete-ordinate-method radiative transfer in multiple scattering and emitting layered media. *Applied Optics,* 27(12), 2502–2509. https://doi.org/10.1364/AO.27.002502

Strabala, K. I., Ackerman, S. A., & Menzel, W. P. (1994). Cloud Properties inferred from 8–12-µm Data. *Journal of Applied Meteorology and Climatology*, *33*(2), 212-229. https://doi.org/10.1175/1520-0450(1994)033<0212:CPIFD>2.0.CO;2

Turner, D. D. (2005). Arctic Mixed-Phase Cloud Properties from AERI Lidar Observations: Algorithm and Results from SHEBA. *Journal of Applied Meteorology*, *44*(4), 427-444. https://doi.org/10.1175/JAM2208.1

Turner, D. D., Ackerman, S. A., Baum, B. A., Revercomb, H. E., & Yang, P. (2003). Cloud phase determination using ground-based AERI observations at SHEBA. *Journal of Applied Meteorology*, 42(6), 701-715. https://doi.org/10.1175/1520-0450(2003)042<0701:CPDUGA>2.0.CO;2

Vergara-Temprado, J., Miltenberger, A. K., Furtado, K., Grosvenor, D. P., Shipway, B. J., Hill, A. A., et al. (2018). Strong control of Southern Ocean cloud reflectivity by ice-nucleating particles. *Proceedings of the National Academy of Sciences of the United States of America*, 115(11), 2687–2692. https://doi.org/10.1073/pnas.1721627115

Verlinde, J., Harrington, J. Y., McFarquhar, G. M., Yannuzzi, V. T., Avramov, A., Greenberg, S., et al. (2007). The Mixed-Phase Arctic Cloud Experiment, Bulletin of the American Meteorological Society, 88(2), 205-222. https://doi.org/10.1175/BAMS-88-2-205

Yang, P., Bi, L., Baum, B. A., Liou, K., Kattawar, G. W., Mishchenko, M. I., & Cole, B. (2013). Spectrally consistent scattering, absorption, and polarization properties of atmospheric ice crystals at wavelengths from 0.2 to 100 µm. *Journal of the Atmospheric Sciences*, 70(1), 330-347. https://doi.org/10.1175/JAS-D-12-039.1

Yang, P., Mlynczak, M.G., Wei, H., Kratz, D.P., Baum, B.A., Hu, Y.X., et al. (2003). Spectral signature of ice clouds in the far-infrared region: Single-scattering calculations and radiative sensitivity study. *Journal of Geophysical Physics,* 108, 4569. https://doi:10.1029/2002JD003291

Appendix

The middle and right panels of Figure 4.4 show that, for different cloud optical depths, the TOA upwelling radiance has varying dependence on the single scattering albedo (ω). Here we use analytical solutions of the two-stream approximation to illustrate the physics of this dependence. The two-stream solution follows Fu et al. (1997), which assumes only one upwelling stream and one downwelling stream and takes thermal emission into account.

In Figure 4.A1, at a given frequency, the cloud has optical depth τ, single scattering albedo ω, asymmetry factor g, and blackbody radiation $B(0)$ and $B(\tau)$ at its top and bottom boundaries, respectively. No gaseous absorption is considered here. Based on Fu et al. (1997), the upwelling radiance at the cloud upper boundary can be expressed as

$$I^{\uparrow}(0) = g_1 e^{-k\tau} + g_2 R + Z_+(0) \quad , \qquad \text{(A1)}$$

where

$$k = (r_1^2 - r_2^2)^{\frac{1}{2}} = D\sqrt{(1 - \omega g)(1 - \omega)},$$

$$R = \frac{r_1 - k}{r_2},$$

$$Z_{\pm}(\tau) = \frac{D(1 - \omega)B(\tau)}{k^2 - \beta^2}(r_1 \pm \beta + r_2),$$

$$r_1 = D\left[1 - \frac{\omega}{2}(1 + g)\right],$$

$$r_2 = D\frac{\omega}{2}(1 - g),$$

$$\beta = \frac{1}{\tau} ln\left[\frac{B(\tau)}{B(0)}\right],$$

and $D = 1.66$ is the diffusive factor.

Assume no downwelling radiance at the cloud top, a reasonable approximation for 449 cm^{-1} and a cloud top at 300 hPa, and assume that the upwelling radiance at the lower boundary is unity, so all radiance is normalized with respect to the upwelling radiance at the lower boundary. Then coefficients g_1 and g_2 can be decided by the boundary conditions as follows:

$$I^{\downarrow}(0) = g_1 R e^{-k\tau} + g_2 + Z_-(0) = 0, \qquad (A2)$$

$$I^{\uparrow}(\tau) = g_1 + g_2 R e^{-k\tau} + Z_+(\tau) = 1, \qquad (A3)$$

which yields

$$g_1 = \frac{[1-Z_+(\tau)] - Z_-(0)Re^{-k\tau}}{1 - R^2 e^{-2k\tau}}, \qquad (A4)$$

$$g_2 = -\frac{Z_-(0) + [1-Z_+(\tau)]Re^{-k\tau}}{1 - R^2 e^{-2k\tau}}. \qquad (A5)$$

On the right-hand-side of Equation A1, the first term, $g_1 e^{-k\tau}$, is related to the upwelling stream in the two-stream approximation; the second term, $g_2 R$, is related to the reflection of the downwelling stream; the third term, $Z_+(0)$, is related to thermal emissions within the cloud layer. Based on the definitions of k and R, it is easy to show that $\partial k / \partial \omega < 0$ and $\partial R / \partial \omega > 0$. As shown in Figure A2, when $\omega = 0$ (pure absorption with no scattering), $k = D$ and $R = 0$; when $\omega \rightarrow 1$, $k \rightarrow 0$ and $R \rightarrow 1$. Neither k nor R is a function of optical depth, but coefficients g_1 and g_2 are both a function of optical depth, as in Equations A4 and A5. Moreover, as long as the blackbody radiation at the cloud lower boundary is less than the upwelling radiance enter the lower boundary (which is the case of our study), $[1 - Z_+(\tau)] < 0$ and thus g_2 is always negative.

To mimic the 449 cm^{-1} case shown in Figure 4.4, let g=0.75, B(0) = 0.65 and B(τ) = 0.7, while the upwelling radiance at the lower boundary is normalized to unity. Figure A3 shows how the terms vary when ω increases from 0.01 to 0.95. The results are shown for an opaque case (τ=10) and a non-opaque case (τ=1). As $\partial k/\partial \omega$<0, the first term $g_1 e^{-k\tau}$ always increases with ω. However, given e^{-10} ~ 0 and e^{-10}«e^{-1}, the rate of increase, $\partial[g_1 e^{-k\tau}]/\partial \omega$, is much larger for the non-opaque case than for the opaque case. As shown in Figure A3a, for τ=10, the first term remains almost flat until ω reaches 0.8, when $k = 0.47$ so the rate of increase starts to be visible. For a non-opaque case, the increase of the first term with ω is always visibly noticeable in Figure A3a.

Because g_2 is negative and $\partial R/\partial \omega$ is positive, the second term $g_2 R$ decreases when ω increases, shown in Figure A3b. For the parameters used here, the rate of decrease is almost the same for both cases. For the opaque case, in-layer emission that can reach the upper boundary essentially originates just below the upper boundary. Emissions from farther below this top sublayer have little chance to reach the upper boundary due to the cloud opacity. That is why the third term $Z_+(0)$ for the opaque case (red curve in Figure 4.A3c) is essentially flat and only slightly above the B(0)=0.65 line. The red curve still increases with ω, but the rate of increase $\partial Z_+(0)/\partial \omega$ is ~9×10^{-5}. For the non-opaque case, in-cloud thermal emissions can reach the upper boundary, especially with larger ω (or smaller absorption optical depth), as shown in Figure A3c. A salient point here is that $Z_+(0)$ contains factor $1/(k^2-\beta^2)$. Note that $\beta(\tau=1) > \beta(\tau=10)$, which also contributes to a larger $Z_+(0)$ for the non-opaque case than for the opaque case.

Taking all three terms into account (Figure 4.A3d), for the non-opaque case the first and third terms increase noticeably with ω, and together they dominate over the decrease of the second term with ω, so I$^{\uparrow}$(0) increases with ω. For the opaque case, the first and third terms increase little

with ω, so the change of the second term dominates and $I^{\uparrow}(0)$ decreases with ω. These results are consistent with Figure 4, which is based on a more accurate 8-stream DISORT solver.

A physical interpretation of the above analytical solution is summarized as follows. The upwelling radiance at the top of a cloud, $I^{\uparrow}(0)$, has three components, reflection of downwelling radiance through the clouds, attenuated upwelling radiance entering the cloud lower boundary, and in-cloud thermal emission reaching the upper boundary. For the parameter regimes studied here, the decrease of reflection of downwelling radiation with increasing ω is largely similar between opaque and non-opaque cases. However, the other two components increase with ω and the rate of increase slows down as the optical depth becomes larger. As a result, $I^{\uparrow}(0)$ shows different dependence on ω for the non-opaque and opaque cases.

This interpretation also highlights the importance of multiple scattering for the opaque case, as the reflection of downwelling radiance is the key process in multiple scattering, which cannot be represented by the single-scattering approximation or absorption approximation methods (e.g., Fu et al., 1997 and Chou et al. 1999.
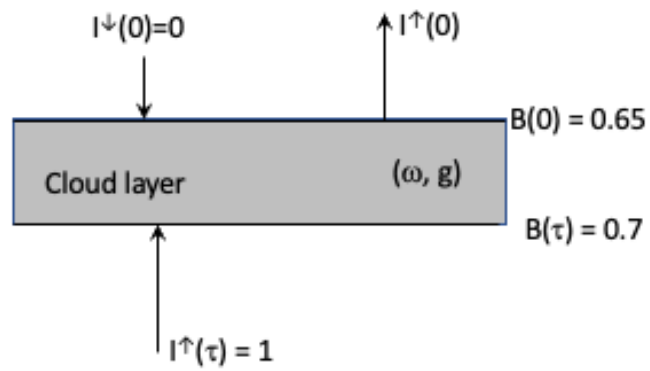
Figure 4.A1. Sketch of the two-stream approximation for the multiple scattering problem discussed here. Only a cloud is considered here and no gaseous absorptions. The extinction optical depth of the cloud is τ. The blackbody emissions at cloud upper and lower boundaries are $B(0)$ and $B(\tau)$, respectively. All radiances are normalized with respect to the upwelling radiance entering the lower boundary.
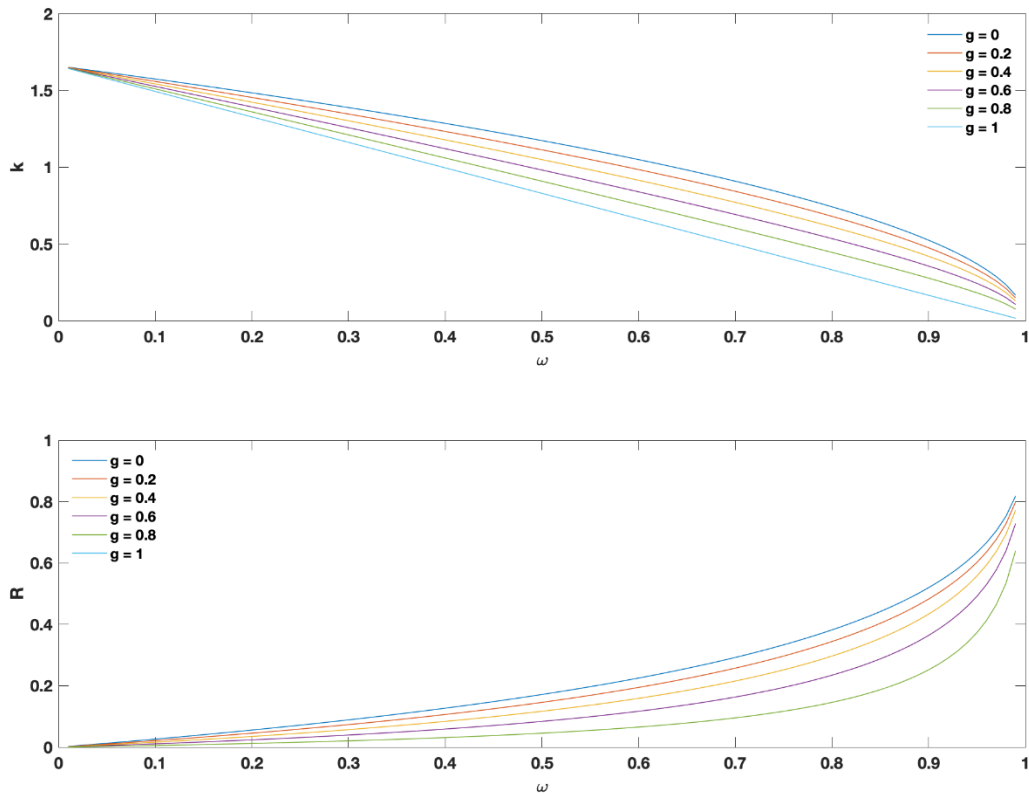
Figure 4.A2. Upper panel: k as a function of ω, different color lines correspond to different values of g as labeled. Lower panel: Same as the upper panel but for R as a function of ω. k and R are defined in the appendix.
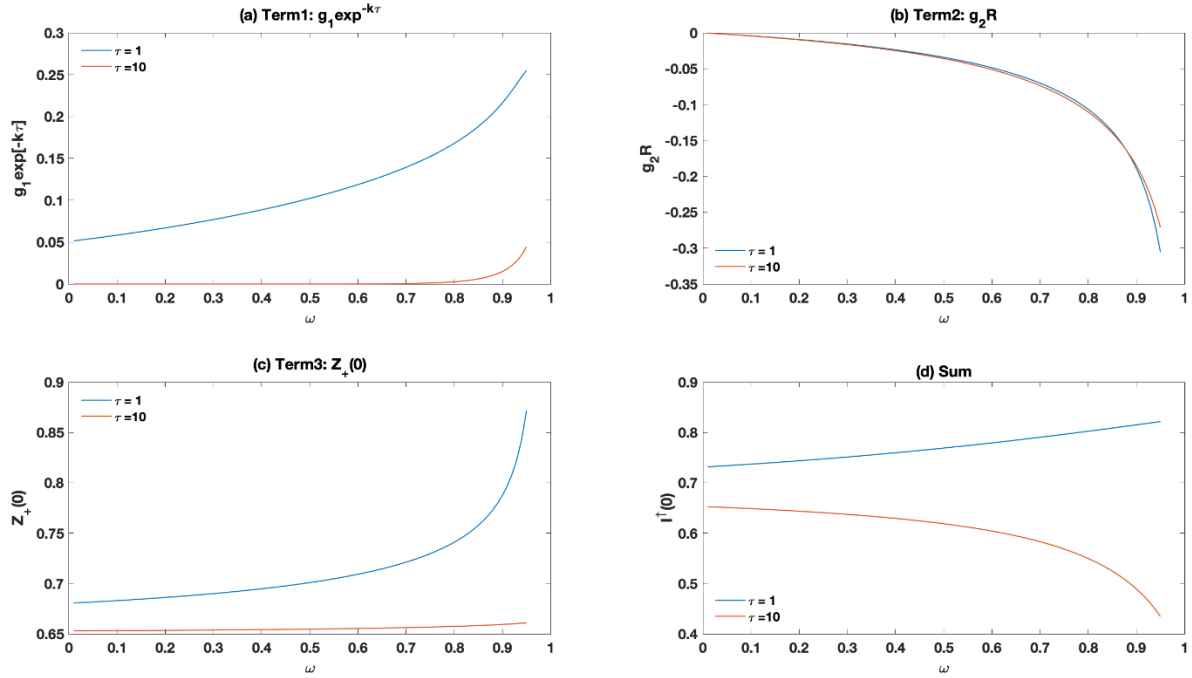
Figure 4.A3. (a) The first term at the right-hand side of Equation A1 as a function of ω for two cases, τ=1 (blue line) and τ=10 (red line). (b)-(c) Same as (a) but for the second and third terms at the right-hand side of Equation A1, respectively. (d) Variation of the upwelling radiance at the upper boundary (the summation of three terms shown in (a)-(c)) with ω for τ=1 and τ=10. For all calculations, $g = 0.75$, blackbody radiation at upper boundary is 0.65 and at the lower boundary is 0.7. The upwelling radiance at the lower boundary is set to be 1 and the downwelling radiance at the upper boundary is zero.

Chapter 5 Sensitivity of Infrared Brightness Temperature to Precipitating Ice Layer of Liquid-Topped Mixed Phase Clouds

5.1 Introduction

Clouds are important contributors to the Arctic surface energy budget and warm the surface throughout much of the year through longwave (LW) emission. Liquid-containing clouds tend to be more optically thick compared to ice-only clouds and correspond to "radiatively opaque" scenes in which the net LW radiative flux at the surface is nearly balanced in the upwelling and downwelling directions (Cesana et al., 2012). Mixed phase clouds are common in the Arctic across the entire region and throughout the entire year, as liquid cloud droplets be in a supercooled state for temperatures as low as -40°C (Shupe, 2011). Typically, when cloud ice and liquid water are coexisting and interacting, the lower saturation vapor pressure of ice tends to result in the amount of ice growing at the expense of liquid. This is referred to as the Wegener-Bergeron-Findeisen process (WBF; Bergeron, 1935; Findeisen, 1938; Wegener, 1911). However, mixed phase clouds in the Arctic can exist for tens of hours (Verlinde et al., 2007; Shupe et al., 2011), much longer than expected based on the WBF process alone. Commonly, mixed phase clouds take the form of a stratiform layer of supercooled liquid water with ice precipitation below and are maintained by a complex web of microphysical and dynamical processes that are not fully understood (Morrison et al., 2012). In this study, such clouds are called liquid-topped mixed phase clouds (LTMs) and are present in the Arctic anywhere from 4 % to 26% of the time depending on season and location (de Boer et al, 2011; Morrison et al., 2012).

Arctic LTMs are not well represented in climate models or even cloud resolving models (Klein et al., 2009; McCoy et al., 2016). Such a misrepresentation of clouds can lead to radiative flux biases in climate models (e.g., Cesana et al., 2012; Cho et al., 2020). Given the remoteness of the Arctic region, satellite observations are crucial for understanding the large-scale distribution and radiative impacts of LTMs. One of the most reliable ways of detecting LTMs from space is by using active sensors. Notably, the CALIPSO lidar and CloudSat radar can be used together to detect the presence of both ice and liquid simultaneously (Sassen, 2008) along vertical curtains that transect a region during an overpass. This vertically curtain can resolve LTM features but lacks horizontal spatial information. Passive infrared (IR) imagers have much larger fields of view and can be used during the entire Arctic year in contrast with shortwave imagers. However, IR imagers are most sensitive to the cloud top, which in the case of LTMs is liquid water. Thus, any cloud phase determination with the IR would be weighted towards liquid. Typically, cloud phase determination with the IR consists of taking the difference in brightness temperature between two spectral channels in the mid-IR window (~800-1250 cm^{-1}), the spectral region used for the MODIS and AIRS cloud phase algorithms. The physical basis is that the absorption and scattering properties can vary across the mid-IR window for both liquid and ice water.

This dissertation, and other studies (e.g., Kahn et al., 2014), have shown that the mid-IR cloud phase determination is more accurate for determining ice phase compared to liquid. Thus, it may be possible for the mid-IR to be used for detection the underlying ice layer of a LTM, which is henceforth referred to as LTM$_{ice}$. The liquid layer is referred to as LTM$_{liq}$.

The purpose of this study is to develop parameter space manifolds for the detection of changes in LTM$_{ice}$ using the brightness temperature at the mid-IR window channel of 11 µm (BT$_{11}$), which a common metric used for the detection of clouds with satellite observations. The

parameters of interest are mainly the liquid and ice water paths (LWP and IWP, respectively) of the LTM_{liq} and LTM_{ice}, respectively. The LWP and IWP represent the vertical integration of liquid and ice cloud water concentration, respectively. The sensitivity of BT_{11} to changes in the IWP of the LTM_{ice}, which will be henceforth referred to as $\frac{d(BT_{11})}{d(IWP)}$), is the metric used in this study to determine if BT_{11} is sensitive to changes in the LTM_{ice}. The development of LWP-IWP manifolds in which $\frac{d(BT_{11})}{d(IWP)}$ is sufficiently large is thus a major goal of this study. Other parameters considered include surface, and atmospheric variables such as tropospheric temperature structure and surface temperature as well as cloud-top-pressure (CTP)

The BT_{11} can be dependent on the absorption and scattering properties of both LTM_{liq} and LTM_{ice}. For example, as the LTM_{liq} LWP approaches infinity, changes in the LTM_{ice} will have less of an effect on BT_{11} and thus $\frac{d(BT_{11})}{d(IWP)}$ would approach zero. Similarly, increasing the IWP of the LTM_{ice} would eventually lead to the LTM_{ice} radiating like a blackbody and $\frac{d(BT_{11})}{d\,(IWP)}$ approaching zero if only absorption and emission are considered. However, because the ice cloud single scattering albedo (SSA_{ice}) can be as large as ~0.5 based on the cloud optical properties used in this study, it is possible that, like what was shown in Chapter 4, for the far-IR, ice cloud scattering can have a significant impact on BT_{11} and the scattering effects can change with IWP. Furthermore, it is possible that different atmospheric and surface conditions could impact $\frac{d(BT_{11})}{d(IWP)}$ and thus this study uses a range of Arctic scene types when determining $\frac{d(BT_{11})}{d(IWP)}$.

Section 5.2 discusses the reanalysis data and radiative transfer simulations used in this study. Section 5.3 presents a simple analytical model for determining the first order factors that

influence $\frac{d(BT_{11})}{d(IWP)}$. Section 5.4 presents the results from radiative transfer simulations. Section 5.5 provides discussion and conclusions.

5.2 Data and Methods

5.2.1 ERA5 Reanalysis Data and Scene Types

ECMWF ERA5 data is used to generate the synthetic radiances in this study. Data over the Arctic (60-90°N), for the year of 2003 and the months of January through August are used. These months effectively capture the Arctic winter, spring, and summer seasons. September through December are not used because the continuation of the study utilizes ground-based cloud observations that are unavailable for those four months. The ERA5 data are hourly and are provided with a horizontal spatial resolution 0.25°x0.25°. The data fields used are surface skin temperature (T_s), surface pressure (P_s), and vertical profiles of specific humidity (q) and temperature (T_{atm}). Vertical profiles in ERA5 are provided at 37 fixed pressure levels from 1000 hPa to 1 hPa. The altitudes of these pressure levels are calculated using the hydrostatic approximation.

To understand how $\frac{d(BT_{11})}{d(IWP)}$ is influenced by tropospheric and surface conditions, radiances are generated for a set of ERA5 scene types based on T_s, the atmospheric temperature difference between 1000 hPa and 750 hPa (ΔT), and total column water vapor (TCWV). The TCWV is computed from the profiles of q and T_{atm}. The different ERA5 scenes represent a wide and nearly continuous range of Arctic environmental conditions during the period of this study. The ERA5
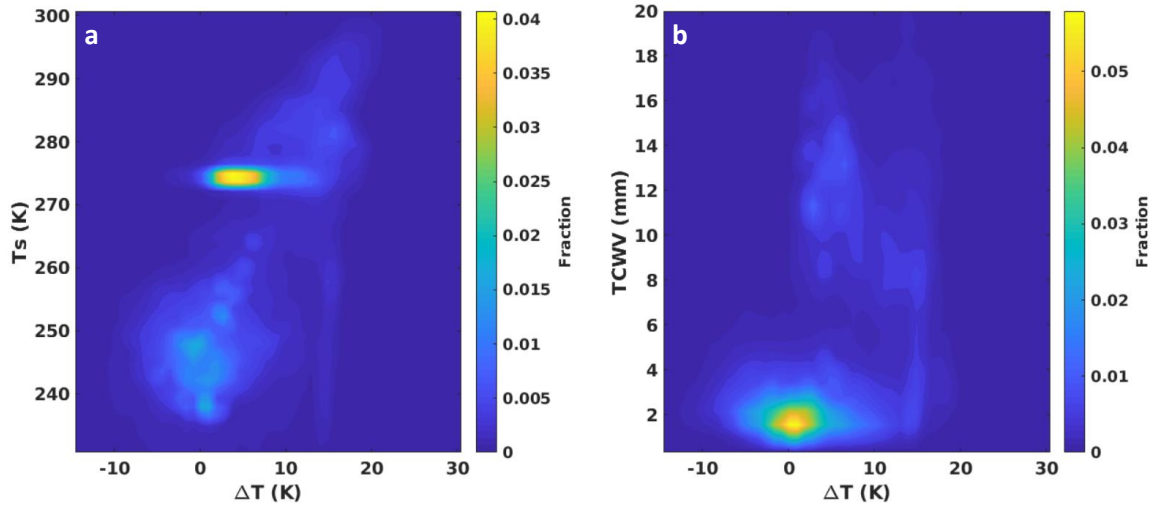
Figure 5.1. Joint histograms of (a) T_s and ΔT and (b) TCWV and ΔT from ERA5 data over the Arctic (60-90°N) for the months of January, March, and July 2003. The color scale represents the fraction of total cases which is ~73,000.

scene types are specified as discrete intervals of Ts, ΔT, and TCWV. The T_s intervals are as follows: (1) $T_s< 245$ K, (2) 245 K $< T_s < 255$ K, (3) 255 K $< T_s < 265$ K, (4) 265 K $< T_s < 285$ K and (5) $T_s > 285$ K. The ΔT intervals are (1) $\Delta T < -5$ K, (2) -5 K $< \Delta T < 0$ K, (3) 0 K $< \Delta T < 5$ K and (4) $\Delta T > 5$ K. The TCWV intervals are (1) TCWV < 5 mm, (2) 5 mm $<$ TCWV < 10 mm, (3) 10 mm $<$ TCWV < 15 mm and (4) TCWV > 15 mm. Figure 5.1 shows joint histograms from which these scene types are based. The number of discrete joint intervals (i.e., scene types) of Ts, ΔT, and TCWV is 80, but only 57 were found in the 8-month ERA5 dataset. The 23 missing scene

types represent less likely combinations of T_s, ΔT, and TCWV, such as very cold conditions (T_s<245 K) having TCWV>15mm (not shown).

5.2.2 Radiative Transfer Simulations of LTMs for the ERA5 Scenes

Synthetic spectral radiances are generated by inputting ECMWF ERA5 reanalysis data and prescribed cloud properties into MODerate Resolution Atmospheric TRANsmission Version 5 (MODTRAN5; Berk at al., 2005), a widely used radiative transfer model. Radiances are generated at 1 cm^{-1} spectral resolution at a channel center of 11 µm.

The ice bulk absorption and scattering models from Baum et al. (2014) are used in ice cloud radiance calculations, just as for Chapter 4. In brief, these models are based on the ice particle single scattering property database developed by Yang et al. (2013) and the general habit mixture from (Baum et al., 2014). The bulk ice COP models at a given wavelength are developed by integrating over in-situ single scattering properties of individual habit and particle size distributions (assumed to be gamma distribution for ice) and averaging them across 14,000 flights. Figure 4.1 shows five COPs: Bulk absorption efficiency (Q_{abs}), scattering efficiency (Q_{scat}), extinction efficiency (Q_{ext}), single scattering albedo (SSA), and scattering asymmetry factor (*g*). COPs are provided at wavelengths from 3 to 99 µm and for effective ice particle diameters (D_{eff_ice}) ranging from 10 to 180 µm at 5 µm increments. These ice COPs are linearly interpolated to the spectral channels in our simulations. Each simulation is performed for D_{eff_ice} values of 20 and 60 µm. The liquid droplet effective diameter (D_{eff_liq}) is fixed at 20 µm and Mie scattering is used to derive the COPs for all liquid clouds.

Cloud properties are manually prescribed in the exact same way for all ERA5 scenes in the radiance simulations. To produce an LTM within a ERA5 scene in MODTRAN5, a single liquid

cloud layer is "stacked" onto a single ice cloud layer in the simulation (i.e., the CTP the ice layer is equal to the cloud bottom pressure of the liquid layer). The cloud top and bottom pressure levels of each cloud layer are equivalent to the geometric boundaries of the cloud in which there is non-zero cloud water content. Liquid water content and ice water content are prescribed to be vertically homogenous and consistent with the prescribed LWP and IWP. In reality, there can be changes in cloud particle sizes with height, but the homogenous assumption is adequate for the purposes of this study. For each ERA5 scene, the CTPs of an LTM with any given properties will be set such that the CTPs are consistent with the three CTP categories (50-440 hPa, 440-680 hPa, and >680 hPa) defined in the International Satellite Cloud Climatology Project (ISCCP; Rossow & Schiffer, 1999). In this study, the CTP of the liquid (ice) layer is 825 (850), 550 (600) and 300 (350) hPa to be within the low-, mid- and high-level categories, respectively.

5.3 Results

5.3.1 Analytical Model of $\frac{d(R_{TOA,v})}{d(IWP)}$ for an Idealized SMC

To understand the first order factors that influence $\frac{d(BT_{11})}{d(IWP)}$, an analytical model based on a simple two-layer atmosphere can be implemented. Figure 5.2 shows a schematic of an LTM. No gaseous absorption or emission is included in this simple model, and scattering by the cloud is not accounted for, only cloud absorption and emission. Assuming that the temperature of each cloud layer is vertically uniform, the upwelling radiance at a frequency v at the TOA can be expressed

as equation 5.1. Here $B_v(T_s)$, $B_v(T_{ice})$, and $B_v(T_{liq})$ represent the Planck emission from the surface, ice cloud, and liquid cloud layer, respectively.
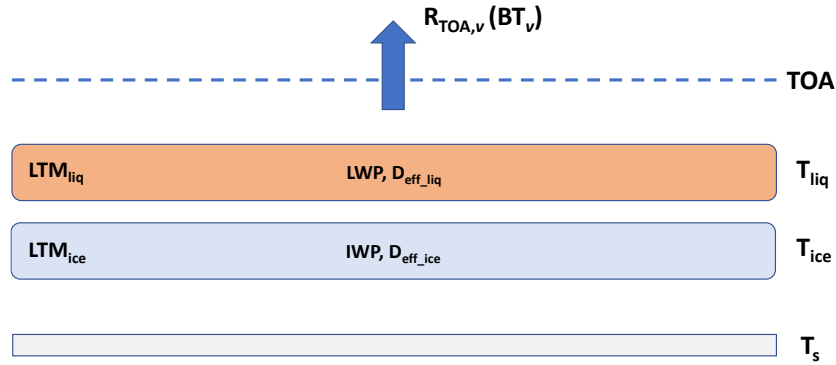
Figure 5.2. Schematic of liquid-topped mixed phase cloud (LTM). The upper cloud layer is composed of liquid cloud water having a liquid water path (LWP) and droplet effective diameter (D_{eff_liq}), while the lower layer is ice water having an ice water path (IWP) and effective diameter (D_{eff_ice}). The temperature of the surface (T_s), ice cloud layer (T_{ice}), and liquid cloud layer (T_{liq}) are labeled. $R_{TOA,v}$ (BT_v) represents the upwelling radiance (brightness temperature) as observed from the top-of-the-atmosphere (dashed line) at frequency v.

$$R_{TOA,v} = [B_v(T_s)\, e^{-\tau_{ice,v}} + (1 - e^{-\tau_{ice,v}})\, B_v(T_{ice})]\, e^{-\tau_{liq,v}} + (1 - e^{-\tau_{liq,v}})\, B_v(T_{liq}) \qquad (eq.\ 5.1)$$

The optical depth of the ice (liquid) layer at frequency v is represented by $\tau_{ice,v}$ ($\tau_{liq,v}$) and can be equated to the product of the IWP (LWP) and the absorption mass cross section, $k_{abs,ice,v}$ ($k_{abs,liq,v}$) (see equations 5.2 & 5.3). The $k_{abs,ice,v}$ and $k_{abs,liq,v}$ used in this model is based on the bulk ice and liquid cloud absorption efficiency data from Yang et al. (2013) and Baum et al. (2014), and is dependent on v and particle effective diameter of ice (D_{eff_ice}) and liquid (D_{eff_liq}) cloud.

$$\tau_{ice,v} = IWP * k_{abs,ice,v} \quad (eq.\ 5.2)$$

$$\tau_{liq,v} = LWP * k_{abs,liq,v} \quad (eq.\ 5.3)$$

Equation 5.1 can be differentiated with respect to IWP to obtain

$$\frac{d(R_{TOA,v})}{d(IWP)} = e^{-\tau_{liq,v} - \tau_{ice,v}}(k_{abs,ice,v})\,[B_v(T_{ice}) - B_v(T_s)] \qquad (eq.\ 5.4)$$

Thus we can expect the sensitivity of $R_{TOA,11}$ (proportional to BT_{11}) to the IWP of the LTM_{ice} to depend on the temperature difference between the LTM_{ice} and the surface (T_s-T_{ice}), the combined optical depths of both LTM cloud layers, and $k_{abs,ice}$ (and thus D_{eff_ice}). Figures 5.3a-d show the results of calculating $\frac{d(R_{TOA,11})}{d(IWP)}$ with varying IWP, LWP, D_{eff_ice}, and T_s-T_{ice} using equation 5.4. For the case with 20 µm D_{eff_ice} and T_s-T_{ice} being 10 K (Figure 5.3a), $\frac{d(R_{TOA,11})}{d(IWP)}$ is negative and largest
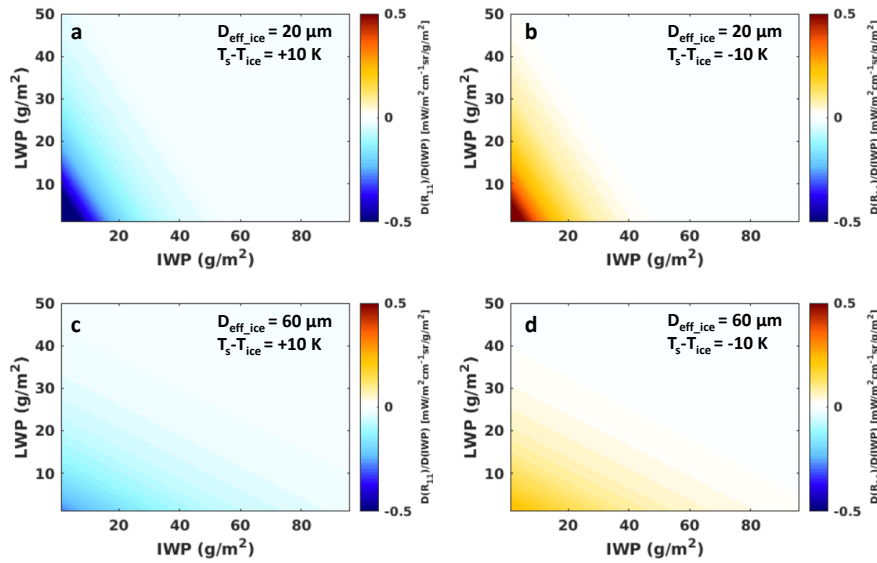
Figure 5.3. The change of top-of-atmosphere upwelling radiance at 11 µm ($R_{TOA,v}$) with respect to ice water path (IWP) as a function of IWP and liquid water path (LWP) calculated using equation 5.4 for (a) 20 µm ice particle effective diameter (D_{eff_ice}) and a difference of 10 K between the surface and the LTM ice layer (LTM_{ice}) temperature (T_s-T_{ice}). (b) same as (a) except T_s-T_{ice} = - 10 K (c) same as (a) but D_{eff_ice} = 60 µm (d) same as (a) except D_{eff_ice} = 60 µm and T_s-T_{ice} = - 10 K.

when both LWP and IWP are less than ~20 g/m^2 and decreases to zero when IWP is >~40 g/m^2. Not surprisingly, when the LTM_{ice} is warmer than the surface (Figure 5.3b), which could be the case if the LTM was within an Arctic temperature inversion, the situation is opposite for the same D_{eff_ice}; $\frac{d(R_{TOA,11})}{d(IWP)}$ is always positive or zero. This is because increasing IWP increases the emissivity of the LTM_{ice}, which increases emission to space if the LTM_{ice} is warmer than the surface. The effect of the LTM_{ice} emissivity increase saturates when IWP is large enough (>~40 g/m^2) or is masked by the overlying liquid layer when LWP becomes greater than ~20 g/m^2. When

the D_{eff_ice} is increased to 60 µm (Figure 5c,d), the sign of $\frac{d(R_{TOA,11})}{d(IWP)}$ is the same as for the smaller

particle size, but the area of the nonzero $\frac{d(R_{TOA,11})}{d(IWP)}$ shifts to lower and higher LWP and IWP,

respectively. This is because, for the same IWP, increasing the D_{eff_ice} decreases the optical depth

of the cloud which causes the $\frac{d(R_{TOA,11})}{d(IWP)}$ to be nonzero for larger IWPs.

This analytical model illustrates the relationship between $R_{TOA,11}$ (and thus BT_{11}), IWP,

LWP, D_{eff_ice}, and T_s-T_{ice}. The model also shows that $\frac{d(R_{TOA,11})}{d(IWP)}$ can be nonzero for LWPs and

IWPs<~40 g/m^2.

5.3.2 Influence of Cloud Properties and ERA5 Scene Types on $\frac{d(BT_{11})}{d(IWP)}$

This section focuses on the impacts of cloud properties and ERA5 scene type parameters

(T_s, ΔT, TCWV) on MODTRAN5 simulations of $\frac{d(BT_{11})}{d(IWP)}$. Note that these simulations include

gaseous absorption and emission, as well as cloud scattering. It was found that ΔT had a much

larger impact on $\frac{d(BT_{11})}{d(IWP)}$ compared to TCWV and T_s (not shown). Note that the ΔT corresponds to

T_s-T_{ice} when LTM$_{ice}$ has a CTP greater than 750 hPa. To account for the latter two scene variables,

the $\frac{d(BT_{11})}{d(IWP)}$ values as a function of LWP, IWP, CTP and D_{eff_ice} were averaged across all scenes that

fell into the same ΔT interval (9 to 13 different TCWV and T_s scenes per ΔT interval depending

on ΔT). A $\frac{d(BT_{11})}{d(IWP)}$ threshold of 0.1 K/g/m^2 was chosen to determine if the BT_{11} was sufficiently

sensitive the LTM$_{ice}$ IWP changes, as an IWP increase of 10 g/m^2 would result in at least a 1 K

BT_{11} increase.

Figure 5.4 shows $\frac{d(BT_{11})}{d(IWP)}$ as a function of IWP and LWP for the 20 µm D_{eff_ice} case and for

the different CTP categories and ΔT intervals. Figure 5.5 shows the same but for the 60 µm D_{eff_ice}

case. The dotted contours show where the $\frac{d(BT_{11})}{d(IWP)}$ threshold is exceeded. A few points are notable:

(1) For the 20 µm D_{eff_ice} high cloud cases (Figure 5.4a-d), not surprisingly, ΔT does not play a

large role in the $\frac{d(BT_{11})}{d(IWP)}$. The differences seen are simply due to T_s-T_{ice} being different for each ΔT

interval (not shown). These high cloud cases show a similar $\frac{d(BT_{11})}{d(IWP)}$ pattern to what was shown

Figure 5.3a, including the fact that $\frac{d(BT_{11})}{d(IWP)}$ tends to be the most negative for IWP and LWP less
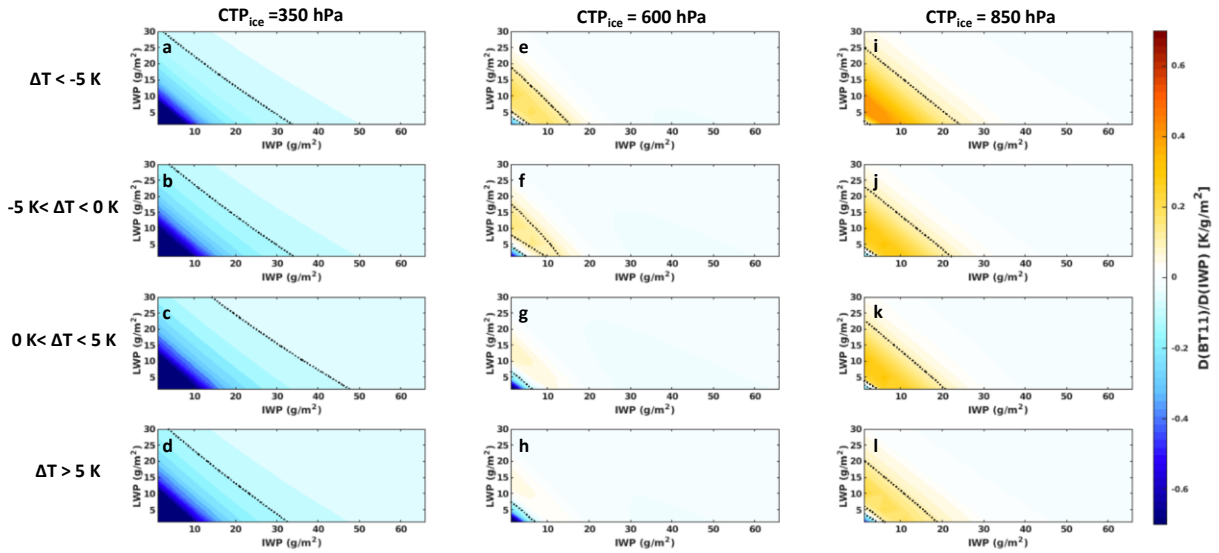
Figure 5.4. (a-d) The gradient of BT$_{11}$ with respect to IWP averaged across all the TCWV and T$_s$ ERA5 intervals for each ΔT interval and for high cloud levels. The dotted lines contain the regions where $\frac{d(BT_{11})}{d(IWP)} > 0.1$ K. Here $D_{eff\_ice} = 20$ µm and $D_{eff\_liq} = 20$ µm (e-h) same as (a-d) except for mid-level clouds (i-l) same as (a-d) expect for low level clouds.

than ~20 g/m². For the 60 µm D_{eff_ice} high cloud cases (Fig. 5.5 a-d), the $\frac{d(BT_{11})}{d(IWP)}$ pattern and

magnitude is like that of the same cases where $D_{eff\_ice} = 20$ µm. However, like what is qualitatively

shown in the Figures 5.3b and 5.3a, increasing the ice particle size shifts the area of the nonzero

$\frac{d(BT_{11})}{d(IWP)}$ to lower and higher LWP and IWP, respectively.

(2) For both D_{eff_ice} cases, low clouds within temperature inversions (Figures 5.4i,j and 5.5i,j) can have positive $\frac{d(BT_{11})}{d(IWP)}$, which is consistent with Figure 5.3.

(4) For the mid and low-level clouds, for all ΔT intervals, and for both D_{eff_ice} cases, both a positive and negative $\frac{d(BT_{11})}{d(IWP)}$ region at higher and lower IWPs, respectively, become noticeable. Figure 5.3
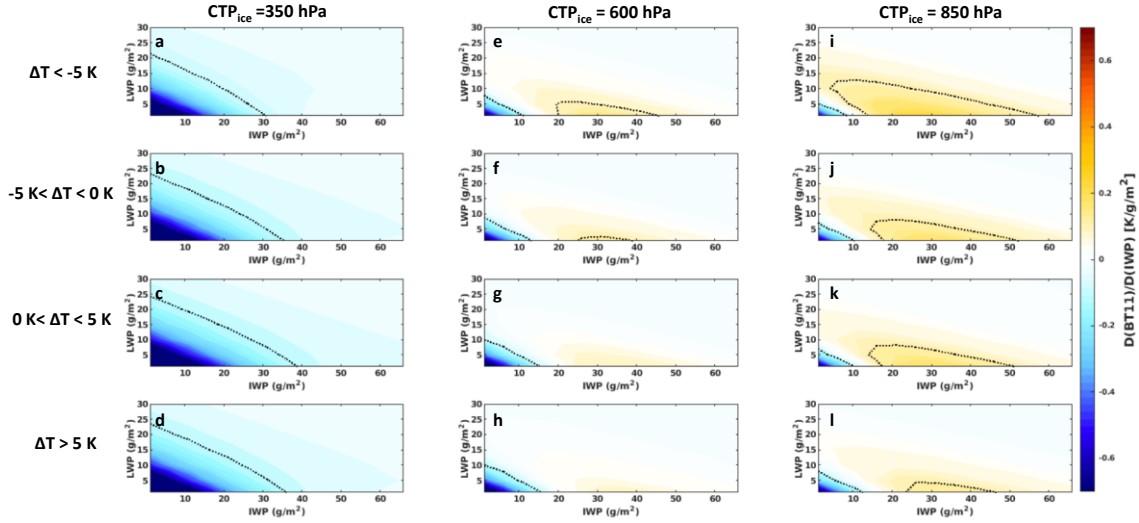
Figure 5.5. Same as Figure 5.4 but D_{eff_ice} = 60 µm.

shows that, for a case where the LTM_{ice} is warmer than the surface, $\frac{d(BT_{11})}{d(IWP)}$ is always non-negative

when scattering is ignored. The fact that $\frac{d(BT_{11})}{d(IWP)}$ can be both positive and negative for these cases

indicates that absorption and emission cannot alone explain it. Thus, scattering must be playing a

role. To understand the role of scattering, a case study is performed in which $SSA_{liq,11}$ and $SSA_{ice,11}$

are jointly varied from 0.075 to 0.95 and the $\frac{d(BT_{11})}{d(IWP)}$ is computed for the LWP-IWP parameter space

(Figure 5.6). It should be noted that, for both liquid and ice, SSA_{11} and $Q_{abs,11}$ change together such

that $Q_{ext,11}$ is constant. The case study is for a low cloud case in which the T_s-T_{ice} = 5 K and the

D_{eff_ice} is 60 µm. Both SSA_{liq} and SSA_{ice} are approximately 0.45 for the COPs used in this study,

and thus panel (e) in Figure 5.6 approximately represents the actual $\frac{d(BT_{11})}{d(IWP)}$ for this case. When

SSA$_{liq}$ and SSA$_{ice}$ are both set to 0.075 (Figure 5.6i), the main process impacting $\frac{d(BT_{11})}{d(IWP)}$ is
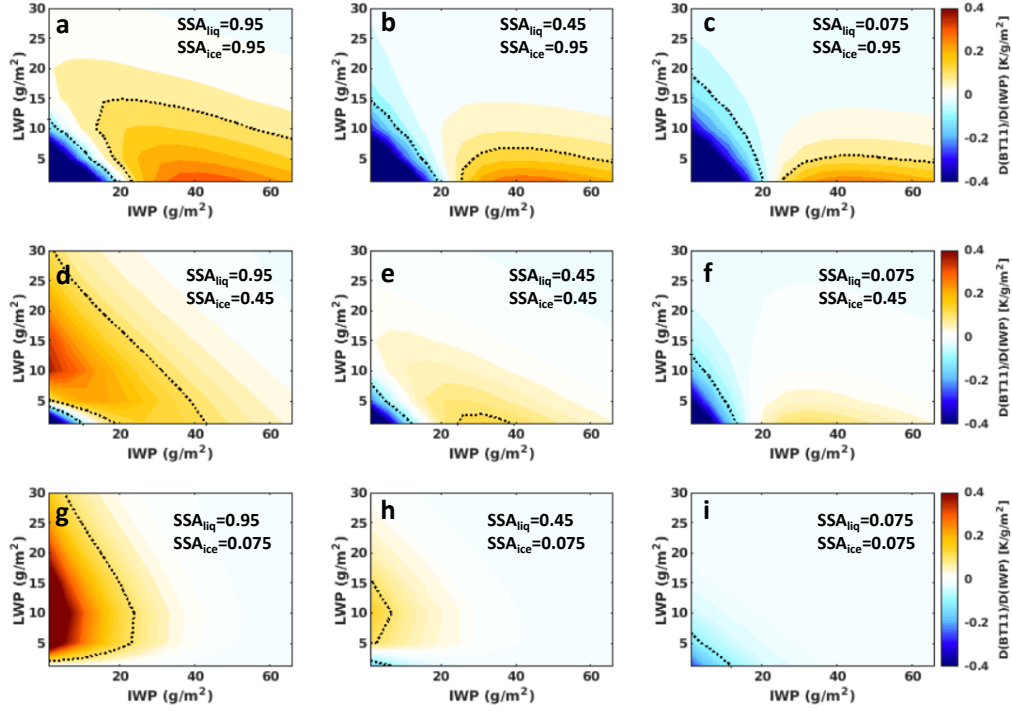
Figure 5.6. The gradient of BT$_{11}$ with respect to IWP when SSA$_{liq}$ and SSA$_{ice}$ are jointly varied for a low cloud case in which T$_s$-T$_{ice}$ ~ 5 K, TCWV < 1, and D$_{eff\_ice}$ = 60 um. Qext is constant for all cases.

absorption and emission by the cloud, which results in the expected negative $\frac{d(BT_{11})}{d(IWP)}$ pattern. When

the SSA$_{ice}$ is increased to 0.95 without changing SSA$_{liq}$ (Figure 5.6c), the negative $\frac{d(BT_{11})}{d(IWP)}$ area

expands and increases in magnitude, and the positive $\frac{d(BT_{11})}{d(IWP)}$ at larger IWPs becomes prominent.

This suggests ice scattering is playing a role in producing the opposite sign $\frac{d(BT_{11})}{d(IWP)}$. Inspection of

Figures 5.4 and 5.5 reveal that the magnitude and area of the positive and negative $\frac{d(BT_{11})}{d(IWP)}$ regions

vary with CTP and ΔT. This implies that there is a complex relationship between scattering and

T$_s$-T$_{ice}$ which is dependent on the IWP. The positive and negative $\frac{d(BT11)}{d(IWP)}$ regions are more

noticeable for the 60 µm D_{eff_ice} cases compared to 20 µm D_{eff_ice} cases because $SSA_{ice,11}$ increase with particle size for this D_{eff_ice} range.

Overall, the results here suggest that D_{eff_ice}, the ΔT (and thus cloud-surface temperature contrast), IWP, and LWP play the most dominant roles in determining the $\frac{d(BT_{11})}{d(IWP)}$. Comparisons between the MODTRAN5 simulations and the analytical model results, as well as the scattering sensitivity study in Figure 5.6, indicate that scattering, absorption, and emission can all play major roles in determining $\frac{d(BT_{11})}{d(IWP)}$. Additionally, the BT_{11} seems to have the least sensitivity to IWP changes for the mid-level clouds, which is possibly due to the absorption and scattering processes counteracting. Finally, the $\frac{d(BT_{11})}{d(IWP)}$ can pass the 0.1 K/g/m^2 threshold for IWPs and LWPs up to ~50 g/m^2, depending on D_{eff_ice} and ΔT.

5.4 Case Study for Detecting LTM$_{ice}$ with the Far-IR BTD Ice Test

A reliable algorithm for the detection of the LTM$_{ice}$ should incorporate more channels than just 11 µm. One possibility is to use the far-IR brightness temperature difference ice cloud detection test developed in Chapter 4 (BTD$_{449-521}$). Figure 5.7 shows BTD$_{449-521}$ for a high- (left column), mid- (middle column) and low-level (right column) cloud prescribed in an ERA5 scene with T$_s$-T$_{ice}$ ~ 5 K and TCWV < 1 for D_{eff_ice}= 20 µm (top row) and for D_{eff_ice}=60 µm (bottom row). The -1.5 K and 0.5 K BTD thresholds are exceeded within the dotted contours. For the 20 µm D_{eff_ice} case, the most obvious feature is the large negative BTD$_{449-521}$ that becomes more negative with IWP. From Chapter 4, it was shown that multiple scattering can lead to large negative BTD$_{449-521}$ and this effect is strengthened with increasing optical depth, or IWP in this case. The larger the IWP, the wider the range of IWP and LWPs for which the negative BTD$_{449-521}$ threshold is exceeded. For the 60 µm D_{eff_ice} case, like what was shown in Chapter 4, BTD$_{449-521}$ can also

become more negative with optical depth (in this case IWP) due to scattering. For the high cloud case with 60 µm D_{eff_ice}, $BTD_{449-521}$ exceeds the 0.5 K threshold for up to IWP ~ 55 g/m^2 when the liquid layer above is relatively thin (LWP<10 g/m^2), and this IWP range decreases with increasing CTP. This positive $BTD_{449-521}$ here represents the absorption regime discussed in Chapter 4, which is most prominent when the cloud-surface temperature contrast is large, such as for high cloud
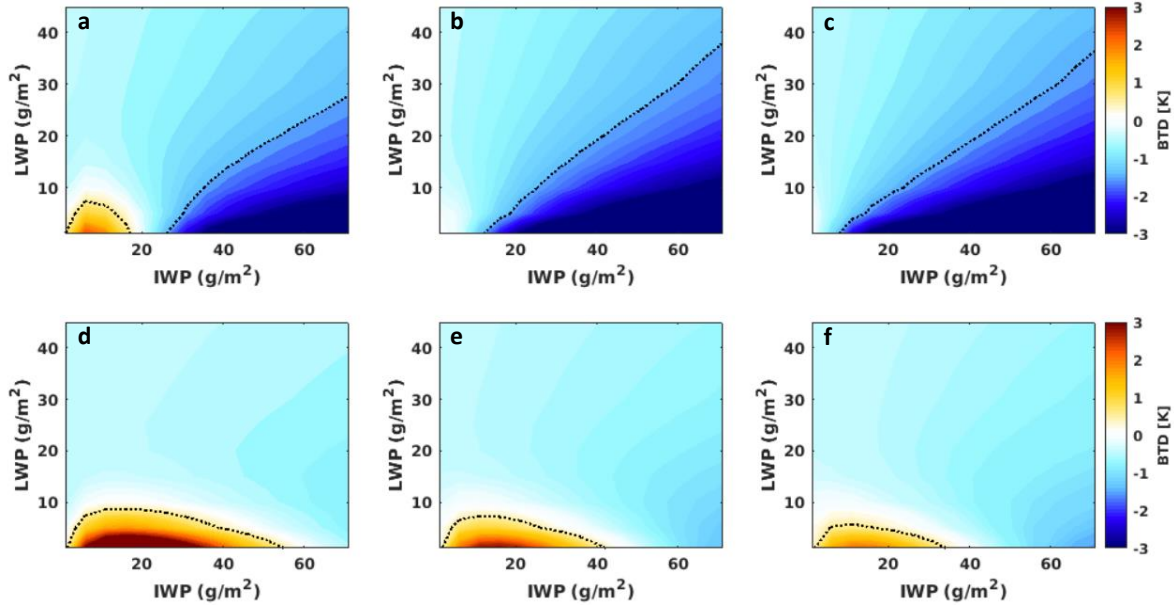
Figure 5.7. (a) The difference between the brightness temperatures at 449 and 521 cm^{-1} as a function of IWP and LWP for a high-level SMC (CTP$_{liq}$=850 hPa), where D_{eff_ice}=20 µm. For this case, T_s-T_{ice} ~ 5 K and TCWV < 1 (b) same as (a) but for CTP$_{liq}$= (c) same as a but for CTP$_{liq}$= (d-f) same as (a-c) expect for D_{eff_ice}=60 µm.

cases. For the high cloud case with 20 µm D_{eff_ice} (Figure 5.7a), such positive $BTD_{449-521}$ occurs for IWP < ~20 g/m^2 and LWP < ~ 7 g/m^2, but is not present for the mid- and low-level cases.

The case study in Figure 5.7 illustrates that the far-IR BTD test can potentially be used for detecting the presence of cloud ice in certain LTM cases. However, it is also important to determine if the LWP and IWP combinations for which the $BTD_{449-521}$ and $\frac{d(BT_{11})}{d(IWP)}$ exceed their respective thresholds correspond to the actual LWPs and IWPs of LTMs in the Arctic. Figure 5.8 shows a joint LWP-IWP histogram for LTM profiles measured from the United States DOE Atmospheric

Radiation Measurement (ARM) site on the north slope of Alaska. The criteria for LTM qualification here is that (1) LWP and IWP are both greater than 1 g/m^2 and (2) the cloud profile
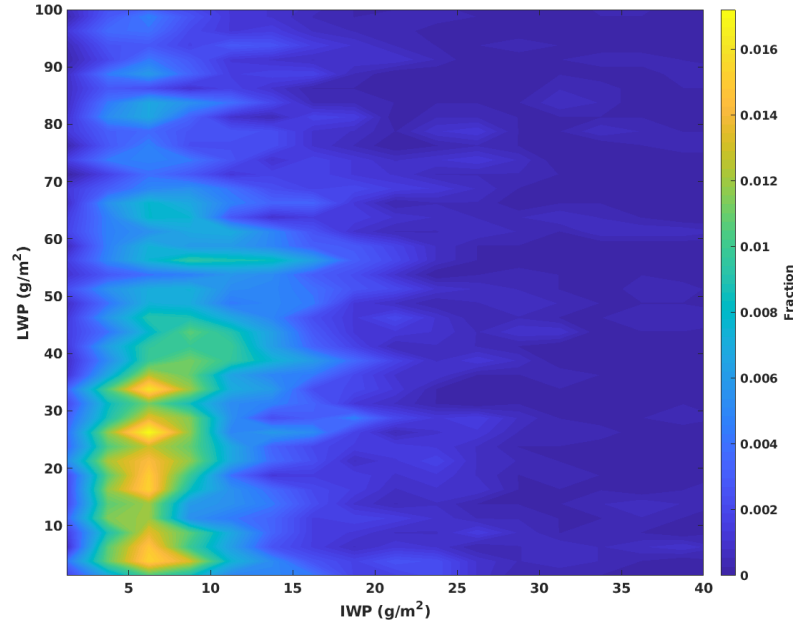
Figure 5.8. Liquid water path (LWP) and ice water path (IWP) statistics for liquid-topped mixed phase clouds at the DOE ARM site on the north slope of Alaska. The data covers January-August 2003. The algorithm for the LWP and IWP retrievals is from Zhang et al. (2017).

consists of one layer of liquid cloud above a single ice cloud layer. From Figure 5.8, the majority of LTMs have IWP < 20 g/m2 and LWP < 50 g/m2, which are ranges in which both the BTD$_{449-521}$ and $\frac{d(BT_{11})}{d(IWP)}$ thresholds are exceeded for in this study.

5.5 Summary and Discussion

This preliminary study aims to explore the potential of using spaceborne IR radiances to detect cloud ice within one of the most common types of mixed phase clouds in the Arctic, liquid-topped mixed phase clouds, or LTMs. To do so, ERA5 reanalysis data for the Arctic region was used as input to MODTRAN5 and BT$_{11}$ was simulated for various prescribed cases of LTMs and the results were compared to a simple analytical model of an idealized LTM case. Using eight months of ERA5 data from the year 2003, 57 Arctic scene types were established using discrete

145

intervals of T_s, TCWV, and ΔT. For each one of these scene types, $\frac{d(BT_{11})}{d(IWP)}$ was computed for prescribed SMCs with differing LWPs, IWPs, D_{eff_ice} and CTP.

A simple analytical model of an LTM showed that, when only cloud absorption and emission is considered, $\frac{d(R_{TOA,11})}{d(IWP)}$ (equivalently, $\frac{d(BT_{11})}{d(IWP)}$) is always negative or zero when the cloud is colder than the surface and positive or zero when the cloud is warmer than the surface.

A threshold of 0.1 K/g/m^2 was chosen to determine if $\frac{d(BT_{11})}{d(IWP)}$ was sufficiently large such that LTM$_{ice}$ can be considered "detectable" using BT$_{11}$. The results show that this threshold can be exceeded for cases in which IWP and LWP are less than ~50 g/m^2, depending on ΔT and D_{eff_ice}. On the joint IWP and LWP plot, the area in which the $\frac{d(BT_{11})}{d(IWP)}$ threshold is exceeded represents the LWP-IWP manifolds that this study aims to develop.

It was found that ΔT was the main variable in the ERA5 scene types that corresponded to significant changes in $\frac{d(BT_{11})}{d(IWP)}$, so $\frac{d(BT_{11})}{d(IWP)}$ for all ERA5 scenes within each ΔT were averaged. Note that the ΔT corresponds to T_s-T_{ice} when LTM$_{ice}$ has a CTP greater than 750 hPa. The results showed that, for the high clouds, regardless of ΔT or D_{eff_ice}, $\frac{d(BT_{11})}{d(IWP)}$ is always negative or zero, which is consistent with the analytical model results. For the low and middle clouds, both positive and negative $\frac{d(BT_{11})}{d(IWP)}$ regions in the LWP-IWP parameter space become noticeable, with the magnitude and LWP-IWP range in which the threshold is exceeded changing with ΔT and D_{eff_ice}. Through sensitivity analyses in which SSA$_{ice,11}$ and SSA$_{liq,11}$ are varied, it was determined that scattering plays an important role in determining the opposite sign values of $\frac{d(BT_{11})}{d(IWP)}$ and that role changes

with the ΔT and D_{eff_ice}. It is also apparent that $SSA_{liq,11}$ variations can significantly impact $\frac{d(BT_{11})}{d(IWP)}$.

Thus, the role of D_{eff_liq} should be investigated in future studies.

In this study, it was assumed that the ice COP database used to generate the synthetic radiances resembles the actual ice cloud properties in the polar regions. This database represents the state-of-the-art knowledge of ice cloud single scattering properties for many different habits. The COP database was generated using over 14,000 aircraft measurements, with only a small fraction of those measurements coming from polar regions. It is possible that a different combination of habits would be more appropriate for representing polar ice clouds, but no ice COP database has been produced for the polar regions due to limited aircraft campaigns in such regions. Furthermore, the fidelity of the ERA5 reanalysis humidity, temperature, and cloud water profiles, which are used in this study due to their temporal and spatial coverage, can also influence the applicability of the results of this study in reality. Reanalysis heavily relies on assimilated satellite observations, especially for the cloud water profiles, and thus the results of this study will be impacted by the quality of the assimilation. Further validation of the ERA5 reanalysis profiles against in-situ measurements in the polar regions can improve confidence in the use of such profiles for similar studies.

The case study in section 5.4 illustrates that it may be possible to use the far-IR BTD test ($BTD_{449-521}$) developed in Chapter 4 to detect the LTM_{ice}. However, the impacts of variables such as ΔT and TCWV on $BTD_{449-521}$ were not fully addressed. Given that water vapor can impact $BTD_{449-521}$, it necessary to investigate how the $BTD_{449-521}$ results in Figure 5.7 change for LTM cases with differing TCWV and how that impacts the LWP-IWP parameter space in which the $BTD_{449-521}$ test can be passed. It is also of interest to perform the mid-IR BTD (i.e., "AIRS-like") from Chapter 4 on LTM cases, as this test is most useful for ice detection compared to liquid.

147

Furthermore, the spectral variation of SSA_{liq} and $Q_{abs,liq}$ is large from the far-IR to the mid-IR, while it can be very small for ice water for the same channel combination. This indicates that a BTD test consisting of a far-IR and mid-IR channel may be capable of detecting the presence of the LTM_{liq}, while the mid-IR and far-IR BTD ice cloud tests could be used for the detection of LTM_{ice}. Overall, this allows for the detection of the LTM.

Acknowledgements

References

Bergeron, T. (1935). On the physics of clouds and precipitation. Proces Verbaux de l'Association de Météorologie, International Union of Geodesy and Geophysics, 156–178.

Cesana, G., Kay, J. E., Chepfer, H., English, J. M., & de Boer, G. (2012). Ubiquitous low-level liquid-containing Arctic clouds: New observations and climate model constraints from CALIPSOGOCCP. *Geophysical Research Letters*, 39, L20804. https://doi.org/10.1029/2012GL053385

Cho, H., Jun, S.-Y., Ho, C.-H., & McFarquhar, G. (2020). Simulations of winter Arctic clouds and associated radiation fluxes using different cloud microphysics schemes in the Polar WRF: Comparisons with CloudSat, CALIPSO, and CERES. *Journal of Geophysical Research: Atmospheres*, 125, e2019JD031413. https://doi.org/10.1029/2019JD031413

Findeisen, W. (1938). Kolloid-meteorologische Vorgänge bei Neiderschlags-bildung. Meteorologische Zeitschrift, 55, 121– 133.
Wegener, A. (1911). Thermodynamik der Atmosphäre (331 pp.). Leipzig.

de Boer, G., Collins, W. D., Menon, S., & Long, C. N. (2011). Using surface remote sensors to derive radiative characteristics of Mixed-Phase Clouds: An example from M-PACE. Atmospheric Chemistry and Physics, 11(23), 11,937– 11,949. https://doi.org/10.5194/acp-11-11937-2011

Kahn, B. H., Irion, F. W., Dang, V. T., Manning, E. M., Nasiri, S. L., Naud, C. M., et al. (2014) The Atmospheric Infrared Sounder version 6 cloud products. *Atmospheric Chemistry and Physic*s, 14, 399-426. https://doi.org/10.5194/acp-14-399-2014

Klein, S. A., McCoy, R. B., Morrison, H., Ackerman, A. S., Avramov, A., Boer, G., et al. (2009). Intercomparison of model simulations of mixed-phase clouds observed during the ARM Mixed-Phase Arctic Cloud Experiment. I: single-layer cloud. *Quarterly Journal of the Royal Meteorological Society*, 135(641), 979– 1002. https://doi.org/10.1002/qj.416

McCoy, D. T., Tan, I., Hartmann, D. L., Zelinka, M. D., & Storelvmo, T. (2016). On the relationships among cloud cover, mixed-phase partitioning, and planetary albedo in GCMs. *Journal of Advances in Modeling Earth Systems*, 8, 650– 668. https://doi.org/10.1002/2015MS000589

Morrison, H., de Boer, G., Feingold, G., Harrington, J., Shupe, M. D., & Sulia, K. (2012). Resilience of persistent Arctic mixed-phase clouds. Nature Geoscience, 5(1), 11– 17. https://doi.org/10.1038/ngeo1332

Sassen, K., Wang, Z., & Liu, D. (2008). Global distribution of cirrus clouds from CloudSat/Cloud-Aerosol Lidar and Infrared Pathfinder Satellite Observations (CALIPSO) measurements. Journal of Geophysical Research, 113, D00A12. doi:10.1029/2008JD009972

Shupe, M. D. (2011). Clouds at Arctic atmospheric observatories. Part ii: Thermodynamic phase characteristics. *Journal of Applied Meteorology and Climatology*, 50(3), 645-661. https://doi:10.1175/2010jamc2468.1

Shupe, M. D., Walden, V. P., Eloranta, E., Uttal, T., Campbell, J. R., Starkweather, S. M., et al. (2011). Clouds at Arctic atmospheric observatories. Part I: Occurrence and macrophysical properties. *Journal of Applied Meteorology and Climatology*, 50, 626– 644. https://doi.org/10.1175/2010JAMC2467.1

Verlinde, J., Harrington, J. Y., McFarquhar, G. M., Yannuzzi, V. T., Avramov, A., Greenberg, S. (2007). The mixed-phase arctic cloud experiment. *Bulletin of the American Meteorological Society*, 88(2), 205– 222. https://doi.org/10.1175/BAMS-88-2-205

Zhang, D., Wang, Z., Luo, T., Yin, Y., & Flynn, C. (2017). The occurrence of ice production in slightly supercooled Arctic stratiform clouds as observed by ground-based remote sensors at the ARM NSA site. *Journal of Geophysical Research: Atmospheres*, 122, 2867–2877. https://doi.org/10.1029/2019JD030673

Chapter 6 Summary and Future Outlook

6.1 Background Overview

As the Arctic continues to become warmer and wetter, it is crucial to monitor the vast and remote region using satellite observations. Arctic climate is significantly influenced year-round by longwave (LW) radiation emitted and absorbed by the atmosphere, clouds, and surface. Atmospheric gases, such as water vapor, absorb and emit LW radiation at specific frequencies, and this leads to the outgoing longwave radiation (OLR) being smaller than the surface emission: the so-called greenhouse effect. The difference between surface emission the OLR normalized by the surface emission is called greenhouse efficiency (GHE), and provides a metric of determining how efficient the surface-atmosphere system is at trapping LW radiative energy emitted by the surface. Both OLR and GHE are fundamentally spectral quantities and are important metrics for Arctic climate studies, but typically both quantities are evaluated in a broadband form (i.e., integrated across the LW spectrum). The first study of this dissertation (Chapter 2) seeks to break down Arctic OLR and GHE trends spectrally to understand how the spectral components of these trends contribute to the broadband trends and understand how changes in the Arctic atmosphere and surface are related to the spectral OLR and GHE trends.

Cloud cover is extensive in the Arctic and clouds tend to warm the Arctic surface through LW emission during most of the year. Liquid phase clouds tend to be opaquer than ice phase clouds for the same cloud water amount, and thus liquid clouds tend to contribute to more surface warming. Mixed phase clouds containing supercooled liquid water are ubiquitous in the Arctic and

the processes that produce and maintain them are complex and not well understood. Improving the understanding of the large-scale Arctic cloud phase distributions and their radiative impacts requires satellite observations. Infrared (IR) imagers are useful for Arctic cloud phase studies because they can be used year-round in the Arctic (unlike shortwave imagers) and can have larger horizontal spatial footprints compared to spaceborne radar and lidar. The IR can be used for cloud phase retrievals based on the different spectral variations of liquid and ice cloud absorption across the mid-infrared (mid-IR; ~800-1250 cm^{-1}). However, the mid-IR has limitations in the polar regions, especially when mixed phase clouds are present. The second study of this dissertation (Chapter 3) evaluates the cloud phase retrievals of the Atmospheric Infrared Sounder (AIRS), a hyperspectral instrument, over the Arctic Ocean against combined radar and lidar observations to further understand the mid-IR limitations for cloud phase determination in the Arctic region, especially for mixed phase clouds.

The far-infrared (far-IR; <~600 cm^{-1}), makes up over 60% of Arctic OLR and studies have shown the potential for using this spectral region for cloud phase determination. There have been no spectrally resolved far-IR observations from space during the modern satellite era, however there are two upcoming missions that will make such observations: the Far-infrared-Outgoing-Radiation Understanding and Monitoring (FORUM) and the Polar Radiant Energy in the Far Infrared Experiment (PREFIRE) missions. Therefore, it is pertinent to investigate far-IR cloud phase retrievals from space. The third study of this dissertation (Chapter 4) presents a physically based and simple far-IR ice cloud detection algorithm for polar regions and seeks to understand the synergy between the far-IR and mid-IR for polar ice cloud detection.

The detection of Arctic mixed phase clouds with the IR remains a challenge. One of the most common types of mixed phase clouds in the Arctic are liquid-topped stratiform mixed phase

clouds (LTMs). Essentially these clouds consist of a single liquid layer above a precipitating ice layer. Since the IR is more sensitive to the cloud top, the classification of the cloud can be weighted to liquid only. However, this dissertations and multiple studies confirm that the IR is more useful for the detection cloud ice as opposed to liquid. In the last study of this dissertation (Chapter 5), we investigate the sensitivity of 11 µm brightness temperature (BT_{11}) at the TOA to changes in the ice water path (IWP) of LTMs for a range of different atmospheric and cloud conditions. The far-IR BTD test is also employed in a case study to demonstrate that the far-IR can be useful for the detection of the LTM ice layer (LTM_{ice}).

6.2 Chapter Summaries

6.2.1 Chapter 2 Summary

Chapter 2 derives, for the first time, zonal mean spectral OLR and GHE trends in the Arctic using 14 years of spectrally resolved radiative fluxes from combined AIRS and Clouds and the Earth's Radiative Energy System (CERES) observations. AIRS level 3 (L3) retrievals of atmospheric humidity (q_{H2O}), atmospheric temperature (T_{atm}) and surface temperature (T_s) are used as inputs to the Principal Component Radiative Transfer Model (PCRTM) to derive clear sky spectral OLR and GHE trends for comparison with their observed counterparts. Chapter 2 focuses on the months of March, July, and September, as they represent the onset of the sea ice melt season, peak of solar insolation, and the end of the sea ice melt season, respectively. For each month, the simulated spectral OLR and GHE trends are similar to the observed ones, which allows for a clear connection to be established between changes (or lack thereof) in T_s, T_{atm}, q_{H2O}, and trends in spectral OLR and GHE.

For March, the spectral OLR trends are the largest compared to the other months, are positive in the mid-IR and far-IR window, and statistically significant north of ~70°N for both all-sky and clear-sky. The September observed clear-sky and all-sky OLR trends are also positive in the same spectral regions for much of the Arctic, but none are statistically significant at the 5% confidence level. For July, the spectral OLR trends are negative in the far-IR dirty window and a mix of negative and positive trends in the mid-IR for different latitudes in the Arctic. The clear-sky spectral GHE trends are positive in July across the water vapor ν_2 band and far-IR for 70–80°N. Much larger positive clear-sky spectral GHE trends occur in March for regions north of 80°N in the same spectral region. Sensitivity studies show that increasing T_s contributes much more to the spectral OLR and GHE trends than trends in T_{atm} and q_{H2O}. However, there are cases in which the latter two are discernable over many spectral regions, such as the increase of q_{H2O} leading to positive spectral OLR trends due to the existence of a temperature inversion.

6.2.2 Chapter 3 Summary

In Chapter 3, the AIRS cloud phase retrievals, which were never evaluated over the Arctic, are compared to collocated radar and lidar observations from CloudSat and Cloud–Aerosol Lidar and Infrared Pathfinder Satellite Observations (CALIPSO; together CCL), respectively, over the Arctic using four years of data. In a previous global evaluation of AIRS cloud phase (Jin & Nasiri, 2014), AIRS footprints were collocated with CALIPSO only, and the mixed phase category was based on the number of liquid and ice phase CALIPSO footprints within the AIRS field of view (FOV; ~13.5 km at nadir). However, in this study, the use of CCL allows for mixed phase classifications of individual CCL FOVs (~1.5 km) within the AIRS FOV, which is important because the scale of cloud phase mixing in for mixed phase clouds can be on the order of tens of meters. Also, in contrast to Jin & Nasiri (2014), we mainly use CCL FOVs with a single cloud

layer that covers the entire CCL FOV, which we refer to as a single-layer-overcast CCL group. These groups are identified as mixed, liquid, or ice phase if enough CCL FOVs (≥90%) with a given group are of that phase. There are ~15-19 CCL FOVs within a nadir AIRS FOV, and the AIRS cloud phase retrieval for the FOV is compared to the CCL group's phase. This comparison is performed using ~4 million AIRS FOVs and ~61 million CCL FOVs and which are separated based on whether the underlying surface type is open ocean or sea ice.

AIRS ice phase classification skill was >85% depending on the surface type, while for liquid it was between 21% and 32%. Mixed phase clouds corresponded to mainly to AIRS liquid and unknown phase classifications, and most AIRS unknown phase classifications corresponded to mixed phase clouds. The results of the AIRS cloud phase evaluation against two-layer-overcast CCL groups suggest that AIRS can detect the underlying layer's phase, which could be possible if the overlying layer is optically thin enough. Overall, the two-layer-overcast systems corresponded to AIRS unknown cloud phase.

Using all CCL and AIRS FOVs, it was determined that seasonal cycle, and in some cases, the dependence of cloud phase relative occurrence on total column water vapor and the temperature difference between 1000 hPa and 300 hPa, was similar between CCL and AIRS. Thus, it is possible that the connections between Arctic atmosphere properties and processes can be captured by the AIRS cloud phase data. Moreover, the accurate seasonal cycle of AIRS liquid and ice cloud phase indicates that AIRS could provide accurate occurrence anomalies on inter-seasonal to interannual scales.

For the month of July 2009, AIRS, CCL, and the Moderate Resolution Imaging Resolution (MODIS) are all collocated together so that the MODIS cloud cover and cloud phase classifications (~200 1 km MODIS pixels for each near nadir AIRS FOV) can be compared to the

AIRS and CCL cloud phase retrievals. The purposes of this analysis are to understand how cloud phase throughout the AIRS FOV compared to the cloud phase of the CCL groups, and how heterogeneity of MODIS cloud macrophysical properties impacts AIRS phase decisions. It was determined that heterogeneity of cloud cover and cloud phase throughout the AIRS FOV corresponded to AIRS unknown phase classifications, which supports previous findings. MODIS cloud phase also corresponded to CCL cloud phase, which provides more confidence in use of the single-layer-overcast CCL groupings for AIRS cloud phase evaluations. Overall, 42% of AIRS Arctic cloud phase classifications were unknown phase, which suggests that further improvements to the AIRS cloud phase algorithm may be necessary to reduce the amount of such unknown classifications.

6.2.3 Chapter 4 Summary

Chapter 4 develops a physically based and simply far-IR brightness temperature difference (BTD) polar ice cloud detection algorithm and compares it to a mid-IR test that is typically used for cloud phase classifications. ECMWF ERA5 polar cloud profiles over ocean for the year of 2005 are used for algorithm development and evaluation. The ERA5 profiles are fed into the MODerate Resolution Atmospheric TRANsmission Version 5 (MODTRAN5) to simulate spectra from 400-1300 cm^{-1} with a resolution of 1 cm^{-1}, approximately three times coarser than the expected FORUM spectral resolution. The far-IR algorithm is based on the spectral variation of ice cloud scattering and absorption across the far-IR dirty window region (400-600 cm^{-1}), a spectral region with numerous semi-transparent water vapor micro windows. This spectral region is especially transparent in the dry polar atmospheres.

The far-IR BTD test is based on the BTD between the channels of 449 cm^{-1} and 521 cm^{-1} ($BTD_{449-521}$). These channels were chosen by accounting for the impacts of water vapor and the

variation in ice cloud optical properties (COPs) across the far-IR dirty window. The $BTD_{449-521}$ test is subject to both ice cloud multiple scattering (leads to negative $BTD_{449-521}$) and absorption (leads to positive $BTD_{449-521}$), and thus a positive and negative $BTD_{449-521}$ threshold was used for ice cloud detection. The double threshold attempts to conservatively avoid misclassifications in the ERA5 dataset.

To determine the far-IR polar ice cloud determination skill and for comparison with an "AIRS-like" mid-IR BTD test ($BTD_{1231-960}$), ice cloud test spectra were generated using four different effective diameters (D_{eff_ice}), creating four D_{eff_ice} groups with the same number of spectra. It was found that the $BTD_{449-521}$ test is more successful for the smallest D_{eff_ice} used in this study (20 µm) compared to the mid-IR test, which was comparable or more successful for larger D_{eff_ice}. When the D_{eff_ice} is the intermediate value of 40 µm, the mid-IR and far-IR synergy is most obvious. By increasing cloud optical depth (COD), far-IR multiple scattering can increase and lead to increasingly negative $BTD_{449-521}$. Both BTD tests have some dependence on cloud top pressure (CTP) and COD, but overall are most dependent on D_{eff_ice}.

6.2.4 Chapter 5 Summary

This chapter presents a preliminary study that aims to explore the potential of spaceborne IR spectral radiances for detecting the underlying ice layer of liquid-topped stratiform mixed phase clouds (LTMs), which is referred to as LTM_{ice}. The overlying liquid layer is referred to as LTM_{liq}. The sensitivity of the brightness temperature at 11 µm (BT_{11}) to changes in the ice water path (IWP) of the LTM_{ice}, which is referred to as $\frac{d(BT_{11})}{d(IWP)}$, is used because BT_{11} is a standard metric for satellite-based cloud detection with the IR. The main goal of the study was to develop joint liquid water path (LWP) and IWP manifolds in which the absolute value $\frac{d(BT_{11})}{d(IWP)}$ exceeds a threshold of

0.1 K/g/m^2, which represents a limit in which BT$_{11}$ is sufficiently sensitive to the changes in the IWP of the LTM$_{ice}$. The results are compared to a simple analytical model.

The BT$_{11}$ is simulated with a radiative transfer model using ERA5 reanalysis data over the Arctic and prescribed LTM properties. The BT$_{11}$ computed for a range of ERA5 scene types based on discrete intervals of T$_s$, TCWV, and the temperature difference between 1000 hPa and 700 hPa (ΔT). For each ERA5 scene, BT$_{11}$ was simulated for a range of LTM$_{liq}$ liquid water paths, LTM$_{ice}$, and IWP. The CTP was also varied between high-, mid- and low-level based on the International Satellite Cloud Climatology Project (ISCCP), and each simulation was performed for a D$_{eff\_ice}$ of 60 and 20 µm.

Of the three scene type parameters, ΔT has the most impact on $\frac{d(BT_{11})}{d(IWP)}$, so $\frac{d(BT11)}{d(IWP)}$ for all ERA5 scenes within each ΔT were averaged. Regardless of ΔT and D$_{eff\_ice}$, $\frac{d(BT_{11})}{d(IWP)}$ is always negative or zero for the high-level clouds, which is consistent with the analytical model results. When the clouds are mid-level or low-level, $\frac{d(BT_{11})}{d(IWP)}$ can be both positive and negative depending on LWP, IWP, ΔT and D$_{eff\_ice}$. It was determined that multiple scattering in the LTM$_{ice}$ played a key role in determining the sign of $\frac{d(BT_{11})}{d(IWP)}$ for the mid- and low-level clouds. Since the 60 µm D$_{eff\_ice}$ ice particles have a larger ice cloud single scattering albedo at 11µm (SSA$_{ice,11}$) compared to the 20 µm case, the larger particle size case showed the most distinct positive and negative $\frac{d(BT_{11})}{d(IWP)}$ regions in the LWP-IWP parameter space. It is also apparent that SSA$_{liq,11}$ variations can significantly impact the $\frac{d(BT_{11})}{d(IWP)}$ parameter space, and this is a subject of future work.

The results show that the 0.1 K/g/m^2 $\frac{d(BT_{11})}{d(IWP)}$ threshold can be exceeded for cases in which

IWP and LWP are less than ~50 g/m^2, depending on ΔT and D_{eff_ice}. Using ground based LTM

profiles from Barrow, Alaska, it was found that a large fraction of LTM cases have IWP and LWP

less than ~50 g/m^2, which suggests that the result of this study are applicable to realistic LTMs. A

case study is also performed that illustrates how BTD$_{449-521}$ varied based on CTP and D_{eff_ice}. The

results suggest that it may be possible to use the BTD$_{449-521}$ ice cloud detection test to detect the

presence of cloud ice in an LTM, but further work is needed.

6.3 Future Outlook

One of the most important findings from this thesis are the application of far-IR spectral

fluxes for Arctic climate and radiation studies. Chapter 2 showed that, due to the dry Arctic

atmosphere, far-IR spectral fluxes observed at the Arctic TOA have signatures of changing water

vapor amounts and temperatures at tropospheric levels closer to the surface compared to lower

latitudes. The far-IR spectral fluxes used in Chapter 2 are estimated using spectral fluxes observed

at AIRS channels (which do not include far-IR), and thus the far-IR fluxes are not "true"

observations. Future far-IR missions, such as FORUM, represent an unprecedented opportunity to

study the Arctic spectral OLR changes as the Arctic troposphere becomes warmer and wetter,

which is critical due to the far-IR making up the majority of polar OLR. For example, it is known

that reductions in sea ice can increase evaporation from the Arctic Ocean and lead to an increase

in the Arctic downwelling IR radiation and the strength of the greenhouse effect (e.g., Screen &

Simmonds, 2010; Gong et al., 2017; Kapsch et al., 2017). Observations of far-IR spectral OLR

may allow for the OLR changes to be attributed to changes in Arctic tropospheric humidity that

correspond to sea ice changes. Furthermore, it has been shown that TOA radiances can be used to

simultaneously retrieve T_{atm}, q_{H2O}, and T_s (Palchetti et al., 2008). The measured far-IR spectral

radiances and the retrieved profiles can then be used to convert the spectral radiances into spectral fluxes (e.g., Palchetti et al., 2008). This allows for the same far-IR radiances to be used for retrieving the Arctic atmospheric state and for deriving the spectral fluxes, which provides consistency in the relating of changes in far-IR retrieved geophysical variables like q_{H20} to changes in far-IR spectral fluxes.

Another major finding from this thesis is that the scattering of far-IR photons can be used for detection of ice clouds from space. Previous studies of IR cloud phase retrievals only explicitly consider the spectral variations of ice and liquid cloud absorption. Thus, this thesis demonstrates that an under considered IR cloud radiative process, scattering, can be used for Arctic ice cloud detection using passive IR satellite measurements. One major implication of this is the detection of polar ice clouds that have a low thermal contrast with the surface, which has been a challenge historically for polar cloud detection. Using standard IR cloud detection techniques, such as BT_{11}, this cloud would be indistinguishable from nearby clear sky scenes. Absorption based bi-spectral IR methods would also fail to detect the ice clouds. However, scattering is virtually not temperature dependent, which means that far-IR BTD test from Chapter 4 could be able to detect the ice clouds. Another implication of using IR scattering for ice cloud detection is the potential detection of mixed phase clouds in polar regions. Figure 5.7 illustrates that the far-IR BTD test can detect the presence of ice in polar mixed phase clouds. The simultaneous detection of the liquid cloud water component with other IR tests would mean that the mixed phase cloud would be detectable with the IR, something that has not been previously accomplished to our best knowledge. Figure 4.1 shows that the spectral variation of liquid cloud scattering and absorption can be large from the mid-IR to the far-IR, while the variation for ice clouds can be small. A BTD test using one channel

from the mid-IR and one channel from the far-IR could potentially be used to detect the liquid water component of a polar mixed phase cloud.

The concept of far-IR ice cloud scattering also has applications in Arctic surface energy budget studies. Chen et al. (2020) showed that polar ice cloud LW scattering can significantly contribute to the downwelling LW fluxes at the polar surface using a climate model with a coupled atmosphere and surface. This study also showed that the scattered far-IR radiation was an important contributor to such downwelling fluxes. Chapter 4 of this dissertation showed that far-IR ice cloud scattering is spectrally dependent and is significantly influenced by ice particle size and cloud optical depth. However, observational studies on how the ice cloud scattering impacts far-IR spectral fluxes at the Arctic surface have not been performed to our best knowledge. In future studies, ground-based ice cloud profiles can be fed into a radiative transfer model that accounts for multiple scattering. Upwelling and downwelling Far-IR spectral radiances can be generated for the cloud profiles and converted to spectral fluxes, which can then be compared with contemporaneous downwelling broadband or spectral flux measurements at the ground station. This could allow for an assessment of the contribution of the ice cloud scattering on the surface far-IR radiative fluxes and how ice cloud microphysics contribute. A radiative closure analysis (i.e., finding conditions in which the simulated and observed fluxes match) could then provide insight into how to improve the state-of-the-art bulk ice cloud optical property models. Such a radiative closure analysis could also be performed using measured TOA far-IR spectral radiances collocated with ground-based ice cloud observations from which the far-IR TOA spectral radiances can be simulated and compared to the observations.

Improving bulk ice COP models is crucial for the applying satellite-based IR measurements to study polar ice clouds and their impact on polar climate. Currently, to our best knowledge, there

are no bulk ice COP models that are designed specifically for polar regions. The state-of-the-art

models from Yang et al. (2013) and Baum et al. (2014) included measurements from one aircraft

campaign in Alaska, with the vast majority of the other profiles being from the tropics and mid-

latitudes. Since polar cloud microphysical properties can be different from their counterparts in

the lower latitudes, it is possible that the habit and particle size distributions of polar ice clouds are

different than what is assumed in the state-of-the-art models used in this thesis. In the future, more

aircraft campaigns should be undertaken in the polar regions to develop a comprehensive

understanding of the habit and particle size distributions of polar ice clouds.

References

Baum, B. A., Yang, P., Heymsfield, A. J., Bansemer, A. R., Cole, B. H., Merrelli, A., et al. (2014). Ice cloud single-scattering property models with the full phase matrix at wavelengths from 0.2 to 100 um. *Journal Of Quantitative Spectroscopy & Radiative Transfer*, 146, 123-139. https://doi:10.1016/j.jqsrt.2014.02.029

Chen, Y.-H., Huang, X., Yang, P., Kuo, C.-P., & Chen, X. (2020). Seasonal dependent impact of ice cloud longwave scattering on the polar climate. *Geophysical Research Letters*, 47, e2020GL090534. https://doi.org/ 10.1029/2020GL090534

Gong, T. T., Feldstein, S., & Lee, S. (2017). The role of downward infrared radiation in the recent Arctic winter warming trend. *Journal of Climate*, 30(13), 4937-4949. https://doi.org/10.1175/jcli-d-16-0180.1

Kapsch, M. L., Graversen, R. G., & Tjernstrom, M. (2013). Springtime atmospheric energy transport and the control of Arctic summer sea-ice extent. *Nature Climate Change*, 3(8), 744-748. https://doi.org/10.1038/nclimate1884

L'Ecuyer, T. S., Drouin, B. J., Anheuser, J., Grames, M., Henderson, et al. (2021). The Polar Radiant Energy in the Far InfraRed Experiment: A New Perspective on Polar Longwave Energy Exchanges. *Bulletin of the American Meteorological Society*, 1-46. https://doi.org/10.1175/BAMS-D-20-0155.1

Palchetti, L., Bianchini, G., Carli, B., Cortesi, U., & Del Bianco, S. (2008). Measurement of the water vapour vertical profile and of the Earth's outgoing far infrared flux. *Atmospheric Chemistry and Physic,s* 8, 2885–2894, https://doi.org/10.5194/acp-8-2885-2008, 2008.

Screen, J. A., & Simmonds, I. (2010a). The central role of diminishing sea ice in recent Arctic temperature amplification. *Nature*, 464(7293), 1334-1337. https://doi.org/10.1038/nature09051

Sgheri, L., Belotti, C., Ben-Yami, M., Bianchini, G., Carnicero Dominguez, B., et al. (2021). The FORUM End-to-End Simulator project: architecture and results. *Atmospheric Measurement Techniques Discussion*, [preprint], https://doi.org/10.5194/amt-2021-196, in review.

Yang, P., Bi, L., Baum, B. A., Liou, K., Kattawar, G. W., Mishchenko, M. I., & Cole, B. (2013). Spectrally consistent scattering, absorption, and polarization properties of atmospheric ice crystals at wavelengths from 0.2 to 100 μm. *Journal of the Atmospheric Sciences*, 70(1), 330-347. https://doi.org/10.1175/JAS-D-12-039.1